DISSERTATION

submitted to the

Combined Faculties for the Natural Sciences and for Mathematics

of the Ruperto-Carola University of Heidelberg, Germany

for the degree of

Doctor of Natural Sciences

presented by

Daniela Urzica, Chem. Eng.

born in Targu Mureş, Romania

Expected oral-examination: July 02, 2010

Numerical Investigation of Droplet Vaporization and CH_4/Air, CH_4/O_2 and CH_4/LOX Counterflowing Spray Flames for Elevated Pressure

Examiners: Prof. Dr. Eva Gutheil

Prof. Dr. Uwe Riedel

Contents

Kurzfassung

Die Untersuchung der physikalischen und chemischen Prozesse ist eine wertvolle Hilfe für die Sicherung der Zuverlässigkeit und Effizienz vieler technischer und wissenschaftlicher Anwendungen. Beispiele dafür sind die Verbrennungsvorgänge in Einspritzmotoren, Gasturbinen oder Flüssigkeitsraketentriebwerken. Der erste Schritt zur Beschreibung der Vorgänge in einem Spray ist das Verständnis der grundlegenden Komponenten, beispielsweise des einzelnen Tröpfchens. Dafür ist es wichtig, ein numerisches Modell zu entwickeln, das den Prozess der Verdampfung eines Tröpfchens präzise beschreiben kann. Zu diesem Zweck wurde die durch einen Infrarot-Laser induzierte Verdampfung eines Wassertropfens berechnet. Dazu wurde ein kugelförmiges Tröpfchen in Luft unter Normalbedingungen angenommen, das mit Hilfe von vertikalen und horizontalen Glasfiberfasern fixiert ist. Als alternative Brennstoffe für Wasserstoff werden, aufgrund ihres hohen Energieinhalts, die Brennstoffe Methan und Kerosin untersucht. Dabei hat Methan wegen seiner sauberen Verbrennung gewisse Vorteile gegenüber Kerosin. Die vorliegende Arbeit trägt zu einem besseren Verständnis der Verbrennung von Methan/Luft, Methan/Sauerstoff und Methan/LOX (flüssiger Sauerstoff) gegenüber dem Wasserstoff/Sauerstoff System bei. Es wurden numerische Untersuchungen von laminaren CH_4/Luft und CH_4/Sauerstoff Flammen bei verschiedenen Mischungsverhältnissen von Stickstoff und Sauerstoff im Sauerstoffseite durchgeführt. Weiterhin wurde in einer Gegenstromkonfiguration die Flamme eines flüssigen Sauerstoff-Sprays in einem Methan Trägergas gegen einen Sauerstoff-Strom untersucht. Diese Ergebnisse können in Flamelet Bibliotheken oder in Flamelet generated manifolds bei turbulenter Verbrennung verwendet werden. Im zugrundeliegenden mathematischen Modell werden die ursprünglich zweidimensionalen Gleichungen durch eine Ähnlichkeitstransformation auf eine Dimension reduziert. Das numerische Modell benutzt eine axialsymmetrische Konfiguration mit einem adaptiven Gitter für die Gasphase. Es werden detaillierte Modelle für alle relevanten Prozesse verwandt. Im speziellen wird ein detaillierter chemischer Reaktionsmechanismus mit 35 Spezies und 294 elementaren Reaktionen benutzt. Das chemische Reaktionsschema, das in dieser Arbeit beschrieben wird, wurde in [1] entwickelt. Die thermodynamischen Daten für CH_4 und O_2 ziwschen 100 K und 300 K wurden, für die Verwendung bei der Berechnung kyrogener CH_4/LOx Verbrennung, für normalen und hohen Druck implementiert. Zur Verifizierung des mathematischen Modells, des Reaktionsmechanismus und des numerischen Verfahrens, wurden die wurden die vorliegenden Ergebnisse der laminaren CH_4/Luft -Flamme mit den Literaturwerten verglichen. Die CH_4/O_2 Flamme wurde für einen erhöhten Druckbereich bis zu 2 MPa untersucht. Die Streckungsgeschwindigkeit bei der Auslöschung wurde ebenso berechnet, wie der Wert der skalaren Dissipationsgeschwindigkeit. Diese Werte können für zukünftige turbulente Flamelet-Berechnungen verwendet werden. Es wurde gezeigt, dass die Verringerung von Sauerstoff, Druck und Streckungsgeschwindigkeit einen deutlichen Einfluss auf die Struktur der Flamme haben. Dies wird durch den Vergleich der Flammenstrukturen von flüssigem und gasförmigen Sauerstoff verifiziert. Die Verbrennung von CH_4/LOx

mit vorhergehender Verdampfung des flüssigen Sauerstoffs unter kyrogenen Bedingungen zeigte einen signifikanten Effekt der flüssigen Phase auf die Gastemperatur. Außerdem wurde bei der Vergrößerung des initialen Tröpfchendurchmessers eine Verbreiterung der Flamme des Sprays beobachtet.

Abstract

Study and optimization of the physical and chemical processes that are involved in many applications in science and engineering are worthwhile, to ensure the stability and efficiency of their performance. Examples are combustion process in direct injection engines, gas turbine combustors, and liquid rocket propulsion systems.

First step in understanding a spray must naturally be the understanding of its basic constituents: i.e. single droplets. Hence, it is important to develop good numerical models that can predict and simulate the process of evaporation of a single droplet accurately. Thus, computational investigation of the evaporation of water droplets induced by an infrared laser beam is performed. In particular, a single spherical droplet is considered, which is suspended on horizontal and vertical glass fibers in air under atmospheric pressure. The droplet heating and evaporation are induced by a pulsed CO_2 laser.

The fuels in liquid rocket propulsion systems, methane and kerosene, are being discussed as alternative fuels to hydrogen because of their high energy content. Methane has some advantages compared to kerosene because of its cleaner burning characteristics. The present study contributes to an improved understanding of methane/air, methane/oxygen and methane/LOX (liquid oxygen) combustion compared to the hydrogen/oxygen system. A numerical investigation of laminar CH_4/air and CH_4/O_2 flames is performed, where different mixtures of nitrogen and oxygen in the oxidizer stream are studied. Moreover, liquid oxygen spray flames with carrier gas methane against an oxygen stream are investigated in the counterflow configuration. The obtained results may be used in (spray) flamelet library or computations of flamelet generated manifolds in turbulent combustion. The mathematical model is based on the two-dimensional conservation equations, which are transformed into one-dimensional equations using a similarity transformation. The numerical simulation concerns the axi-symmetric configuration with an adaptive grid for the gas phase. Detailed models of all relevant processes are employed; in particular, a detailed chemical reaction mechanism is used, which comprises 35 species involving 294 elementary reactions. The chemical reaction scheme presented in this work was developed in [1]. The thermodynamic data for CH_4 and O_2 between 100 and 300 K are implemented for normal and elevated pressures for use in computations of cryogenic CH_4/LOX combustion. For the CH_4/air laminar flame, the present results are compared with results from literature to verify the mathematical model, chemical mechanism and the numerical scheme. The CH_4/O_2 flame is studied for elevated pressures up to 2 MPa. Both extinction strain rates and the scalar dissipation rates at stoichiometric conditions are evaluated for use in future turbulent flamelet computations. It is shown that oxygen dilution, pressure, and strain rate have a pronounced effect on flame structures, which becomes evident by studying the effects of liquid oxygen compared to gaseous oxygen on flame structure. The combustion of CH_4/LOX with preceding evaporation of liquid oxygen under cryogenic conditions has displayed a significant effect of the liquid phase on gas temperature. Moreover, the spray flame is broadened with increase of initial droplet size.

1 Introduction and Motivation

The understanding of physical and chemical processes in many science and engineering applications is crucial to ensure stability and efficiency of their performance. Droplet and spray processes play an important role in fields such as medicine, pharmacy, biological and agricultural systems [2–9]. In particular, these are used extensively in liquid-fuel combustion processes such as direct-injection engines [10–12], gas turbine combustors [13–15] and liquid rocket propulsion systems [16–18]. Typically, in such processes, either liquid fuels or a mixture of fuel and liquid oxidizer are injected as a spray into the combustion chamber, where combustion takes place and involves many complex phenomena, e.g. interaction between phases, transport characteristics of droplets and chemical reactions. One of the basic components of all these complex phenomena is the process of evaporation of a single droplet. Therefore, it is important to develop suitable numerical models that can predict and simulate the evaporation of a single droplet accurately.

Presently, combustion is, the major energy source of daily life and it will remain the major source in the future as well. Therefore, the knowledge about combustion phenomena is of great scientific interest due to its presence in a wide range of industrial processes. It is known that the combustion contributes the most in total energy sources of the world e.g. in 2006, about 90% of the worldwide energy support was provided by combustion of liquids (such as gasoline and hydrocarbon fuels), solids (such as coal and wood) and gases (such as natural gas containing mainly methane and small amounts of other hydrocarbons) [19]. The remaining 10% of the worldwide energy support was provided by energy sources such as nuclear or renewable energy. In recent years, the importance of the reduction of pollutant emissions has increased considerably due to both environmental consciousness and governmental policies. A direct contribution to reduce pollutant emissions can be made by improving the efficiency of combustion processes, thereby increasing fuel economy. In the past, much attention has been paid to carry out the research on combustion processes based on H_2/LOX or LH_2/LOX. These propellants, however, are expensive and difficult to store. In order to protect our environment, green propellants are further needed. Green propellants are those propellants which cause low pollution, roll out chlorides, nitrogen, nitric oxides, have no corrosive material and are easy to handle. Some examples of green propellants are CH_4, kerosene, propane, ethylene etc.

Therefore, the present work focuses on combustion processes based on green propellants. The propellant combination chosen is CH_4/LOX, because of its high performance, good characteristics at high temperature, lower cost than other propellants as well as

importance in technical applications. In particular the modeling and numerical simulation of such processes in order to provide the foundation for future combustion systems with reduced pollutants and increased efficiency is considered. Currently, many technical areas such as Plane and Space Industry, Space Shuttle Main Engine or Vulcaine Engine from Ariane 5 are using H_2/LOX propellants. Many experiments for turbulent combustion of H_2/LOX and CH_4/LOX have been carried out in ONERA France using the Mascotte burner [20–22] and DLR, Lampoldshausen, Germany using the M3 burner [23–25]. They are operating at cryogenic initial LOX temperature (85 K) and pressures up to 5.5 MPa, because of handling and storage difficulties as well as efficiency considerations.

The aim of this work is the numerical investigations of laminar CH_4/air, CH_4/O_2 and CH_4/LOX spray flames in counterflow configuration, which yields the advantages that include control of the transition from stable flames to local extinction conditions, compactness of the domain as compared to jet flames, which is worthwile from computational viewpoint and reduction of soot formation [26]. Furthermore, the detailed chemistry and detailed transport have been considered to seek realistic predictions of experimental data. In particular, simulations of laminar spray flames for different parameters such as droplet sizes, droplet velocities, strain rates and equivalence ratios are performed because they form a base for modeling of turbulent combustion, for instance, in (spray) flamelet computations of turbulent combustion or flamelet generated manifolds, which provide an accurate and efficient way for the modeling of turbulent flames. This method uses a chemical library based on one-dimensional unstrained flames to model the chemistry of a multi-dimensional turbulent flame [27].

Studying the behavior of single droplets is the most crucial part in comprehending the spray characteristics, therefore, it is studied separately in this work. Usually, a cold spray is injected into a hot environment. In this work, however a special case of experimental setup for a single spherical droplet suspended on horizontal and vertical glass fibers in cold air is considered. This experimental setup was designed at PCI (Institute of Physical Chemistry), Heidelberg for evaluation of its performance and mathematical model of droplet vaporization. Moreover, the experiments investigate the time-dependent variation of droplet size and LIF (Laser Induced Fluorescence) signal intensity as a function of time in laser-heated, fiber-suspended, Rhodamine-6G-doped water droplets (typical dye used for laser spectra). Therefore, numerical investigations for single droplet vaporization by laser heating are performed as well in order to validate the mathematical model for droplet vaporization, which is used in laminar spray computations in present study.

Furthermore, combustion of CH_4/air flames, CH_4/O_2 flames as well as CH_4/LOX laminar spray flames in counterflow configuration are investigated. Detailed models of all relevant processes are employed; in particular, a detailed chemical reaction mechanism is used in order to predict the profiles of all the chemical species involved in combustion processes. The CH_4/air system is investigated and the results are compared with literature results in order to validate the gas phase model. The CH_4/O_2 system is studied

for elevated pressures up to 2 MPa and different strain rates up to extinction. Parametric studies are performed for mono-disperse spray in counterflow configuration. They represent typical configurations after the vaporization occurs either through pressure or twin-fluid atomizers. Since the combustion of CH_4/LOX takes place in the flamelet regime of turbulent combustion, the resulting laminar flame structures can be used in turbulent diffusion flame studies employing the flamelet model for turbulent spray flames. Hence, the obtained results in this work contribute to a better understanding of droplet vaporization and spray combustion of laminar flames that lays foundation of studying turbulent spray flames, which are important in many technical applications.

In Chapter 2, a general overview of the single droplet vaporization and combustion is presented. The current status and focus of present work on droplet vaporization is discussed. The wide applications of combustion and, especially, spray combustion processes and their importance as well as the desired characteristics for green propellants are described. Moreover, state of the art in combustion and significance of present study is presented. In Chapter 3, the basic governing equations and the chemical model are described, for the gas phase as well as the liquid phase. In Chapter 4 the focus is on the specific equations for single droplet vaporization by laser heating and laminar CH_4/LOX spray combustion in counterflow configuration. The numerical algorithm for solving the equations is also described.

Chapter 5 presents the numerical simulation results and discussions. In particular, simulations for single droplet vaporization by laser heating as well as CH_4/LOX and CH_4/air in counterflow configuration are presented. Numerical results are compared with the experimental data and other results available in the literature. Finally, summary and conclusions are given in Chapter 6.

2 Droplet Vaporization and Combustion

2.1 Single Droplet Vaporization

The first step in understanding a spray must naturally be the understanding of its basic constituents: i.e. single droplets. Therefore, it is important to develop good numerical models that can predict and simulate the process of vaporization of a single droplet accurately. Moreover, experiments have to be carried out in order to validate the models. In this chapter, a combined experimental [28] and computational investigation [29] of the vaporization of water droplets induced by an infrared laser beam is carried out. In particular, a single spherical droplet is considered which is suspended on horizontal and vertical glass fibers in air under atmospheric pressure. The droplet heating and vaporization are induced by a pulsed CO_2 laser. The droplet size variation is observed as a function of time via direct visualization. The vaporization of single droplets by irradiation with a pulsed laser is extensively studied in the literature. For example CTR- Carinthian Tech Research AG [30] has developed a miniature laser that could easily replace the spark plug in the future, while improving performance and reducing fuel consumption and emissions. The main benefit of using laser ignition in internal combustion engines is that the laser can enhance the combustion process and minimize the pollutant formation [31–33]. The interaction of absorbing aerosols with pulsed laser beams has been studied in [34]. Approximate energy and mass conservation equations, neglecting the molecular absorption and scattering effects are developed and they will be applied to analyze the vaporization of aerosol droplets. In [35], a spherically-symmetric liquid droplet subject to a high-intensity pulsed laser flux has been investigated. A set of coupled equations for the droplet temperature, radius and beam intensity in the diffusive regime, assuming low-mass-flux conditions, has been set up. Other studies of vaporization of laser-irradiated droplets have been performed in [36] and [37]. In [36], the vaporization of small droplets irradiated by a long-pulsed laser beam has been numerically analyzed. A set of convective and diffusive transport equations is included in the generalized vaporization model. Thus, droplet vaporization has been studied over a wide range of beam irradiance, from low irradiance beams where isobaric diffusion and conductive energy transport dominate, to high irradiance beams where convective transport processes occur. In [37], sublimation and vaporization of a cylindrical ice particle, and vaporization of a spherical water droplet by laser radiation, has been well

investigated. The effects of a fiber or a suspender on the droplet vaporization are also discussed in some studies. In [38], vaporization of a suspended droplet in a convective high-pressure environment has been studied. A numerical model was developed to study the vaporization of droplets suspended in a hot nitrogen stream under different pressure conditions. The model used includes high-pressure effects, real gas effects, variable thermophysical properties, liquid phase internal circulation. However, there exist only few combined numerical and experimental studies of vaporization of laser-heated droplets, that are large compared to the wavelength of the laser light. In this chapter, the case of vaporization of a large droplet irradiated with a long-time laser pulse of low energy is studied. The purpose of using suspended droplets on glass fiber is to avoid the experimental difficulties of free falling droplets, such as keeping the heating rate constant and obtaining high resolution droplet images in real time. In [39], the effect of support fiber conduction on droplet vaporization in a weakly convective flow has been investigated. A numerical one-dimensional model of transient conduction is formulated together with vaporization of the droplet. It is shown that heat transport through the supporting fibers is an insignificant effect and the method of suspending the droplet on a glass fiber can be applied in experiments of droplet vaporization.

In the present work, vaporization of a single spherical droplet irradiation by a pulsed laser of different pulses widths is studied with the help of the so called uniform temperature field model [40]. Numerical simulations [29] and [41] are carried out and compared with experimental results from [28, 42]. As a result, it is shown that the uniform temperature field model is a suitable model for the investigated experimental setup, i.e., a large spherical H_2O droplet heated by a pulsed CO_2 laser.

2.2 Combustion in Space

The first propellants used for rocket propulsion, nearly 60 years ago, were combinations such as LOX(liquid oxygen)/ethanol or H_2O_2/ethanol [43]. These propellants were largely available, low cost and their characteristics, chemistry, physical and combustion properties were already well known. This experience contribute to the development of the first large operational rocket, the A-4 using LOX/ethanol.

After these initial steps, in order to increase the performance, the fuel was replaced by kerosene, both in USA and Russia. A wide range of rocket engines were designed e.g. RP-1, Saturn V, Atlas V, Falcon 1 and Falcon 9 [43], tested and used extensively in launchers. Several LOX/kerosene engines are still used, and an intense research activity in this area has been carried out in the last years [44–46]. To be cost effective, the need of less massive launcher vehicles with the highest possible performance brought to the choice of LOX/LH_2 propellant combination in several rocket stages. This cryogenic pair has by far the best specific impulse (vacuum Isp =4400 m/s). Rocket launcher stages like Centaur (Titan 4 upper stage), J-2 (Saturn 5 upper stage), STS Space Shuttle main stage, RD-0120 (Energia upper stage), H10 (Ariane 4 upper stage) and Vulcain (Ariane 5 main

stage) are all powered by the LOX/LH_2 propellant combination. For reusable launcher vehicles in particular, it represents a good choice in their design. Solid propellants generally have a very high density and, are storable and relatively easy to handle, but provide a low specific impulse (vacuum Isp = 2500 - 2900 m/s) and generate very high atmospheric pollution, where specific impulse is a way to describe the efficiency of rocket and jet engines. Moreover, solid propellants do not allow any thrust level control, as the thrust history is dictated by the grain design. Therefore, they are used in heavy launchers mainly as a support of the primary stage, and their employment on standalone engines is more difficult. Storable propellants such as nitrogen tetroxyde (N_2O_4), hydrazine and its derivatives (monomethylhydrazine MMH, unsymmetrical dimethylhydrazine UDMH) were first considered for military applications, because a missile using these propellants can be stored for years without propellant boiloff at ambient conditions. These have a good specific impulse (vacuum Isp = 2700-3200 m/s), a relatively high density and provide a safe and reliable ignition since no igniter is required for these hypergolic propellants (those that spontaneously ignite when they come into contact). The use of these propellants was extended to a range of launchers and upper stage engines, such as Vexin-A and Astris (Europa upper stages), Proton first and upper stage, Titan 2 through 4 first and upper stages, Viking (Ariane 1 through 4 main and upper stages) and Aestus (Ariane 5 upper stage). Their main drawback is that both propellants and combustion products are highly toxic. Actually, handling of propellants like N_2O_4, MMH and UDMH requires a high degree of precautions. The inhalation and contact of these chemically aggressive propellants is highly dangerous, and several precautions have to be taken (protective suits, purging of work places, feed lines, etc.). Additionally, their combustion products have a heavy environmental impact, as detailed in next section. As a replacement for both solid and liquid hypergolic propellants here described, a renewed effort in the study of nontoxic propellant combinations LOX/hydrocarbons (HC), including the wellknown LOX/kerosene, is being carried on recently. Several activities worldwide are aimed at the replacement of solid boosters and N_2O_4/Hydrazine (design studies are carried on for Ariane 5 liquid boosters in Europe, RS-76 for Liquid Flyback Booster, Fastrac engine for X-34, nontoxic Orbiter Maneuvering System and Reaction Control System (OMS/RCS) for Space Shuttle in USA [47], and several existing engines in Russia) with LOX/kerosene or LOX/methane engines. As shown in the next sections, kerosene and methane are the best candidates as nontoxic propellants.

2.2.1 Enviromental Impact

Before addressing the study of propellants and their properties, a first screening of possible propellants is made by identifying the criteria which define nontoxic propellants for rocket propulsion. Actually, several propellants, like LOX/hydrocarbons, produce carbon dioxide (CO_2). Although CO_2 is one of the main contributors to the greenhouse effect, the amount of CO_2 globally released by rocket launchers is quite small compared to industrial sources, and can be neglected [48]. On the other hand, solid boosters

produce chlorides (mainly HCl), hot metallic particulates (Al_2O_3), and high temperature N_2. Chlorides are responsible for the destruction of stratospheric ozone, as well as for acid rain. Aluminium oxide is also responsible for depleting the ozone layer, because it acts as a catalyst for the decomposition of ozone (O_3) in oxygen molecules. These emissions are far more dangerous than CO_2 for the environment, and should be avoided. Hypergolic propellants N_2O_4/hydrazine produce high temperature N_2 and NO, which react to NOX and nitric acid in the atmosphere, and emissions of this toxic exhaust gases are to be avoided. They contribute for acid rains and depletion of stratospheric ozone. LOX/methane and LOX/kerosene engines eliminate the production of harmful species, such as chlorides, Al_2O_3, and hot N_2 (which reacts to NOX and nitric acid in the atmosphere).

2.2.2 Green Propellants

Based on the above comparisons among solid, hypergolic and LOX/hydrocarbon propellants, it is possible to define a list of desired characteristics regarding non toxic propellants:

- Low pollution, thereby ruling out chlorides, metallic particulates like Al_2O_3, nitrogen (N_2) and nitric oxides (NOX) from the combustion products;
- Simple handling, without complicated and costly safety precautions;
- Extensive material compatibility, no corrosive or chemically aggressive behaviour.

These definitions restrict nontoxic propellants to a range of possible choices including:

- Liquid oxygen (LOX) or hydrogen peroxyde (H_2O_2) as an oxidizer.
- Hydrocarbons as a fuel, because of their composition (they contain only carbon (C), oxygen (O) and hydrogen (H) atoms, apart from impurities). Their combustion products do not contain any chlorides, metallic particulates or nitrogen.

Other characteristics are desirable; the following parameters contribute to propellant selection:

- The performance should be equal or better than hypergolic storable propellants (vacuum Isp $>$ 3400 m/s);
- The density should be as high as hypergolic propellants;
- The propellants should be either storable, or moderately cryogenic (critical temperatures not lower than 150 K);
- The propellant costs should be low, as compared to hypergolic or solid propellants.

The best performing fuels in relation with criteria mentioned above are identified as methane, propane and kerosene, in this order. For methane, the theoretical vacuum Isp reaches 3900 m/s, which is one of the highest possible values, though well below LOX/LH_2 specific impulse (around 4700 m/s) [48]. Thus, this comparative study will be limited to the following propellant combinations: LOX/methane, LOX/propane and LOX/kerosene.

2.2.3 Applications

To increase the performance and to reduce the costs in rocket propulsion, LOX/HC engines have been developed and improved over the last 50 years, especially as far as LOX/kerosene engines are concerned. They range from first stage engines (F-1, RD-170) to upper stage engines (RD-0109, RD-58M, LR-91-AJ-3) [48]. The F-1 was actually one of the largest liquid rocket engine ever built, used in the Saturn V rocket engine for the Apollo program. The RD-170 is still employed in Russia, and delivers one of the highest thrust levels ever achieved by a liquid rocket engine. The LOX/kerosene propellant pair was used both in USA and in Russia, and some work also took place in Europe (RZ-2, P111). Only in 1985, with the Russian engine RD-170/171, high combustion chamber pressures were attained (critical pressure p_c = 24.5 MPa). These advanced rocket engines were envisaged for the EnergiaBuran reusable space system, developed as a system intended to reach the capabilities of the US Shuttle system [49]. Research about the LOX/methane propellant combination began relatively recently in the last decade of twentieth century, and has taken place especially in Russia [49].

Some engines are reconverted LOX/kerosene engines, the others are brand new engine designs. Although none of these engines have yet reached the production stage, a huge effort is being made by both Russia and USA in the development of LOX/methane liquid rocket engines. In Russia, methane is widely available in form of liquefied natural gas which is predominantly methane that has been converted temporarily to liquid form for ease of storage or transport, at a very low cost (LNG) [50], and this is one of the reasons for extensive study in this country. In USA, preliminary studies on the use of LOX/methane have been performed since 1980's [51]. In Europe, several comparative studies have been performed on LOX/hydrocarbon engines in recent years [44, 51, 52].

2.2.4 Combustion of Spray Flames

In the recent years, methane (CH_4) is considered as an alternative fuel to hydrogen in liquid rocket propulsion systems [20,21,23–25,53–59]. On CH_4/LOX nonpremixed flames in counterflow configuration using transcritical conditions, in [53], a methodology was proposed and illustrated for calculations of strained flames. This methodology discusses the mass transfer and heat release for the flame that is formed in the counterflow of a stream of cold oxygen injected at a temperature which is below critical and impinges on a supercritical stream of CH_4. Oxygen is injected at transcritical state (T = 80 K) and

CH_4 at 300 K at a pressure of 7 MPa. It was seen that the flame thickness was about 0.9 mm while the reaction layer thickness was about 0.6 mm for this relatively low level of strain rate (about 20 s^{-1}).

There are two major research groups in Europe which experimentally investigate the CH_4/O_2 and LOX/CH_4 flames: ONERA in France and DLR Lampoldshausen in Germany. Both ONERA's MASCOTTE test facility [20] and the DLR's M3 combustion chamber ([25]), which initially were developed for experimental investigations of liquid oxygen/hydrogen combustion (LOX/H_2), have been modified to allow for the study of LOX/CH_4. In these investigations, pressure ranges from 0.1 to 5.5 MPa, the injection temperature for LOX is 85 K, and for liquid CH_4 it is 125 K, hence both temperatures are cryogenic. A recent study [21] concerns fuel rich conditions. [54] studied the flame structure of both LOX/CH_4 and LOX/H_2 in the transcritical range for a pressure range between 0.1 to 7 MPa and a subcritical injection temperature of liquid oxygen. Combustion of cryogenic oxygen and methane injected at pressures between 4.5 and 6 MPa were investigated experimentally by [55]. The coaxial injector delivers oxygen at a temperature of 85 K and methane at a temperature of 120 K or 288 K. Stabilization of flames formed by cryogenic liquid oxygen/hydrogen or methane has been investigated through planar laser induced fluorescence (PLIF) of OH [56]. In the LOX/H_2 experiments, injection conditions are transcritical, since the chamber pressure (6.3 MPa) is above the critical value, whereas the temperature (80 K) is below the critical value. In the LOX/CH_4 experiments, the chamber pressure (2 MPa) and LOX injection temperature (80 K) are below critical values.

In the DLR experiments [25], a comparison between spray combustion for coaxially injected CH_4/LOX and H_2/LOX, at similar injection conditions was performed where the Weber number and the momentum flux ratio were varied. Experimental investigations [23] on the development of LOX/CH_4 flames, especially ignition and flame stabilization, strongly coupled with the distribution of liquid oxygen phase before and after the occurrence of ignition, were carried out. [57] experimentally investigated cryogenic reactive coaxial sprays with oxygen and hydrogen or methane in order to determine if concepts from H_2/LOX injector design can be transferred to LOX/CH_4. The experimental study of the ignition and flame stabilization of a gaseous methane/oxygen jet for different configurations and injector conditions is described by [24].

Lux *et.al.* [58] investigated flame stabilization in CH_4/LOX combustion using a single shear coaxial injector during both ignition and steady-state operation. Three main operating points of sub-, near-, and supercritical conditions with respect to thermodynamic critical point of oxygen were considered, whereas LOX was injected at about 120 K and CH_4 was injected at near ambient temperature of about 270 K. Taking into account the slightly different experimental setup and operating conditions in comparison with previous H_2/LOX investigations [58], these results are in good conformance with those for H_2/LOX flames. [59] experimentally studied the effect of a moderately recessed LOX tube on the flame stabilization in CH_4/LOX combustion at the same operation conditions as used by [58], using an optically accessible combustion chamber equipped with

a single-shear coaxial injector. It was observed that a recessed LOX post significantly increases the flame expansion shortly after injection.

Even though applications typically involve turbulent flow fields, laminar flames are studied extensively to investigate principal flame characteristics in a simple geometry. The evidence gained from these investigations then is included in both experimental and numerical configurations.

Combustion of laminar CH_4/air, CH_4/O_2 as well as CH_4/LOX spray flame in counterflow configuration, is extensively studied in the literature. Several authors studied the behavior of laminar CH_4/air in counterflow configurations at different conditions and using different chemical mechanisms. For instance, in [60] numerical results for laminar CH_4/air diffusion flame have been presented. A starting kinetic mechanism, a 5-step mechanism and a 4-step mechanism have been used. The starting mechanism used there is essentially the C_1 mechanism, including 39 reactions which involve 17 species. The conditions used in their simulations are: pressure is 0.1 MPa, the temperature at both boundaries is 298 K, the mass fractions of fuel and oxygen is $Y_{F,\infty} = 1$ respectively $Y_{O_2,-\infty} = 0.233$ and different strain rates until extinction are used. Starting with a 3-step reduced chemistry, a simplified formulation aimed at facilitating numerical computations of nonpremixed CH_4/air have been developed in [61]. In order to remove the stiffness associated with the fast fuel consumption, the conservation equations for the major species and the temperature are written in terms of generalized coupling functions, which corresponds to generalized Burke-Schumann formulation. The conditions used in the simulations are: pressure is 0.1 and 4 MPa, the temperature at both boundaries is 300 K and the mass fractions of fuel and oxygen $Y_{F,\infty} = 1$ respectively $Y_{O_2,-\infty} = 0.233$ at strain rates of 10 and 500 s^{-1}. Furthermore, effects of pressure on the structure and consumption rate of nonpremixed strained flames are studied in [62], which concluded based upon fast chemistry limit, that the flame thickness is inversely proportional to the square root of pressure and that the flame structure may be described in terms of a similarity variable that scales to the square root of the product of pressure and strain rate. This exponent is independent of finite rate chemistry effects, except when conditions are close to extinction. In [63], the effect of flame structure on the extinction limits of CH_4-O_2-N_2 counterflow diffusion flames are investigated experimentally and numerically by varying the mixture fraction between 0.055 (methane-air flame) and 0.78 (enriched methane-oxygen flame). In this study, the C_1 mechanism, which gives an extinction strain rate of 494 s^{-1} for methane-air flame and 1488 s^{-1} for diluted methane-oxygen flame, has been used for the numerical simulations. Flame structure, extinction characteristics, and nitric oxide (NO) formation in diffusion flames of methane and air have been numerically investigated in [64]. The effect of pressure on NO emission is emphasized in high-temperature and diluted-air conditions. The simulations are performed with the GRI-Mech 2.11 which consists of 279 elementary reactions and 49 species, for different pressures and oxygen temperatures. Numerical and experimental studies on radical concentrations were performed in [65] and [66]. In [65], linear laser-induced fluorescence has been applied to obtain spatially resolved profiles of CH radicals in laminar methane/air

and methane/nitric oxide/air counterflow diffusion flames at atmospheric pressure and strain rates from 59 to 269 s^{-1}. The experiments have been compared with predicted CH levels obtained using the GRI-Mech. 3.0 chemical kinetic mechanism. In [66], issues related to the computation and measurement of CH, CH^* and OH^* in a laminar flame have been discussed. Experimentally, CH radical concentrations were measured with laser-induced fluorescence, whereas CH^* and OH^* concentrations were measured through flame emission. For the simulations, the GRI-Mechanism 2.11 chemical kinetic mechanism has been used and the results have been compared with experiments.

Other studies [67–70] specifically investigated the effect of enriched oxygen flames. For example, [67] and [68] investigated oxygen-enhanced methane counterflow flames through both optical diagnostics and numerical simulations. The effect of strain rate and the influence of oxygen concentration in the oxidizer on the flame structure were studied for nitrogen-diluted methane (20% CH_4 and 80% N_2). The strain rate varies from 60 to 168 s^{-1} while in the oxidizer stream, the nitrogen in air is replaced by oxygen ranging from 23% O_2 to 100% O_2. For the simulations, the GRI 3.0 kinetic mechanism was used. Beltrame *et. al.* [70] studied soot formation in oxygen-rich counterflowing methane-oxygen diffusion flames. They found that soot formation in methane flames is enhanced by oxygen enrichment. With increase of the oxygen in the oxidizer stream, the soot zone narrows and is shifted towards the stagnation plane. An extension of the GRI 2.11 mechanism including chemical reactions with species up to C_6, thus consisting of 365 reactions among 62 chemical species, was used. A soot map that separates the non-sooting from sooting regions for laminar counterflow methane-oxygen-nitrogen diffusion flames at atmospheric pressure is given by [69]. Soot formation is studied at a constant strain rate of 20 s^{-1} as a function of the methane content ranging from 25% to 100% in nitrogen in the fuel stream and as a function of oxygen diluted in nitrogen from 35% to 100% in the oxidizer stream.

In the present work, the numerical investigation of laminar oxygenated CH_4/air as well as CH_4/O_2 flames as well as intermediate degrees of oxygen dilution in the counterflow configuration is performed. For the CH_4/O_2 system a flamelet library for turbulent combustion is generated for use in turbulent spray computations at normal and elevated pressure. Evaluation of extinction conditions are presented, which are very important for use in turbulent flamelet computations. Moreover, the nitrogen/oxygen ratio is varied. Physical properties of methane at cryogenic inlet conditions are considered which are typical for liquid rocket propulsion systems. These properties are parameterized for use in LOX/CH_4 computations. Moreover, structures of LOX/CH_4 spray flames for different initial droplet sizes are discussed.

3 Governing Equations for Reactive Two-Phase Flows

3.1 Description of the Gas Phase

In this section, general three-dimensional conservation equation for mass, energy and momentum are derived. These are the Navier-Stokes equations for reactive flows [1, 71, 72].

3.1.1 General Equations of the Gas Phase

In this section, a general formulation for the conservation equations for the extensive variables mass, energy and momentum is derived based on balance considerations in a given control volume. Such balance describes the change of the extensive variable $\Phi(t)$, which corresponds to the quantities that should be conserved such as mass, momentum, energy etc, in the control volume Ω_{CV} at time t. The change in $\Phi(t)$ can be caused by three different processes: change caused by a flux $\vec{F}_{\Phi}\dot{\vec{n}}\mathrm{d}S$ through the surface $\partial\Omega_{\mathrm{CV}}$, by a production q_{Φ} within the volume element, or by long range processes s_{Φ} acting on the control volume. The transport of the variable Φ through the surface of the control element volume can be realized by diffusion, convection and heat conduction. A production of Φ within the volume element takes place by chemical reactions or also by phase change in two phase flows. The sprays must satisfy the condition that their volume flux is negligible in comparison with the volume flux of the gas phase, such that the fluid density corresponds to the gas density [72]. For long range processes, such as energy transport by heat radiation, gravity and electromagnetic forces are considered. Considering an extensive variable $\Phi(t)$, it can be calculated from the corresponding density $\phi(\vec{r}, t) = d\Phi(t)/dV$ by integration over the whole control volume element Ω_{CV} [1, 19]

$$\frac{\partial\Phi}{\partial t} = \int\limits_{\Omega_{\mathrm{CV}}} \frac{\partial\phi}{\partial t} dV, \tag{3.1}$$

where dV denotes a differential volume element. The overall balance of variable Φ can be obtained by integration of the flux over the surface $\partial\Omega_{\mathrm{CV}}$ and integration of production terms and long range processes over the control volume element Ω_{CV}:

$$\underbrace{\int_{\Omega_{\mathrm{CV}}} \frac{\partial \phi}{\partial t} dV}_{\text{Time change}} + \underbrace{\int_{\partial\Omega_{\mathrm{CV}}} \vec{F}_\Phi \vec{n} dS}_{\text{Flux}} = \underbrace{\int_{\Omega_{\mathrm{CV}}} q_\Phi dV}_{\text{Production}} + \underbrace{\int_{\Omega_{\mathrm{CV}}} s_\Phi dV}_{\text{Long range process}} , \tag{3.2}$$

where dS denotes the surface element of the control surface $\partial\Omega_{\mathrm{CV}}$, V is the control volume, and q_Φ and s_Φ denote source terms for quantities Φ and long range processes acting upon control volume V, respectively. Using the Integral Law of Gauss, the surface integral for the change of Φ by the flux $\vec{F}_\Phi$, can be expressed as follows:

$$\int_{\partial\Omega_{\mathrm{CV}}} \vec{F}_\Phi \vec{n} dS = \int_{\Omega_{\mathrm{CV}}} \mathrm{div} \vec{F}_\Phi dV. \tag{3.3}$$

If an infinitesimally small volume element is considered, then the limiting process $\Omega \to 0$ yields the following equation:

$$\frac{\partial \phi}{\partial t} + \mathrm{div} \vec{F}_\Phi = q_\Phi + s_\Phi. \tag{3.4}$$

This general equation is used in the following to derive the conservation equations for mass, momentum, energy, and species mass.

3.1.1.1 Mass Conservation

The mass conservation equation is usually called continuity equation. It states that the mass of a closed system will remain constant, or an equivalent statement is that the matter cannot be created nor destroyed, although it may be rearranged. In the following equation (3.4) is considered in order to derive the continuity equation. If the extensive variable $\Phi(t)$ is the total mass of the system ($\Phi = m$) then the density of the extensive mass m is given by the mass density ρ, ($\phi = \rho$). The mass flux density is given by $\vec{F}_m = \rho \vec{v}$, where $\vec{v}$ is the local flow velocity.

For the case of two phase flow modeling, a production term q_m in the continuity equation is included, which describes the mass exchange between liquid phase and gas phase during the evaporation or the condensation processes, respectively. The definition of phase exchange term in all conservation equations will be given in Section 4.2.2.2. In the mass conservation equation, there is no long-range process term because of the fact that mass can neither be formed nor destroyed during chemical reactions. Therefore, only the source term q_m for mass m contributes due to the exchange of mass between gas and liquid phase caused by evaporation or condensation.

Taking these considerations into account, and substituting the corresponding quantities, i.e. $\Phi = m$, $\phi = \rho$, $F_m = \rho v$, one obtains from equation (3.4) the continuity equation [1, 19]:

$$\frac{\partial \rho}{\partial t} + \mathrm{div}(\rho \vec{v}) = q_m. \tag{3.5}$$

3.1.1.2 Species Mass Conservation

If the masses of different species m_i are considered, their density ϕ is given by the partial mass density $\rho_i = Y_i \rho$, where $Y_i = m_i/m$ is the mass fraction of species i. The local flow velocity $\vec{v}_i$ can be written as follows:

$$\vec{v}_i = \vec{v} + \vec{V}_i. \tag{3.6}$$

In equation (3.6), $\vec{v}$ is the mean flow velocity of the center of mass and $\vec{V}_i$ represents the diffusion velocity. The total flux density is composed of a convective part $\vec{F}^K_{m_i} = \rho_i \vec{v}$ and a diffusive part $\vec{F}^D_{m_i} = \rho_i \vec{V}_i$. The diffusive part of the total flux splits in two components, the flux density caused by the molecular diffusion $\vec{j}_i$ and the flux density caused by thermal diffusion $\vec{j}^T_i$. The diffusion velocity $\vec{V}_i$ is the sum of both flux densities divided by the density. In the species mass conservation equation a long-range process term does not exist. As in the continuity equation, a production term must be involved due to the phase exchange, which can be written for spray as:

$$q_{m_i} = \delta_{is} q_m, \tag{3.7}$$

where δ_{is} is the Kronecker symbol, which assumes the numerical value of one if the balance as a spray is formulated, (index 's'), and otherwise the numerical value of zero. Additionally, there is a production term given by

$$q_{m_i,c} = W_i \dot{\omega}_i \tag{3.8}$$

which describes the formation and consumption by chemical reactions. Here, W_i denotes the molar mass and $\dot{\omega}_i$ is the molar rate of reaction of species i. If one substitutes the corresponding quantities in equation (3.4), then the species mass conservation equation [1, 19] is obtained:

$$\frac{\partial \rho_i}{\partial t} + \mathrm{div}(\rho_i \vec{v}) = -\mathrm{div}(\vec{j}_i + \vec{j}^T_i) + W_i \dot{\omega}_i + \delta_{is} q_m. \tag{3.9}$$

With the help of following relations

$$\sum_{i=1}^{K} Y_i = 1, \tag{3.10}$$

$$\sum_{i=1}^{K} (\vec{j}_i + \vec{j}^T_i) = 0, \tag{3.11}$$

$$\sum_{i=1}^{K} W_i \dot{\omega}_i = 0, \tag{3.12}$$

it can be easily shown that adding up the terms in equation (3.9) over the all components K results in the continuity equation (3.5).

3.1.1.3 Momentum Conservation

In the momentum conservation equation, an extensive vector variable $\vec{\Phi}_p = m\vec{v}$, i.e. the momentum, is considered. The momentum density is given by $\vec{\phi}_p = \rho\vec{v}$. The momentum flux density $\overline{\overline{F}}_p$ consists of two parts, a convective part $\rho\vec{v} \otimes \vec{v}$ and a part $\overline{\overline{p}}$, which describes the momentum change due to frictional force and pressure. The symbol $\otimes$ denotes the dyadic product [1] between two vectors. The source term due to the phase exchange $\vec{q}_p$ is given in Section 4.2.2.2. There is also a long-range process term, namely the gravity $\vec{s}_p = \rho\vec{g}$, where $\vec{g}$ is the gravitational acceleration. Inserting all terms into the general equation (3.4), yields the momentum conservation equation [1, 19]

$$\frac{\partial(\rho\vec{v})}{\partial t} + \mathrm{div}(\rho\vec{v} \otimes \vec{v}) = -\mathrm{div}\overline{\overline{p}} + \rho\vec{g} + \vec{q}_p. \tag{3.13}$$

3.1.1.4 Energy Conservation

In the following, using again the general conservation equation (3.4), a conservation equation for the total specific energy e is derived. This equation can be reformulated into an equation for the specific enthalpy.

The terms in equation (3.4) are defined as follows: The energy density is given by $\phi_e = \rho e$, the energy flux density $\vec{F}_e$ is composed of three terms. A convective term $\rho e\vec{v}$, a term $\overline{\overline{p}}\vec{v}$, which describes energy changes due to pressure and viscous dissipation, and a term which takes into account the heat conduction ($\vec{j}_e$ - heat flux density).
Because of the energy exchange between the gas phase and liquid phase, the production term q_l, is also included in the energy conservation equation. As before, a long range term is formulated, which is the energy change due to radiation, q_r.
Substituting all terms into general equation (3.4), yields the energy conservation equation

$$\frac{\partial(\rho e)}{\partial t} + \mathrm{div}(\rho e\vec{v} + \vec{j}_e) + \mathrm{div}(\overline{\overline{p}}\vec{v}) = q_e + q_r. \tag{3.14}$$

The total energy density, e, is given as a sum of the kinetic energy $\frac{1}{2} \mid \vec{v} \mid^2$, the potential energy G and the specific internal energy u_{in} [1]:

$$e = \frac{1}{2} \mid \vec{v} \mid^2 + G + u_{\mathrm{in}}, \tag{3.15}$$

where G is the gravitational potential, $\vec{g} = \text{grad}\, G$, and u_{in} is the specific internal energy. The following relation is obtained by inserting the definition of total specific energy (3.15) in the energy equation (3.14) and using continuity and momentum equations

$$\rho h = \rho u_{in} + p, \tag{3.16}$$

where p denotes the pressure and h the specific enthalpy. Hence, the conservation equation for the specific enthalpy h is given by [73, 74]

$$\begin{aligned} \frac{\partial(\rho h)}{\partial t} - \frac{\partial p}{\partial t} + \text{div}(\rho h \vec{v} + \vec{j}_e) + \bar{\bar{p}} : \text{grad}\vec{v} - \text{div}(p\vec{v}) \\ = \left(\frac{1}{2} \mid \vec{v} \mid^2 - G\right) q_m - \vec{v}\vec{q}_p + q_e + q_r, \end{aligned} \tag{3.17}$$

where " : " denotes the contraction of two tensors leading to a scalar.

3.1.1.5 Closure of the System of Equations

A system of equations is said to be closed if it can be solved, for all variables that it involves, without imposing any additional constraint. In other words, a system of equations is closed if number of linearly independent equations is equal to the number of variables. The conservation equations of total mass, mass of chemical species, momentum and energy will be closed by ideal gas law. The ideal gas law gives the gas density ρ as a function of pressure p and temperature T:

$$\rho = \frac{p\overline{W}}{RT}, \tag{3.18}$$

where R is the general gas constant and $\overline{W}$ is the molar mass of the mixture given by:

$$\overline{W} = \left(\sum_{i=1}^{K} \frac{Y_i}{W_i}\right)^{-1}. \tag{3.19}$$

where K is the number of chemical species in the system and W_i is the molecular weight of the species i.

3.1.2 Transport Processes in the Gas Phase

3.1.2.1 Mass Transport

Diffusion is composed of three parts, a part $\vec{j}_i^D$, describing the molecular diffusion, a part $\vec{j}_i^T$, caused by thermal diffusion, and a part $\vec{j}_i^P$, caused by pressure diffusion. The molecular part is given by Fick's first law [74, 75]:

$$\vec{j}_i = -\frac{\rho D_i}{\overline{W}} \mathrm{grad}(Y_i \overline{W}), \tag{3.20}$$

where D_i is the diffusion coefficient of species i into the mixture.

The transport of the chemical species by thermal diffusion is the effect of a temperature gradient, called also Soret Effect. The part caused by thermal diffusion is dependent on the thermal diffusion coefficient D_i^T, and it can be expressed as follows [74, 75]:

$$\vec{j}_i^T = -\frac{D_i^T}{T} \mathrm{grad}(T). \tag{3.21}$$

Usually, the pressure diffusion part can be neglected in combustion processes. In addition, when the diffusion mass fluxes $\vec{j}_i$ and $\vec{j}_i^T$ are divided by the density, the resulting equation expresses diffusion velocity:

$$\vec{V}_i = -\frac{D_i}{\overline{W}} \mathrm{grad}(Y_i \overline{W}) - \frac{D_i^T}{\rho T} \mathrm{grad}(T). \tag{3.22}$$

The expression given in equation (3.22) is derived in [75].

3.1.2.2 Momentum Transport

An empirical equation for the transport of momentum describes the relation between the stress state and the deformation state of a control volume element. The stress state is determined through the involved surface forces which depend on the deformation state. If relaxation is neglected, the dynamic viscosity μ is the only transport property. Assuming that the fluid behaves as a Newtonian fluid (all gases as well as some liquids, e.g. water, fulfill this assumption), then the stress state through the pressure tensor is described as following:

$$\overline{\overline{p}} = p\overline{\overline{E}} + \overline{\overline{\Pi}}. \tag{3.23}$$

Here, $\overline{\overline{E}}$ denotes the unit matrix and p the hydrostatic pressure. The product $p\overline{\overline{E}}$ describes the hydrostatic part and $\overline{\overline{\Pi}}$ the viscous part of the pressure tensor. The viscous part is given by [1]:

$$\overline{\overline{\Pi}} = -\mu[(\mathrm{grad}\vec{v}) + (\mathrm{grad}\vec{v})^T] + \frac{2}{3}\mu(\mathrm{div}\vec{v})\overline{\overline{E}}. \tag{3.24}$$

In equation (3.24), μ denotes the dynamic viscosity of the mixture, the first term of the equation represents the deformation tensor, which contains the strain velocities.

3.1.2.3 Energy Transport

The heat flux $\vec{j}_e$ is the sum of three different parts, a part $\vec{j}_e^c$ which denotes flux caused by heat conduction, a part $\vec{j}_e^D$ which denotes flux caused by the Dufour effect, and $\vec{j}_e^d$ denotes flux caused by diffusion. Usually the Dufour effect can be neglected in combustion processes. The heat flux caused by heat conduction, $\vec{j}_e^c$ is given by:

$$\vec{j}_e^c = -\lambda \text{grad} T, \tag{3.25}$$

where λ is mixture thermal conductivity. The heat flux during diffusion is given by:

$$\vec{j}_e^d = \rho \sum_{i=1}^{K} h_i \vec{V}_i. \tag{3.26}$$

Here, h_i denotes the specific enthalpy of species i and $\vec{V}_i$ is the diffusion velocity and it is given in equation (3.22).

3.2 Description of the Liquid Phase

Between the liquid phase and gas phase, mass, momentum, and energy are exchanged due to vaporization of droplets and possibly due to condensation on the droplet surface. The coupling between these two phases occurs by source terms in the conservation equations of the gas phase. The vaporization source terms depend on the vaporization rate $\dot{m}$ and energy $\dot{q}$, which are required for the phase change. These two quantities have to be determined by the model for the vaporization process.

3.2.1 Droplet Vaporization

Abramzon and Sirignano [76,77] developed a model for the vaporization of fuel droplets in a convective environment (ambient gas with temperature higher than droplet), for pressures up to 1 MPa. The film theory is applied in order to take into account the convection caused by the relative droplet motion in the gas flow. It is assumed, that the droplet is surrounded by a film also called boundary layer. This film is used in order to model the resistance when mass and energy is exchanged in the gas phase (see Figure 3.1).

The film thickness δ_{M0} and δ_{T0} for the diffusive and thermal exchange, respectively, are computed as follows [78]:

$$\delta_{M0} = \frac{2R}{\text{Sh}_0 - 2}, \qquad \delta_{T0} = \frac{2R}{\text{Nu}_0 - 2}, \tag{3.27}$$

where R is the droplet radius. The Sherwood number Sh_0 describes the ratio of convective mass transport to diffusive mass transport. The Nusselt number Nu_0 describes

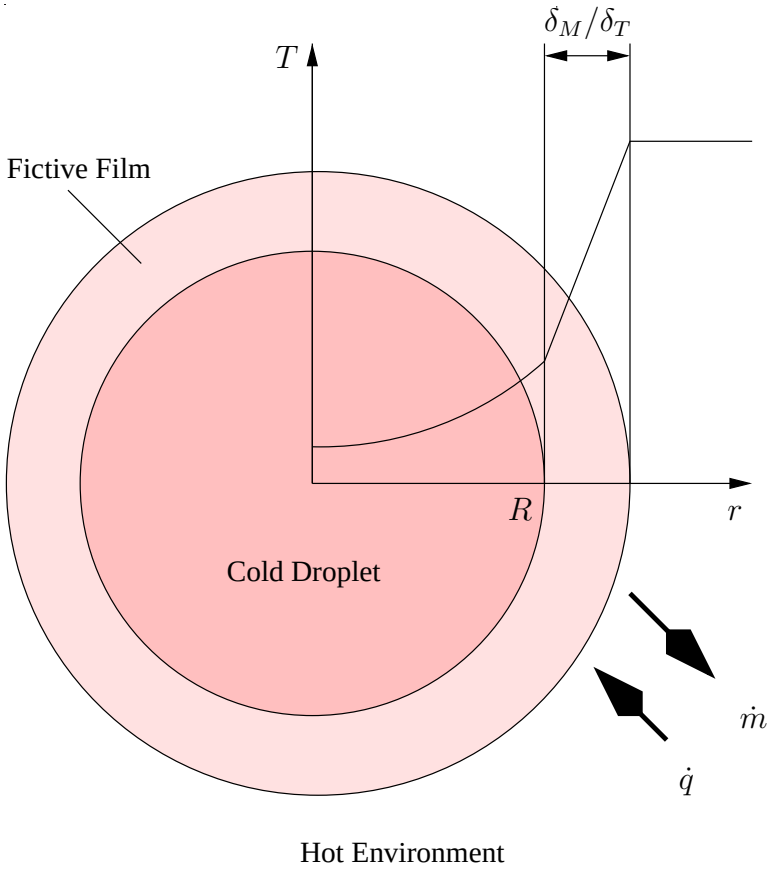

Figure 3.1: Scheme of a single vaporazing droplet in a hot and convective environment surrounded by a fictive film.

ratio between convective and conductive heat transfer. The index "0" is used, if the mass flow of the evaporating component (so called Stefan-flow) is not considered. Clift *et al.* [79] suggested the following relations for the computation of Sh_0 and Nu_0:

$$\mathrm{Sh}_0 = 1 + (1 + \mathrm{Re}\ \mathrm{Sc})^{\frac{1}{3}} f(\mathrm{Re}) \tag{3.28}$$

$$\mathrm{Nu}_0 = 1 + (1 + \mathrm{Re}\ \mathrm{Pr})^{\frac{1}{3}} f(\mathrm{Re}), \tag{3.29}$$

where the function of droplet Reynolds number $f(\mathrm{Re})$ is given by:

$$f(\mathrm{Re}) = \max(1, \mathrm{Re}^{0.077}) \quad \text{and} \tag{3.30}$$

$$\mathrm{Re} = \frac{2R\rho|\Delta\vec{v}|}{\mu_{g,f}}. \tag{3.31}$$

Here, R denotes the droplet radius, ρ is the density and μ denotes the dynamic viscosity. Thus, for the computation of droplet Reynolds number, the density of gaseous environment and the dynamic viscosity in film is used. When the relative velocity between droplet and gaseous environment is everywhere zero ($\Delta\vec{v} = 0$), then the Reynolds number is zero and Sh_0 and Nu_0 take the value 2 for a spherical droplet. The vaporization causes an expansion of the surrounding laminar boundary layer [78]. Therefore, the Sherwood number and the Nusselt number are adapted as follows:

$$\widetilde{\mathrm{Sh}} = 1 + (\mathrm{Sh}_0 - 2)/F_M, \qquad \widetilde{\mathrm{Nu}} = 1 + (\mathrm{Nu}_0 - 2)/F_T, \tag{3.32}$$

where F_M and F_T are correction factors. These factors describe the relative change of the film thickness through the Stefan-flow as follows:

$$F_M = \frac{\delta_M}{\delta_{M0}}, \qquad F_T = \frac{\delta_T}{\delta_{T0}}. \tag{3.33}$$

In [77], a universal function

$$F(B) = (1 + B)^{0.7} \frac{\ln(1 + B)}{B} \tag{3.34}$$

has been provided, which delivers the correction factors by $F_M = F(B_M)$ and $F_T = F(B_T)$.

The transfer numbers are functions of the concentration gradient of the evaporated components and the temperature gradient between droplet surface and gas. Note that, in this work, the evaporating component is liquid oxygen and the fuel is methane. In conventional technical applications as internal combustion engines or gas turbine combustion chambers, however, liquid fuel is injected in oxidant air. Therefore, the transfer number B_M is dependent on the oxygen mass fraction on the droplet surface $Y_{O_{2,s}}$ and on the surrounding Y_{O_2}, and the transfer number B_T is dependent on the specific heat capacity of oxygen in the film $c_{p,O_{2,f}}$ and on the latent heat of vaporization $L_{v,O_2}(T_s)$ at the droplet surface temperature T_s [80]. In particular:

$$B_M = \frac{Y_{O_{2,s}} - Y_{O_2}}{1 - Y_{O_{2,s}}}, \qquad B_T = \frac{c_{p,O_{2,f}}(T - T_s)}{L_{v,O_2}(T_s) + \dot{q}/\dot{m}}. \tag{3.35}$$

The latent heat of vaporization of oxygen is not only dependent on temperature but also strongly depends on the pressure [81]. For pressures higher than the critical pressure, the latent heat of vaporization is around zero (see Figure 3.9). A mass balance around the droplets provides an equation for the evaporated mass flow [82]:

$$\dot{m} = 2\pi\rho_f D_f R \, \widetilde{\mathrm{Sh}} \, \ln(1 + B_M). \tag{3.36}$$

Using energy conservation, the equation (3.36) becomes:

$$\dot{m} = 2\pi \frac{\lambda_f}{c_{p,O_{2,f}}} R \cdot \widetilde{\mathrm{Nu}} \cdot \ln(1 + B_T). \tag{3.37}$$

Equating (3.36) with (3.37), one gets the following relation for B_T:

$$B_T = (1 + B_M)^{\Phi} - 1 \tag{3.38}$$

with

$$\Phi = \frac{1}{\mathrm{Le}_f} \frac{c_{p,O_{2,f}}}{c_{p,f}} \frac{\widetilde{\mathrm{Sh}}}{\widetilde{\mathrm{Nu}}} \tag{3.39}$$

and

$$\mathrm{Le}_f = \left(\frac{\mathrm{Sc}}{\mathrm{Pr}} \right)_f = \left[\frac{\lambda}{c_{p,O_2} D} \right]_f . \tag{3.40}$$

The Lewis number Le_f depends only on film properties. From the droplet surface an exchange of mass and transport data is being applied through the film thickness and the average film temperature T_f as well as the average mass fractions in the film $Y_{i,f}$ are determined hereby by applying the so called "1/3 rule" [82, 83].

$$T_f = T_s + \frac{1}{3}(T - T_s), \tag{3.41}$$

$$Y_{i,f} = Y_{i,s} + \frac{1}{3}(Y_i - Y_{i,s}). \tag{3.42}$$

Investigations in [83] have shown that the factor 1/3 is an appropriate value, even though it has no physical interpretation. The decrease of the droplet mass is described as follows:

$$\dot{m} = -\frac{d}{dt}(\frac{4}{3}\pi R^3 \rho_l). \tag{3.43}$$

Differentiating equation (3.43) with respect to time and re-arranging, the expression for rate of change of the droplet radius in time ca be written as

$$\frac{dR}{dt} = -\frac{\dot{m}}{4\pi\rho_l R^2}. \tag{3.44}$$

Equating (3.36) and (3.44), relation for the change of droplet radius in time is obtained:

$$\frac{dR}{dt} = -\frac{\rho_f D_f}{2\rho_l R} \widetilde{\mathrm{Sh}} \cdot \ln(1 + B_M). \tag{3.45}$$

The energy flux $\dot{q}$, which heats up the droplet, can be computed as follows:

$$\dot{q} = \dot{m} \left(\frac{c_{p,f}(T - T_s)}{B_T} - L_{v,O_2}(T_s) \right). \tag{3.46}$$

Thus, the exchange of mass and energy between droplet and surrounding gas is described in detail.

3.2.2 Droplet Heating

The process of droplet heating influences the vaporization process via the time varying surface temperature T_s. There are three commonly used models in the literature to model the energy transport in droplets: the Thin Skin Model, the Uniform Temperature Model and the Conduction Limit Model.

The assumption for the Thin Skin Model (TS) is that the life time of the droplet is much shorter than the time required to transport energy into the droplet interior. As a consequence of this assumption, the droplet temperature remains at its initial value during the vaporization process. The droplet surface area decreases linearly in time. This behavior is known as the d^2- law [84, 85]. This model is applicable to liquids with low boiling points and for moderate temperatures.

In contrast to the Thin Skin Model, the Uniform Temperature Model (UT) is based on the assumption that the life time of the droplet is much longer than the time for the energy transport in the droplet. This is equivalent with the assumption of an infinite liquid heat conductivity. The temperature profile in the interior of the droplet is uniform but changes over time. This model is applicable for very small droplets with high thermal conductivity in a high-temperature environment [86].

The most realistic behavior is described by the Conduction Limit Model, which lies in between The Thin Skin Model and The Uniform Temperature Model. The Conduction Limit Model (CL) [87–89] addresses the radial energy transport in the droplet interior. The liquid temperature is not only a function of time but also changes as a function of the droplet radius. The disadvantage of this model is the higher computational cost since a partial differential equation for the energy in the droplet has to be solved for each time step. Therefore, the computational complexity leads to a limited applicability to technical problems.

In the TS Model, no energy transport into the droplet interior is considered. The computational cost to simulate the evaporation process is minimal. In the case of UT Model, the total energy balance for the droplet allows the calculation of the temperature variation dT_l:

$$\dot{q} = m_l c_{p,l} \frac{dT_l}{dt}, \tag{3.47}$$

where m_l denotes the droplet mass, T_l denotes the temperature of liquid and $c_{p,l}$ is the liquid heat capacity. The CL Model is more complex. A partial differential equation

for the radial energy transport has to be solved such that T_l can be computed as a function of droplet radius and time i.e. $T_l = f(r,t)$. Considering a local time dependent thermal conductivity of the droplet, the energy conservation equation can be formulated as follows [84]:

$$\frac{\partial T_l}{\partial t} = \alpha_l \left(\frac{\partial^2 T_l}{\partial r^2} + \left(\frac{2}{r} + \frac{1}{\lambda_l} \frac{\partial \lambda_l}{\partial r} \right) \frac{\partial T_l}{\partial r} \right). \tag{3.48}$$

The equation (3.48) can be simplified when a constant heat conductivity in the droplet is assumed:

$$\frac{\partial T_l}{\partial t} = \frac{\alpha_l}{r^2} \frac{\partial}{\partial r} \left(r^2 \frac{\partial T_l}{\partial r} \right). \tag{3.49}$$

Here $\alpha_l = \frac{\lambda_l}{(\rho_l c_{p,l})}$ is the thermal diffusivity and λ_l is the thermal heat conductivity, which depends on the pressure and initial temperature of the droplet and it is taken as a constant. In order to solve the energy equation, the temperature profile at initial time $t = 0$ as well as two boundary conditions must be specified:

$$T_l(t=0) = T_{l,0} \tag{3.50}$$

$$\left. \frac{\partial T_l}{\partial r} \right|_{r=0} = 0 \tag{3.51}$$

$$\left. \frac{\partial T_l}{\partial r} \right|_{r=R} = \frac{\dot{q}}{4\pi R^2 \lambda_{l,s}}. \tag{3.52}$$

While the TS Model underestimates the life time of a droplet, the UT Model estimates the life time of a droplet more accurately. However, as expected among the three models, the CL Model supplies the best results. The life time determined with this model is between the life times calculated with the TS Model and the UT Model. This is shown in [84, 90] for a freely falling hepthane droplet evaporating in nitrogen.

3.2.3 Droplet Motion

The droplet motion is calculated by solving the momentum equation in x- and y-direction. The momentum equation for a droplet [87] is given by:

$$\frac{d\mathbf{v}_l}{dt} = \frac{3}{8} \frac{\rho}{R\rho_l} (\mathbf{v} - \mathbf{v_l}) \mid \mathbf{v} - \mathbf{v_l} \mid C_D + \mathbf{g} \tag{3.53}$$

where $\vec{v}$ and $\vec{v}_l$ are the velocity vectors for the gas and liquid phase, C_D is the drag coefficient. The change in the droplet momentum, given by the left hand side of the equation (3.53), is equal to the sum of all acting forces, namely forces of inertia and the gravitation. Stokes Law [79] supplies the drag coefficient C_D for a sphere:

$$C_D = \frac{24}{\mathrm{Re}}. \tag{3.54}$$

If the sphere is surrounded by gas, the drag coefficient is corrected as follows [91]:

$$C_D = \frac{24}{\mathrm{Re}} \left(1 + \frac{\mathrm{Re}^{2/3}}{6} \right). \tag{3.55}$$

The equation (3.55) is valid when the droplet Reynolds number is Re$<$ 1000.

3.3 Chemical Reactions

3.3.1 Chemical Rate Law

One of the first steps in studying the kinetics of a chemical reaction is to determine the rate law of the reaction. Gas-phase reactions have a large impact on ignition and flame stabilization, on the heat release rate, and on pollutant emissions. The gas-phase chemistry is particularly important for the emission of carbon monoxide, unburned hydrocarbons, aromatic compounds, soot and nitrogen oxides. Reactions that take place in the gas phase are known as homogeneous reactions.

Chemical processes are composed by a number of reversible (or irreversible) reactions that include N chemical species. Each one of these reactions can be represented in the general form [1]

$$\sum_{i=1}^{N} \nu_i' A_i \rightarrow \sum_{i=1}^{N} \nu_i'' A_i \,, \tag{3.56}$$

where ν_i' and ν_i'' are the stoichiometric coefficients of the chemical species i and A_i are the species symbols, and N is the number of chemical species.

For a given reaction, the rate law is an equation which describes how fast a reaction proceeds and how the reaction rate depends on the concentration of the chemical species involved. The rate law describes the time dependence of a chemical reaction. The rate of a reaction whose stoichiometry is known can be measured in terms of the rate of formation of any product or the rate of consumption of any reactant. Formation is normally indicated as a positive rate, with a positive sign, and consumption as a negative rate, with a negative sign. Since a rate of a reaction often depends upon the concentration or pressure of a reactant, but not a product, rates of reactions are usually written in terms of rates of consumption of reactants. The rate law for Reaction (3.56) can be written as [1]

$$\frac{\mathrm{d}c_i}{\mathrm{d}t} = \nu_i k_\mathrm{f} \prod_{i=1}^{N} c_i^{n_{i,1}} \,, \tag{3.57}$$

where $\nu_i = \nu_i'' - \nu_i'$, c_i is the concentration of species i, k_f is the rate coefficient, and $n_{i,1}$ is the reaction order with respect to species i.

For an elementary mechanism composed of N reactions and K species, the rate of formation (or reaction rate) of species j is given by summation over the rate equations (3.58) of all elementary reactions:

$$\dot{\omega}_j = \sum_{j=1}^{N} \nu_{ij} k_{\mathrm{j}} \prod_{i=1}^{K} \left(\frac{Y_i p \bar{W}}{RTW_i} \right)^{\nu_{ij}} \quad . \tag{3.58}$$

For the reverse of reaction (3.56),

$$\sum_{i=1}^{N} \nu_i'' A_i \rightarrow \sum_{i=1}^{N} \nu_i' A_i \,, \tag{3.59}$$

the rate law can be written as

$$\frac{\mathrm{d}c_i}{\mathrm{d}t} = -\nu_i k_{\mathrm{r}} \prod_{i=1}^{N} c_i^{n_{i,2}} \,, \tag{3.60}$$

where $n_{i,2}$ is the reaction order of the i-th product species. The equilibrium has been reached when the forward and backward reactions have the same microscopic rate,

$$\nu_i k_{\mathrm{f}} \prod_{i=1}^{N} c_i^{n_{i,1}} = \nu_i k_{\mathrm{r}} \prod_{i=1}^{N} c_i^{n_{i,2}} \,, \tag{3.61}$$

which means that no net reaction can be observed on a macroscopic level. The equilibrium constant of the reaction [1] is

$$K_{\mathrm{eq}} = \frac{k_{\mathrm{f}}}{k_{\mathrm{r}}} = \prod_{i=1}^{N} c_i^{\nu_i} \,. \tag{3.62}$$

The equilibrium constant, K_{eq}, represents the ratio of the rate coefficients of the forward and reverse reactions. For an ideal gas, the equilibrium constant is calculated according to [1, 19]

$$K_{\mathrm{eq}} = \frac{k_{\mathrm{f}}}{k_{\mathrm{r}}} = \left(\frac{p^0}{RT} \right)^{\sum_{i=1}^{N} \nu_i} \exp \left[\frac{\Delta_R \bar{S}^0}{R} - \frac{\Delta_R \bar{H}^0}{RT} \right] \,, \tag{3.63}$$

where p^0 is the standard pressure ($p^0 = 0.1\mathrm{MPa}$), $\Delta_R \bar{S}^0$ is the molar entropy of the reaction,

$$\Delta_R \bar{S}^0 = \sum_{i=1}^{N} \nu_i \bar{S}_i^0 \,, \tag{3.64}$$

and $\Delta_R \bar{H}^0$ the standard molar enthalpy of the reaction,

$$\Delta_R \bar{H}^0 = \sum_{i=1}^{N} \nu_i \bar{H}_i^0 \,. \tag{3.65}$$

$\bar{S}_i^0$ and $\bar{H}_i^0$ are, respectively, the standard molar entropies and enthalpies of the species involved in the reaction.

3.3.2 Rate Coefficients

3.3.2.1 Temperature Dependence of Rate Coefficients

It is known that the rate of chemical reactions depends on the temperature. At higher temperatures, the probability that two molecules will collide per unit time is higher. This higher collision rate results from a higher average kinetic energy. The activation energy is the amount of energy required to ensure that a reaction happens. In 1889, Arrhenius analyzed the characteristics of rate coefficients and elaborated the well-known Arrhenius Law.

The relationship between the rate of the reaction and its temperature is determined by the Arrhenius equation [1]

$$k = A \exp\left(-\frac{E_\mathrm{a}}{RT}\right), \tag{3.66}$$

where k is the rate coefficient for the reaction, A is called the pre-exponential factor or frequency factor and is a constant specific to each reaction that depends on the chance the molecules will collide in the correct orientation (depends on the molecularity of the reaction and accounts for the number of collisions between molecules in a reaction system), E_a is the activation energy, R is the gas constant (R has the value of $8.314 \times 10^{-3}\,\mathrm{kJ/\,mole\,K}$), and T is the temperature (in K). A and E_a are determined from experiment or statistical mechanics calculations. It is known that not all molecular collisions will result in reaction, but only those with kinetic energy higher than the energy needed to break the reactant's chemical bonds. This energy barrier is described by the activation energy (see Figure 3.2). Therefore, the proportion of collisions occurring between molecules that have kinetic energy higher than activation energy is given by $\exp\left(-E_\mathrm{a}/RT\right)$; this results from the kinetic theory of gases. An analysis of the enthalpy of the system will give a decent account of the energetics of the reaction mixture. By calculating the amounts of energy required to break all the bonds of the reactant species and products, it is possible to calculate the energy difference between the reactants and the products. This is referred to as ΔH, where Δ means difference (energy used in bond breaking reactions minus energy released in bond making products), and H stands for enthalpy, a measure of energy which is equal to the heat transferred at constant pressure. ΔH is negative for exothermic reactions, and refers to the fact that the energy has been released in the form of heat.

However, limitations of the accuracy of experimental data, and the fact that small differences among rate coefficients could cause considerable changes of reaction rates, motivated the common acceptance of a simplified Arrhenius equation. In the case of using detailed chemistry, the rate coefficient is predicted to have the form [1, 19]

$$k = AT^m \exp\left(-\frac{E_\mathrm{a}}{RT}\right), \tag{3.67}$$

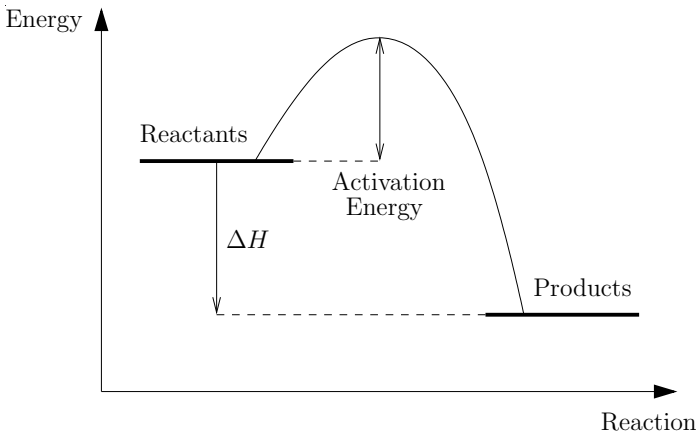

Figure 3.2: The energy profile (schematic) of a chemical reaction. The reaction coordinate represents the changes in bond lengths and bond angles that occur as the chemical reaction proceeds from reactants to products [92].

where A is the preexponential factor, E_a denotes the activation energy. If m is known, E_a can be determined from the slope of the plot of $\ln(k/T^m)$ against $1/T$.

Equations. (3.66) and (3.67) are empirical expressions based on fits of experimental data. Rate coefficients are usually calculated for a finite temperature range.

An important point to notice is that the reaction rate coefficient increases very fast with temperature. This is the fundamental reason why combustion reactions occur at high temperatures and not at room temperature.

3.3.2.2 Pressure Dependence of Rate Coefficients

Lindemann-Hinshelwood-Mechanisms

The pressure dependence of the rate coefficient of unimolecular reactions can be understood using the Lindemann model [93]. This model explains how unimolecular reactions occur and provides a simplified representation of the physical processes that are involved in unimolecular reactions. According to Lindemann, the energy source for a unimolecular reaction is collision with other molecules, M. The excited molecule can deactivate through another collision, or decompose into the products. The Lindemann model for unimolecular reactions of the form

$$\mathrm{A} \underset{k_{-1}}{\overset{k_1}{\rightleftharpoons}} \mathrm{B} \tag{3.68}$$

can be written as

$$\mathrm{A} + \mathrm{M} \underset{k_{-1}}{\overset{k_1}{\rightleftharpoons}} \mathrm{A}^* + \mathrm{M} \tag{3.69}$$

$$\mathrm{A}^* \overset{k_2}{\rightarrow} \mathrm{B} \tag{3.70}$$

where A^* is the energized reactant molecule and M is the collision molecule. The rate of product formation is given by

$$\frac{d[B]}{dt} = k_2[A^*]\,. \tag{3.71}$$

Because of the activation and deactivation of the reactant molecule A^*, the concentration of A^* is very small and the steady-state approximation can be assumed:

$$\frac{d[A^*]}{dt} = 0 = k_1[A][M] - k_{-1}[A^*][M] - k_2[A^*]\,. \tag{3.72}$$

The concentration of species A^* is

$$[A^*] = \frac{k_1[M][A]}{k_2 + k_{-1}[M]}\,, \tag{3.73}$$

and the rate law for the overall reaction is

$$\frac{d[B]}{dt} = -\frac{d[A]}{dt} = \frac{k_1 k_2[M][A]}{k_2 + k_{-1}[M]}\,. \tag{3.74}$$

At very high pressures, the concentration of the collision partner M is high. If the rate of collisional deactivation is much larger than the rate of the unimolecular decomposition, $k_{-1}[A^*][M] \gg k_2[A^*]$ or $k_{-1}[M] \gg k_2$, then

$$\frac{d[B]}{dt} = \frac{k_1 k_2}{k_{-1}}[A] = k_\infty[A]. \tag{3.75}$$

In this case, the reaction rate is first order in A, where the k_∞ represents the high-pressure rate coefficient. The reaction rate does not depend on the concentrations of the collision partners, because at high pressures collisions occur very often and, thus, the rate-limiting step is the decomposition of the activated molecule A^*.

At low pressures, the concentration of the collision partner M is very low. If the rate of collisional deactivation is much smaller than the rate of the reaction, $k_1[M] \ll k_2$, then

$$\frac{d[B]}{dt} = k_1[A][M] = k_0[A][M]\,, \tag{3.76}$$

where k_0 is the low-pressure rate coefficient. In this case, the rate law is first order in [A] and [M]. The overall reaction order is 2. The reaction rate is proportional to the concentration of species A and collision partner M, because the activation is slow at low pressures.

The physical meaning of this change of reaction order is that at low pressures, the bimolecular formation of $[A^*]$ is the rate-limiting reaction. For the overall reaction, the equation of the global rate is

$$\frac{d[B]}{dt} = k[A][M]\,, \tag{3.77}$$

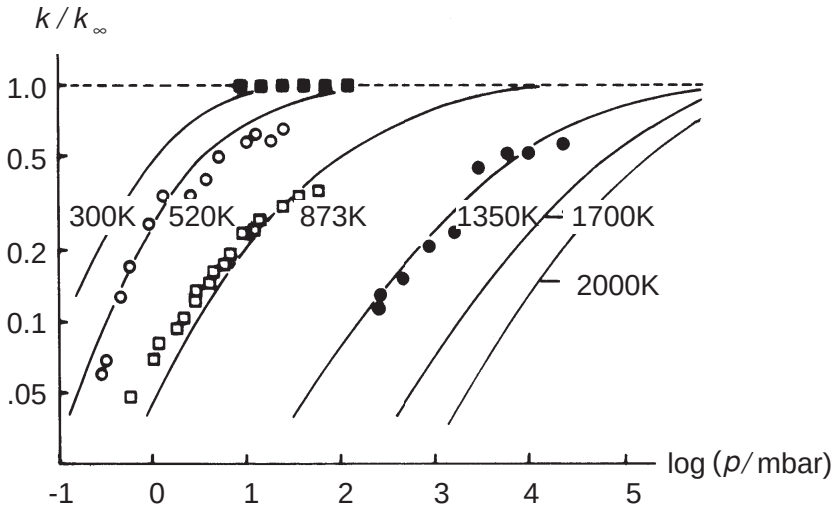

Figure 3.3: Fall-off curves for the unimolecular reaction $C_2H_6 \rightarrow CH_3 + CH_3$ [1]

where

$$k = \frac{k_1 k_2 [\mathrm{A}]}{k_2 + k_{-1}[\mathrm{A}]} \tag{3.78}$$

or

$$\frac{1}{k} = \frac{k_{-1}}{k_1 k_2} + \frac{1}{k_1[\mathrm{A}]}\,. \tag{3.79}$$

The theory can be tested by plotting $1/k$ against $1/[\mathrm{A}]$; the result must be a straight line.

The Lindemann model illustrates the behavior of the reaction rate with concentration but does not explain in detail how the energy transfer processes take place. More accurate results for the pressure dependence of unimolecular reactions can be obtained from the theory of unimolecular reactions . The theory of [94–96] unimolecular reactions yields fall-off curves which describe the pressure dependence of k for different temperatures. The fall-off curves strongly depend on temperature. Thus, the rate coefficients of unimolecular reactions show different temperature dependencies at different values of the pressure.

Rice-Ramsperger-Kassel model (RRK model)

An improved model was proposed in 1926 by O.K. Rice and H.C. Ramsperger and almost simultaneously by L.S. Kassel, and is now known as the Rice-Ramsperger- Kassel model (RRK model) [94]. The model has been elaborated, largely by R.A. Marcus, into the RRKM model.

The essential feature of the model is that, although a molecule might have enough energy to react, that energy is distributed over all the modes of motion of the molecule,

and reaction will occur only when enough of that energy has migrated into a particular location (such as a bond) in the molecule. Provided the rate constant is proportional to this probability:

$$P = \left(1 - \frac{E^*}{E}\right)^{s-1} \tag{3.80}$$

where s is the number of modes of motion over which the energy may be dissipated and E^* is the energy required for the bond of interest to break. We can write the Kassel form of the unimolecular rate constant for the decay of A^* to products as

$$k_2(E) = \left(1 - \frac{E^*}{E}\right)^{s-1} k_2 \quad \text{for } E \geq E^*\,, \tag{3.81}$$

where k_2 is the rate constant used in the original Lindemann theory.

Treatment of Pressure-Dependent Reactions

As mentioned earlier, for some dissociation/recombination and bimolecular reactions, it has been observed that under certain conditions reaction rates depend strongly on pressure as well as on temperature. These reactions are called dissociation/recombination fall-off reactions and chemically activated bimolecular reactions. In the first ones, the rate of the reaction increases with pressure, while for the second type it decreases when the pressure increases. For a given combination and the reverse dissociation reaction,

$$\mathrm{A} + \mathrm{B} + \mathrm{M} \rightleftharpoons \mathrm{AB} + \mathrm{M}, \tag{3.82}$$

the rate law is described by

$$\frac{\mathrm{d[AB]}}{\mathrm{d}t} = k[\mathrm{A}][\mathrm{B}]\,, \tag{3.83}$$

in which the second-order rate constant depending on [M]. The pressure dependence of the rates of these reactions is described by two limiting situations, the low-pressure and high-pressure limits. At low pressures (k_0), a third-body concentration is needed to provide enough energy for the collision so that the reaction may take place. At high pressure (k_∞), this contribution is not necessary. Between these two circumstances, there is an intermediate case, the fall-off region represented by a fall-off expression of k/k_∞ as a function of

$$\frac{k_0[\mathrm{M}]}{k_\infty} = \frac{[\mathrm{M}]}{[\mathrm{M}]_c}\,, \tag{3.84}$$

where $[\mathrm{M}]_c$ is the center of the fall-off curve and indicates the third body concentration for which the extrapolated k_0 would be equal to k/k_∞. The dependence of k on [M] is complicated and has to be analyzed by unimolecular rate theory. For moderately complex molecules at not too high temperatures the following expression is given [97]:

$$k = \frac{k_0 k_\infty[\mathrm{M}]}{k_0[\mathrm{M}] + k_\infty} F = k_0[\mathrm{M}] \left(\frac{1}{1 + [\mathrm{M}]/[\mathrm{M}]_c}\right) F = k_\infty \left(\frac{[\mathrm{M}]/[\mathrm{M}]_c}{1 + [\mathrm{M}]/[\mathrm{M}]_c}\right) F, \tag{3.85}$$

where F is called the broadening factor. At not too high temperatures, which vary from reaction to reaction, the broadening factor can be written as [98]

$$\log F = \frac{\log F_c}{1 + \left[\frac{\log\left([\mathrm{M}]/[\mathrm{M}]_c\right)}{N}\right]^2}, \tag{3.86}$$

where $N = 0.75 - 1.27 \log F_c$. The fall-off curve is characterized by k_0, k_∞, F_c and $[\mathrm{M}]_c$ ($[\mathrm{M}]_c = k_0/k_\infty$).

Troe [99–101] estimated the temperature dependence of F_c by the following equation:

$$F_c = (1-a)\exp\left(-T/T^{***}\right) + a\exp\left(-T/T^{*}\right) + \exp\left(-T^{**}/T\right). \tag{3.87}$$

where a, T^{***}, T^{**} and T^{*} are used to determine the F_c value which describes the center of fall-off range.

											A[cm,mol,s]	n[-]	E_a[kJ/mol]	no.
1. H_2–CO oxidation														
1.1. H_2–O_2 reactions (no HO_2, H_2O_2)														
O_2	+	H			$\rightleftharpoons$	OH	+	O			$2.00{\cdot}10^{14}$	0.0	70.30	1
H_2	+	O			$\rightleftharpoons$	OH	+	H			$5.06{\cdot}10^{04}$	2.67	26.30	2
H_2	+	OH			$\rightleftharpoons$	H_2O	+	H			$1.00{\cdot}10^{8}$	1.60	13.80	3
OH	+	OH			$\rightleftharpoons$	H_2O	+	O			$1.50{\cdot}10^{9}$	1.14	0.42	4
H	+	H	+ M(1)		$\rightleftharpoons$	H_2	+	M(1)			$1.80{\cdot}10^{18}$	−1.0	0.0	5
O	+	O	+ M(1)		$\rightleftharpoons$	O_2	+	M(1)			$2.90{\cdot}10^{17}$	−1.0	0.0	6
H	+	OH	+ M(1)		$\rightleftharpoons$	H_2O	+	M(1)			$2.20{\cdot}10^{22}$	−2.0	0.0	7
1.2. HO_2 formation/consumption														
H	+	O_2	+ M(1)		$\rightleftharpoons$	HO_2	+	M(1)			$2.30{\cdot}10^{18}$	−0.8	0.0	8
HO_2	+	H			$\rightleftharpoons$	OH	+	OH			$1.50{\cdot}10^{14}$	0.0	4.20	9
HO_2	+	H			$\rightleftharpoons$	H_2	+	O_2			$2.50{\cdot}10^{13}$	0.0	2.90	10
HO_2	+	H			$\rightleftharpoons$	H_2O	+	O			$3.00{\cdot}10^{13}$	0.0	7.2	11
HO_2	+	O			$\rightleftharpoons$	OH	+	O_2			$1.80{\cdot}10^{13}$	0.0	−1.70	12
HO_2	+	OH			$\rightleftharpoons$	H_2O	+	O_2			$6.00{\cdot}10^{13}$	0.0	0.0	13
1.3. H_2O_2 formation/consumption														
HO_2	+	HO_2			$\rightleftharpoons$	H_2O_2	+	O_2			$2.50{\cdot}10^{11}$	0.0	−5.20	14
OH	+	OH	+ M(1)		$\rightleftharpoons$	H_2O_2	+	M(1)			$3.25{\cdot}10^{22}$	−2.0	0.0	15
H_2O_2	+	H			$\rightleftharpoons$	H_2	+	HO_2			$1.70{\cdot}10^{12}$	0.0	15.71	16
H_2O_2	+	H			$\rightleftharpoons$	H_2O	+	OH			$1.00{\cdot}10^{13}$	0.0	15.00	17
H_2O_2	+	O			$\rightleftharpoons$	OH	+	HO_2			$2.80{\cdot}10^{13}$	0.0	26.80	18
H_2O_2	+	OH			$\rightleftharpoons$	H_2O	+	HO_2			$5.40{\cdot}10^{12}$	0.0	4.20	20
1.4. CO reactions														
CO	+	O	+ M(1)		$\rightleftharpoons$	CO_2	+	M(1)			$7.10{\cdot}10^{13}$	0.0	−19.00	21
CO	+	OH			$\rightleftharpoons$	CO_2	+	H			$6.00{\cdot}10^{06}$	1.5	−3.10	22
CO	+	HO_2			$\rightleftharpoons$	CO_2	+	OH			$1.50{\cdot}10^{14}$	0.0	98.7	23
CO	+	O_2			$\rightleftharpoons$	CO_2	+	O			$2.50{\cdot}10^{12}$	0.0	200.0	24
2. C_1–hydrocarbons oxidation														
2.1. CH reactions														
CH	+	O			$\rightleftharpoons$	CO	+	H			$4.00{\cdot}10^{13}$	0.0	0.0	25
CH	+	O_2			$\rightleftharpoons$	CHO	+	O			$6.00{\cdot}10^{13}$	0.0	0.0	26
CH	+	CO_2			$\rightleftharpoons$	CHO	+	CO			$3.40{\cdot}10^{12}$	0.0	2.90	27

continues on next page

								A[cm,mol,s]	n[-]	E_a[kJ/mol]	no.
continued from previous page											
CH	+	H_2O	$\rightleftharpoons$	CH_2O	+	H		$3.80 \cdot 10^{12}$	0.0	−3.2	28
CH	+	H_2O	$\rightleftharpoons$	$^3CH_2$	+	OH		$1.90 \cdot 10^{12}$	0.0	−3.2	29
CH	+	OH	$\rightleftharpoons$	CHO	+	H		$3.00 \cdot 10^{13}$	0.0	0.0	30
		2.2. CHO reactions									
CHO	+	M(1)	$\rightleftharpoons$	CO	+	H	+ M(1)	$7.10 \cdot 10^{14}$	0.0	70.30	31
CHO	+	H	$\rightleftharpoons$	CO	+	H_2		$9.00 \cdot 10^{13}$	0.0	0.0	32
CHO	+	O	$\rightleftharpoons$	CO	+	OH		$3.00 \cdot 10^{13}$	0.0	0.0	33
CHO	+	O	$\rightleftharpoons$	CO_2	+	H		$3.00 \cdot 10^{13}$	0.0	0.0	34
CHO	+	OH	$\rightleftharpoons$	CO	+	H_2O		$1.00 \cdot 10^{14}$	0.0	0.0	35
CHO	+	O_2	$\rightleftharpoons$	CO	+	HO_2		$3.00 \cdot 10^{12}$	0.0	0.0	36
CHO	+	CHO	$\rightleftharpoons$	CH_2O	+	CO		$3.00 \cdot 10^{13}$	0.0	0.0	37
		2.3. CH_2 reactions									
$^3CH_2$	+	H	$\rightleftharpoons$	CH	+	H_2		$6.00 \cdot 10^{12}$	0.0	−7.5	38
$^3CH_2$	+	O	$\rightarrow$	CO	+	H	+ H	$8.40 \cdot 10^{12}$	0.0	0.0	39
$^3CH_2$	+	$^3CH_2$	$\rightleftharpoons$	C_2H_2	+	H_2		$1.20 \cdot 10^{13}$	0.0	3.40	40
$^3CH_2$	+	$^3CH_2$	$\rightleftharpoons$	C_2H_2	+	H	+ H	$1.10 \cdot 10^{14}$	0.0	3.40	41
$^3CH_2$	+	CH_3	$\rightleftharpoons$	C_2H_4	+	H		$4.20 \cdot 10^{13}$	0.0	0.0	42
$^3CH_2$	+	O_2	$\rightleftharpoons$	CO	+	OH	+ H	$1.30 \cdot 10^{13}$	0.0	6.2	43
$^3CH_2$	+	O_2	$\rightleftharpoons$	CO_2	+	H_2		$1.20 \cdot 10^{13}$	0.0	6.2	44
$^1CH_2$	+	M(1)	$\rightleftharpoons$	$^3CH_2$	+	M(1)		$1.20 \cdot 10^{13}$	0.0	0.0	45
$^1CH_2$	+	O_2	$\rightleftharpoons$	CO	+	OH	+ H	$3.10 \cdot 10^{13}$	0.0	0.0	46
$^1CH_2$	+	H_2	$\rightleftharpoons$	CH_3	+	H		$7.20 \cdot 10^{13}$	0.0	0.0	47
$^1CH_2$	+	CH_3	$\rightleftharpoons$	C_2H_4	+	H		$1.60 \cdot 10^{13}$	0.0	−2.38	48
		2.4. CH_2O reactions									
CH_2O	+	M(1)	$\rightleftharpoons$	CHO	+	H	+ M(1)	$5.00 \cdot 10^{16}$	0.0	320.00	49
CH_2O	+	H	$\rightleftharpoons$	CHO	+	H_2		$2.30 \cdot 10^{10}$	1.05	13.70	50
CH_2O	+	O	$\rightleftharpoons$	CHO	+	OH		$4.15 \cdot 10^{11}$	0.57	11.56	51
CH_2O	+	OH	$\rightleftharpoons$	CHO	+	H_2O		$3.40 \cdot 10^{09}$	1.2	−1.90	52
CH_2O	+	HO_2	$\rightleftharpoons$	CHO	+	H_2O_2		$3.00 \cdot 10^{12}$	0.0	54.70	53
CH_2O	+	CH_3	$\rightleftharpoons$	CHO	+	CH_4		$1.00 \cdot 10^{11}$	0.0	25.50	54
CH_2O	+	O_2	$\rightleftharpoons$	CHO	+	HO_2		$6.00 \cdot 10^{13}$	0.0	171.00	55
		2.5. CH_3 reactions									
CH_3	+	M(1)	$\rightleftharpoons$	$^3CH_2$	+	H	+ M(1)	$6.90 \cdot 10^{14}$	0.0	345.0	56
CH_3	+	M(1)	$\rightleftharpoons$	$^3CH_2$	+	H	+ M(1)	$1.00 \cdot 10^{16}$	0.0	379.0	57
CH_3	+	O	$\rightleftharpoons$	CH_2O	+	H		$8.43 \cdot 10^{13}$	0.0	0.0	58
CH_3	+	H	$\rightleftharpoons$	CH_4				$1.93 \cdot 10^{36}$	−7.0	38.0	59
CH_3	+	OH	$\rightarrow$	CH_3O	+	H		$2.26 \cdot 10^{14}$	0.0	64.8	60

continues on next page

	A[cm,mol,s]	n[-]	E_a[kJ/mol]	no.
continued from previous page				
$CH_3O + H \rightarrow CH_3 + OH$	$4.75{\cdot}10^{16}$	-0.13	88.00	61
$CH_3 + O_2 \rightarrow OH + CH_2O$	$3.30{\cdot}10^{11}$	0.0	37.4	62
$CH_3 + HO_2 \rightleftharpoons CH_3O + OH$	$1.80{\cdot}10^{13}$	0.0	0.0	63
$CH_3 + HO_2 \rightleftharpoons CH_4 + O_2$	$3.60{\cdot}10^{12}$	0.0	0.0	64
$CH_3 + CH_3 \rightarrow C_2H_4 + O_2$	$1.00{\cdot}10^{16}$	0.0	134.0	65
$CH_3 + CH_3 + \rightleftharpoons C_2H_6 +$	$1.69{\cdot}10^{53}$	-12.0	81.2	66
2.6. CH_3O reactions				
$CH_3O + M(1) \rightleftharpoons CH_2O + H + M(1)$	$5.00{\cdot}10^{13}$	0.0	105.00	67
$CH_3O + H \rightleftharpoons CH_2O + H_2$	$1.80{\cdot}10^{13}$	0.0	0.0	68
$CH_3O + O_2 \rightleftharpoons CH_2O + HO_2$	$4.00{\cdot}10^{10}$	0.0	8.9	69
$CH_3O + CH_2O \rightarrow CH_3OH + CHO$	$6.00{\cdot}10^{11}$	0.0	13.8	70
$CH_3OH + CHO \rightarrow CH_3O + CH_2O$	$6.50{\cdot}10^{09}$	0.0	57.2	71
$CH_3O + O \rightleftharpoons O_2 + CH_3$	$1.10{\cdot}10^{13}$	0.0	0.0	72
$CH_3O + O \rightleftharpoons OH + CH_2O$	$1.40{\cdot}10^{12}$	0.0	0.0	73
2.7. CH_2OH reactions				
$CH_2OH + M(1) \rightleftharpoons CH_2O + H + M(1)$	$5.00{\cdot}10^{13}$	0.0	105.00	74
$CH_2OH + H \rightleftharpoons CH_2O + H_2$	$3.00{\cdot}10^{13}$	0.0	0.0	75
$CH_2OH + O_2 \rightleftharpoons CH_2O + HO_2$	$1.00{\cdot}10^{13}$	0.0	30.0	76
2.8. CH_3O_2 reactions				
$CH_3O_2 + M(1) \rightarrow CH_3 + O_2 + M(1)$	$7.24{\cdot}10^{16}$	0.0	111.00	77
$CH_3 + O_2 + M(1) \rightarrow CH_3O_2 + M(1)$	$1.41{\cdot}10^{16}$	0.0	-4.60	78
$CH_3O_2 + CH_2O \rightarrow CH_3O_2H + CHO$	$1.30{\cdot}10^{11}$	0.0	37.7	79
$CH_3O_2H + CHO \rightarrow CH_3O_2 + CH_2O$	$2.50{\cdot}10^{10}$	0.0	42.3	80
$CH_3O_2 + CH_3 \rightarrow CH_3O + CH_3O$	$3.80{\cdot}10^{12}$	0.0	-5.0	81
$CH_3O + CH_3O \rightarrow CH_3O_2 + CH_3$	$2.00{\cdot}10^{10}$	0.0	0.0	82
$CH_3O_2 + HO_2 \rightarrow CH_3O_2H + O_2$	$4.60{\cdot}10^{10}$	0.0	-10.9	83
$CH_3O_2H + O_2 \rightarrow CH_3O_2 + HO_2$	$3.00{\cdot}10^{12}$	0.0	163.0	84
$CH_3O_2 + CH_3O_2 \rightarrow CH_2O + CH_3OH + O_2$	$1.80{\cdot}10^{12}$	0.0	0.0	85
$CH_3O_2 + CH_3O_2 \rightarrow CH_3O + CH_3O + O_2$	$3.70{\cdot}10^{12}$	0.0	9.20	86
2.9. CH_4 reactions				
$CH_4 + H \rightleftharpoons H_2 + CH_3$	$1.30{\cdot}10^{4}$	3.0	33.6	87
$CH_4 + O \rightleftharpoons OH + CH_3$	$6.92{\cdot}10^{8}$	1.56	35.5	88
$CH_4 + OH \rightleftharpoons H_2O + CH_3$	$1.60{\cdot}10^{7}$	1.83	11.6	89
$CH_4 + HO_2 \rightleftharpoons H_2O_2 + CH_3$	$1.10{\cdot}10^{13}$	0.0	103.00	90
$CH_4 + CH \rightleftharpoons C_2H_4 + H$	$3.00{\cdot}10^{13}$	0.0	-1.7	91
$CH_4 + {}^3CH_2 \rightleftharpoons CH_3 + CH_3$	$1.30{\cdot}10^{13}$	0.0	39.9	92

continues on next page

							A[cm,mol,s]	n[-]	E_a[kJ/mol]	no.
continued from previous page										
2.10. CH_3OH reactions										
CH_3OH			$\rightleftharpoons$	CH_3	+	OH	$9.51{\cdot}10^{29}$	-4.3	404.0	93
CH_3OH	+	H	$\rightleftharpoons$	CH_2OH	+	H_2	$4.00{\cdot}10^{13}$	0.0	25.5	94
CH_3OH	+	O	$\rightleftharpoons$	CH_2OH	+	OH	$1.00{\cdot}10^{13}$	0.0	19.6	95
CH_3OH	+	OH	$\rightleftharpoons$	CH_2OH	+	H_2O	$1.00{\cdot}10^{13}$	0.0	7.1	96
CH_3OH	+	HO_2	$\rightarrow$	CH_2OH	+	H_2O_2	$6.20{\cdot}10^{12}$	0.0	81.1	97
CH_2OH	+	H_2O_2	$\rightarrow$	CH_3OH	+	HO_2	$1.00{\cdot}10^{7}$	1.7	47.9	98
CH_3OH	+	CH_3	$\rightleftharpoons$	CH_4	+	CH_2OH	$9.00{\cdot}10^{12}$	0.0	41.1	99
CH_3OH	+	CH_3O	$\rightarrow$	CH_2OH	+	CH_3OH	$2.00{\cdot}10^{11}$	0.0	29.3	100
CH_2OH	+	CH_3OH	$\rightarrow$	CH_3OH	+	CH_3O	$2.20{\cdot}10^{4}$	1.7	45.4	101
CH_3OH	+	CH_2O	$\rightarrow$	CH_3O	+	CH_3O	$1.53{\cdot}10^{12}$	0.0	333.0	102
CH_3O	+	CH_3O	$\rightarrow$	CH_3OH	+	CH_2O	$3.00{\cdot}10^{13}$	0.0	0.0	103
2.11. CH_3O_2H reactions										
CH_3O_2H			$\rightleftharpoons$	CH_3O	+	OH	$4.00{\cdot}10^{15}$	0.0	180.0	104
CH_3O_2H	+	OH	$\rightleftharpoons$	H_2O	+	CH_3O_2	$2.60{\cdot}10^{12}$	0.0	0.0	105
3. C_2–hydrocarbons oxidation										
3.1. C_2H reactions										
C_2H	+	O	$\rightleftharpoons$	CO	+	CH	$1.00{\cdot}10^{13}$	0.0	0.0	106
C_2H	+	O_2	$\rightleftharpoons$	$HCCO$	+	O	$3.00{\cdot}10^{12}$	0.0	0.0	107
3.2. HCCO reactions										
$HCCO$	+	H	$\rightleftharpoons$	$^3CH_2$	+	CO	$1.50{\cdot}10^{14}$	0.0	0.0	108
$HCCO$	+	O	$\rightarrow$	CO	+	CO + H	$9.60{\cdot}10^{13}$	0.0	0.0	109
$HCCO$	+	$^3CH_2$	$\rightleftharpoons$	C_2H_3	+	CO	$3.00{\cdot}10^{13}$	0.0	0.0	110
3.3. C_2H_2 reactions										
C_2H_2	+	M(1)	$\rightleftharpoons$	C_2H	+	H + M(1)	$3.60{\cdot}10^{16}$	0.0	446.0	111
C_2H_2	+	O_2	$\rightleftharpoons$	$HCCO$	+	OH	$2.00{\cdot}10^{8}$	1.5	126.0	112
C_2H_2	+	H	$\rightleftharpoons$	C_2H	+	H_2	$6.02{\cdot}10^{13}$	0.0	116.0	113
C_2H_2	+	O	$\rightleftharpoons$	$^3CH_2$	+	CO	$1.72{\cdot}10^{4}$	2.8	2.1	114
C_2H_2	+	O	$\rightleftharpoons$	$HCCO$	+	H	$1.72{\cdot}10^{4}$	2.8	2.1	115
C_2H_2	+	OH	$\rightleftharpoons$	H_2O	+	C_2H	$6.00{\cdot}10^{13}$	0.0	54.2	116
C_2H_2	+	C_2H	$\rightleftharpoons$	C_4H_2	+	H	$3.00{\cdot}10^{13}$	0.0	0.0	117

continues on next page

		A[cm,mol,s]	n[-]	E_a[kJ/mol]	no.

continued from previous page

3.4. CH_2CO reactions

CH_2CO	+ M(1)	$\rightleftharpoons$	$^3CH_2$	+ CO	+ M(1)	$1.00 \cdot 10^{16}$	0.0	248.0	118
CH_2CO	+ H	$\rightleftharpoons$	CH_3	+ CO		$3.60 \cdot 10^{13}$	0.0	14.1	119
CH_2CO	+ O	$\rightleftharpoons$	CHO	+ CHO		$2.30 \cdot 10^{12}$	0.0	5.7	120
CH_2CO	+ OH	$\rightleftharpoons$	CH_2O	+ CHO		$1.00 \cdot 10^{13}$	0.0	0.0	121

3.5. C_2H_3 reactions

C_2H_3		$\rightleftharpoons$	C_2H_2	+ H		$4.73 \cdot 10^{40}$	−8.8	194.0	122
C_2H_3	+ OH	$\rightleftharpoons$	C_2H_2	+ H_2O		$5.00 \cdot 10^{13}$	0.0	0.0	123
C_2H_3	+ H	$\rightleftharpoons$	C_2H_2	+ H_2		$1.20 \cdot 10^{13}$	0.0	0.0	124
C_2H_3	+ O	$\rightleftharpoons$	C_2H_2	+ OH		$1.00 \cdot 10^{13}$	0.0	0.0	125
C_2H_3	+ O	$\rightleftharpoons$	CH_3	+ CO		$1.00 \cdot 10^{13}$	0.0	0.0	126
C_2H_3	+ O	$\rightleftharpoons$	CHO	+ $^3CH_2$		$1.00 \cdot 10^{13}$	0.0	0.0	127
C_2H_3	+ O_2	$\rightleftharpoons$	CH_2O	+ CHO		$5.40 \cdot 10^{12}$	0.0	0.0	128

3.6. CH_3CO reactions

CH_3CO		$\rightleftharpoons$	CH_3	+ CO		$2.32 \cdot 10^{26}$	−5.0	75.1	129
CH_3CO	+ H	$\rightleftharpoons$	CH_2CO	+ H_2		$2.00 \cdot 10^{13}$	0.0	0.0	130

3.7. CH_2CHO reactions

CH_2CHO	+ H	$\rightleftharpoons$	CH_2CO	+ H_2		$2.00 \cdot 10^{13}$	0.0	0.0	131

3.8. C_2H_4 reactions

C_2H_4	+ M(1)	$\rightleftharpoons$	C_2H_2	+ H_2	+ M(1)	$7.50 \cdot 10^{17}$	0.0	320.0	132
C_2H_4	+ M(1)	$\rightleftharpoons$	C_2H_3	+ H	+ M(1)	$8.50 \cdot 10^{17}$	0.0	404.0	133
C_2H_4	+ H	$\rightleftharpoons$	C_2H_3	+ H_2		$5.67 \cdot 10^{14}$	0.0	62.9	134
C_2H_4	+ O	$\rightleftharpoons$	CH_2CHO	+ H		$1.40 \cdot 10^{6}$	2.08	0.0	135
C_2H_4	+ O	$\rightleftharpoons$	CHO	+ CH_3		$2.42 \cdot 10^{6}$	2.08	0.0	136
C_2H_4	+ OH	$\rightleftharpoons$	C_2H_3	+ H_2O		$2.11 \cdot 10^{13}$	0.0	24.9	137

3.9. CH_3CHO reactions

CH_3CHO	+ M(1)	$\rightleftharpoons$	CH_3	+ CHO	+ M(1)	$7.00 \cdot 10^{15}$	0.0	343.0	138
CH_3CHO	+ H	$\rightleftharpoons$	CH_3CO	+ H_2		$2.10 \cdot 10^{9}$	1.16	10.1	139
CH_3CHO	+ H	$\rightleftharpoons$	CH_2CHO	+ H_2		$2.00 \cdot 10^{9}$	1.16	10.1	140
CH_3CHO	+ O	$\rightleftharpoons$	CH_3CO	+ OH		$5.00 \cdot 10^{12}$	0.0	7.6	141
CH_3CHO	+ O	$\rightleftharpoons$	CH_2CHO	+ OH		$8.00 \cdot 10^{11}$	0.0	7.6	142
CH_3CHO	+ O_2	$\rightleftharpoons$	CH_3CO	+ HO_2		$4.00 \cdot 10^{13}$	0.0	164.0	143
CH_3CHO	+ OH	$\rightleftharpoons$	CH_3CO	+ H_2O		$2.30 \cdot 10^{10}$	0.73	−4.7	144
CH_3CHO	+ HO_2	$\rightleftharpoons$	CH_3CO	+ H_2O_2		$3.00 \cdot 10^{12}$	0.0	50.0	145

					A[cm,mol,s]	n[-]	E_a[kJ/mol]	no.
CH_3CHO	+ $^3CH_2$	$\rightleftharpoons$	CH_3CO	+ CH_3	$2.50{\cdot}10^{12}$	0.0	15.9	146
CH_3CHO	+ CH_3	$\rightleftharpoons$	CH_3CO	+ CH_4	$2.00{\cdot}10^{-6}$	5.64	10.3	147
	3.10. C_2H_5 reactions							
C_2H_5	+ M(1)	$\rightleftharpoons$	C_2H_4	+ H + M(1)	$1.02{\cdot}10^{43}$	−9.1	224.0	148
C_2H_5	+ H	$\rightleftharpoons$	CH_3	+ CH_3	$3.00{\cdot}10^{13}$	0.0	0.0	149
C_2H_5	+ O	$\rightleftharpoons$	CH_3CHO	+ H	$5.00{\cdot}10^{13}$	0.0	0.0	150
C_2H_5	+ O	$\rightleftharpoons$	CH_2O	+ CH_3	$1.00{\cdot}10^{13}$	0.0	0.0	151
C_2H_5	+ O_2	$\rightleftharpoons$	C_2H_4	+ HO_2	$1.10{\cdot}10^{10}$	0.0	−6.3	152
C_2H_5	+ CH_3	$\rightleftharpoons$	C_2H_4	+ CH_4	$1.14{\cdot}10^{12}$	0.0	0.0	153
C_2H_5	+ C_2H_5	$\rightleftharpoons$	C_2H_4	+ C_2H_6	$1.40{\cdot}10^{12}$	0.0	0.0	154
	3.11. C_2H_6 reactions							
C_2H_6	+ H	$\rightleftharpoons$	C_2H_5	+ H_2	$1.40{\cdot}10^{9}$	1.5	31.1	155
C_2H_6	+ O	$\rightleftharpoons$	C_2H_5	+ OH	$1.00{\cdot}10^{9}$	1.5	24.4	156
C_2H_6	+ OH	$\rightleftharpoons$	C_2H_5	+ H_2O	$7.20{\cdot}10^{6}$	2.0	3.6	157
C_2H_6	+ HO_2	$\rightleftharpoons$	C_2H_5	+ H_2O_2	$1.70{\cdot}10^{13}$	0.0	85.9	158
C_2H_6	+ O_2	$\rightleftharpoons$	C_2H_5	+ HO_2	$6.00{\cdot}10^{13}$	0.0	217.0	159
C_2H_6	+ $^3CH_2$	$\rightleftharpoons$	C_2H_5	+ CH_3	$2.20{\cdot}10^{13}$	0.0	36.3	160
C_2H_6	+ CH_3	$\rightleftharpoons$	C_2H_5	+ CH_4	$1.50{\cdot}10^{-7}$	6.0	25.4	161

Table 3.1.: Small hydrocarbons mechanism [1].

Figure 3.4 is a scheme of the oxidation of methane mechanism and Table 3.1 is the detailed mechanism of the oxidation of methane in the gas phase [1]. It is composed of 294 elementary reactions and involves 35 species.

3.4 Transport Properties

3.4.1 Gas Phase Properties

The transport properties of the gas phase have been evaluated from the kinetic theory of gases [75].

Specific Heat and Specific Enthalpy

The specific heat, $c_{p,i}$, of species i, in gas phase is calculated from a temperature dependent polynomial fit [102]

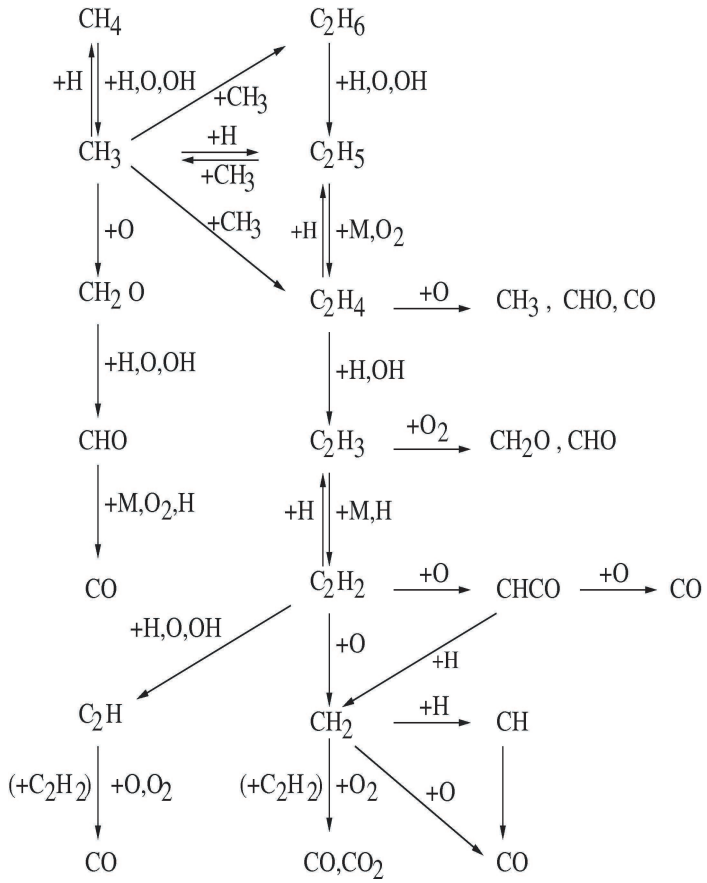

Figure 3.4: Mechanism of the oxidation of CH_4 [1].

$$c_{p,i} = R \sum_{n=1}^{5} a_{c_P,i,n} T^{n-1}, \tag{3.88}$$

where the coefficients $a_{c_P,i,n}$ for two ranges of temperatures, between 300 to 1000 K, and between 1000 to 4000 K are given. The specific heat of the gas mixture, $\bar{c}_p$, is then determined from the specific heats of its constituent species as below

$$\bar{c}_p = \sum_{i=1}^{K} c_{p,i} Y_i. \tag{3.89}$$

The specific enthalpy, h_i of species i, which is temperature dependent, and calculated by integrating the specific heat of species i, as follows

$$h_i(T) = h^0_{i,T^0} + \int_{T^0}^{T} c_P(T) dT, \tag{3.90}$$

where h^0_{i,T^0} is the standard enthalpy of formation of species i, at reference temperature T^0.

Dynamic Viscosity

The dynamic viscosity μ_i, of species, i, in the gas phase is calculated [102] as follows

$$\ln(\mu_i) = \sum_{i=1}^{4} a_{\mu,i,n} (\ln T)^{n-1} \tag{3.91}$$

and the viscosity of the gas mixture, $\bar{\mu}$, is evaluated from the viscosities of the constituent species by

$$\bar{\mu} = \frac{1}{2} \left[\sum_{i=1}^{K} X_i \mu_i + \left(\sum_{i=1}^{K} \frac{X_i}{\mu_i} \right)^{-1} \right]. \tag{3.92}$$

Thermal Conductivity

The thermal conductivity λ_i, of species i, in the gas phase is calculated [102] as follows

$$\ln(\lambda_i) = \sum_{i=1}^{4} a_{\lambda,i,n} (\ln T)^{n-1} \tag{3.93}$$

and the thermal conductivity of the gas mixture, $\bar{\lambda}$, is evaluated from the thermal conductivities of the constituent species as

$$\bar{\lambda} = \frac{1}{2} \left[\sum_{i=1}^{K} X_i \lambda_i + \left(\sum_{i=1}^{K} \frac{X_i}{\lambda_i} \right)^{-1} \right]. \tag{3.94}$$

Diffusion Coefficients

Binary diffusion coefficient D_{ij}, of species i into species j, is calculated [102] as follows

$$\ln(pD_{i,j}) = \sum_{i=1}^{4} a_{D,i,n} (\ln T)^{n-1}. \tag{3.95}$$

The coefficients $a_{D,i,n}$, $a_{\lambda,i,n}$,$a_{\mu,i,n}$ are valid for temperatures between 300 and 5000K. The diffusion coefficient of species, i, into the gas mixture D_i, is calculated from the binary diffusion coefficients [102] as follows

$$D_i = \frac{1 - Y_i}{\sum_{j \neq i}^{K} \frac{X_i}{D_{ij}}}. \tag{3.96}$$

The transport coefficients for the species CH_4 and O_2, which are the only available components in temperatures ranging below 300 K, increasingly deviate from the extrapolated NASA polynomials when reaching the critical temperatures ($T_{c,O_2} = 154.6$ K, $T_{c,CH_4} = 190.55$ K). Moreover, they show a strong pressure dependence. Therefore the transport characteristics for CH_4 and O_2 are taken from JSME tables [103], which cover the temperature range from 80 to 300 K and the pressure range from 0.1 to 20 MPa. The figures (3.5, 3.6, 3.7, 3.8) show the pressure and temperature dependence of the specific heat conductivity and the dynamic viscosity of CH_4 and O_2. Figure 3.9 shows the dependence of latent heat of vaporization of oxygen below 300 K as a function of temperature and pressure.

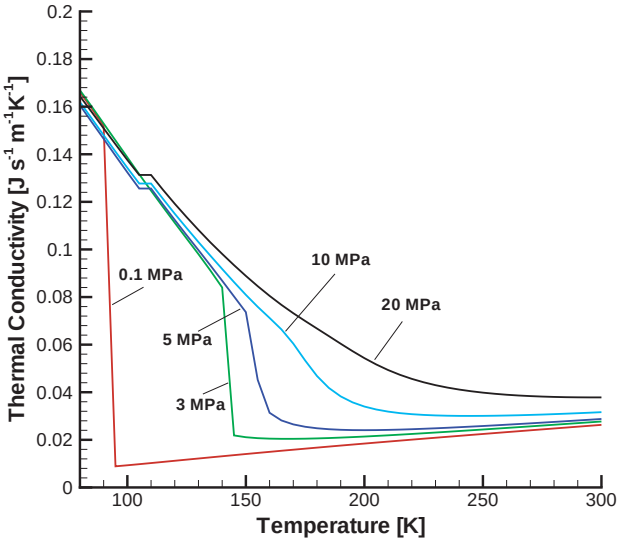

Figure 3.5: The pressure and temperature dependence of the thermal conductivity of methane in the temperature range $100 < T < 300$ K, [103].

The thermodynamic data for CH_4, for temperature range between 300 and 3000 K is computed with NASA polynomials. Below 300 K, the data is taken from JSME tables [103] for the pressures between 0.1 and 20 MPa and temperatures between 100 and 300 K. For more detailed information needed for computations, the thermodynamic data are linearly interpolated in the present work.

3.4.2 Liquid Phase Properties

Previous studies have shown that the liquid phase is dominant in characterizing both laminar and turbulent flames [105, 106]. Since CH_4/LOx -spray flames are considered in this work, the thermodynamic data of liquid oxygen are crucial. These data are taken

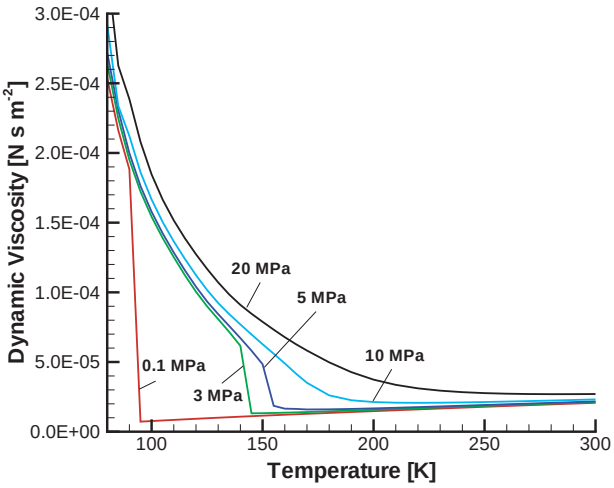

Figure 3.6: The pressure and temperature dependence of the dynamic viscosity of methane in the temperature range $100 < T < 300$ K, [103].

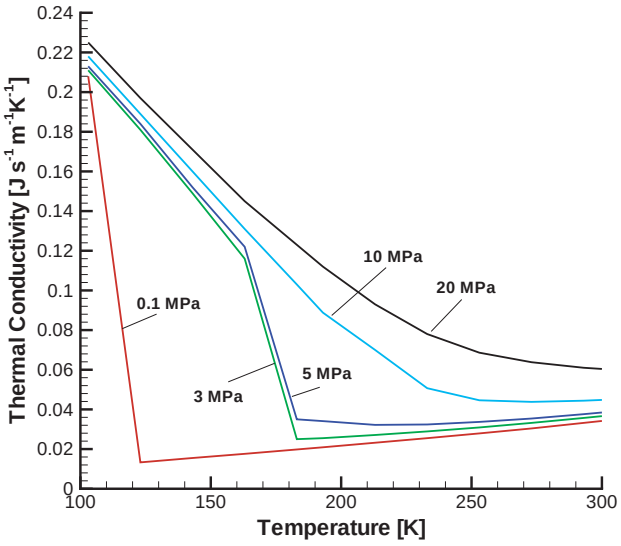

Figure 3.7: The pressure and temperature dependence of the thermal conductivity of oxygen in the temperature range $80 < T < 300$ K, [103].

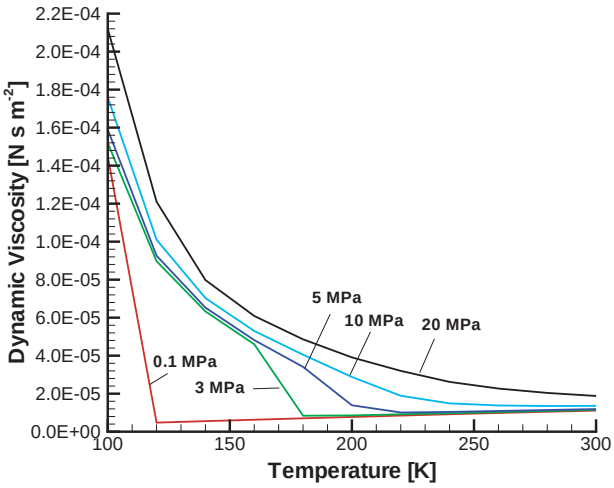

Figure 3.8: The pressure and temperature dependence of the dynamic viscosity of oxygen in the temperature range $80 < T < 300$ K, Data taken from [103].

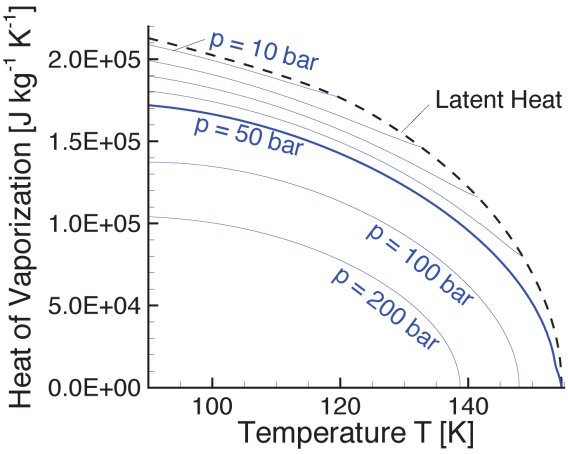

Figure 3.9: The pressure and temperature dependence of the latent heat of vaporization of oxygen in the temperatures $T < 300$ K, [104].

from the JSME tables [103] for pressures between 0.1 to 20 MPa and temperatures between 80 K and the boiling temperature. The tabulated values are linearly interpolated in the code.

A single component spray is considered in this work. Therefore no mixture rules for the liquid phase have to be considered.

4 Mathematical Models of Droplet Vaporization and Spray Combustion

4.1 Single Droplet Vaporization

4.1.1 Description of the Droplet Vaporization

While the vaporization of cold droplets in hot air has been frequently studied, the inverse case is not yet well investigated because of the increased experimental complexity. Radiation of a pulsed CO_2 laser is used to provide controlled internal heating of fiber-suspended individual water droplets in order to observe the droplet vaporization via direct visualization. The laser heating and the vaporization are simulated with a convective droplet vaporization model, which is modified to account for the laser heating. For understanding these processes, a short description of the experimental setup of [28] is presented.

Experimental Setup

Figure 4.1 shows the experimental setup [28] that is considered in the present work [29]. A single water droplet of 1.2 µl in volume is suspended on two thin glass fibers ($dh = dv$ = 140 µm) in the focal plane of a high-resolution CCD camera (LaVision Flowmaster). The pulsed beam of a CO_2-laser operating at a repetition rate of 2 Hz and with a wavelength of λ= 9.3 µm is focused on the droplet by a f = 700 mm spherical ZnSe lens to an overall intensity of 600 W/cm^2. Different heating rates are achieved by variation of the laser pulse duration (2 - 15 ms). A stroboscopic light source is placed behind the droplet, and shadow images (see Figure 4.2) of the droplet during the vaporization process are recorded by a high-resolution CCD camera at a repetition rate of 2 Hz. The nominal spatial resolution of the images is 3.3 µm per pixel.

The absorption-coefficient α of water at the laser wavelength [107] is 572 cm^{-1}, which results according to Beer's law, cf. Eq. (4.1), in absorption of more than 80% of the incident infrared light entering the droplet in a 30 µm layer at the droplet surface:

$$I(x) = I_0 e^{-\alpha x}. \tag{4.1}$$

Therefore, we can assume that the laser beam entering the droplet is completely absorbed over the whole observation time range. The droplet shape is determined according to the Laplace-Young [107] from Eq. (4.2):

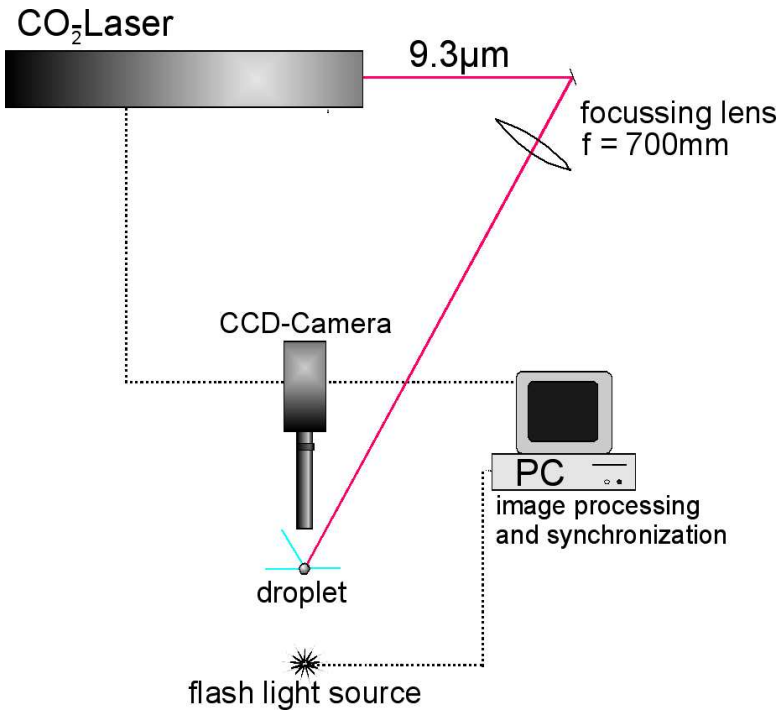

Figure 4.1: Experimental setup [29].

$$\Delta P = P_{in} - P_{\infty} = \sigma \left(\frac{1}{r_1} + \frac{1}{r_2} \right). \tag{4.2}$$

P_{in} and P_{∞} are the internal and external pressure, respectively, σ is the surface tension, and r_1 and r_2 are the radii of curvature at each point of the droplet surface.

A simple experimental method is used to suspend the droplet on a thin glass fiber for the time of the measurement. Different fiber arrangements are possible. In our studies, a two fibers arrangement was used (see Figure 4.2): A vertical fiber to set the initial position of the droplet and a horizontal fiber to additionally fix it and prevent "creeping" of the droplet due to change in the equilibrium between adhesion and gravitational forces during the vaporization process. This method is only applicable for relatively large droplets (500 µm - 1 mm) and due to the fibers, the droplet shape is distorted as can be seen in Figure 4.2. Liquids with a low specific surface tension show a stronger deviation from the spherical shape. The degree of the deviation of the droplets spherical shape depends on the distance between the fibers as well as the droplet volume itself. In order to correct these effects, the system is first calibrated by imaging of droplets with known volumes. Figure 4.3 schematically shows how the droplet cross-section is reconstructed from the shadow image in combination with the background image. An

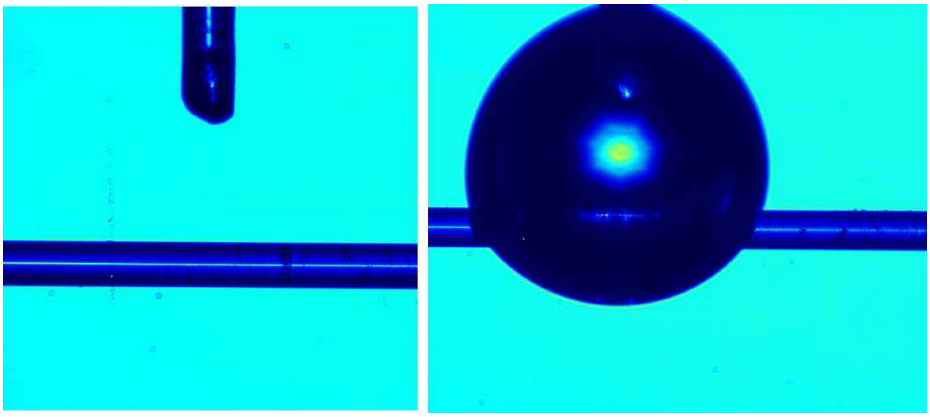

Figure 4.2: Left: Arrangement of the suspending fibers. Right: Shadow image of a suspended water droplet. The combination of fibers is necessary to hold the droplet in place during vaporization [29, 42].

image processing routine calculates the droplet volume and radius from the cross section and the distance d_{x1}. The accuracy of the measurement is found to be 3% for the large droplets and up to 8% for small droplets [28, 29].

The presence of the fibers prohibits the observation of the evaporating droplet throughout its whole lifetime. It was found that in the volume range of interest (0.5-1.3 µl) the x-diameter $d_{x,1}$ of the distorted droplet was proportional to the diameter d_s of a perfect sphere of the same volume:

$$\begin{aligned} d_{x,i} = c_d d_s &\longleftrightarrow V_{droplet} \\ &= \frac{1}{6}\pi(c_d^{-1} d_{x,i})^3. \end{aligned} \tag{4.3}$$

For a given liquid, i.e. water, the calibration factor c_d depends only on the fiber geometry and it was close to unity in all experiments. The observed droplet cross section A_i correlated well with the expected cross section of a spherical droplet, A_s, according to

$$\begin{aligned} A_i = C_A A_s &\longleftrightarrow V_{droplet} \\ &= \frac{1}{6}\pi(\sqrt{C_A \pi^{-1} A_i})^3, \end{aligned} \tag{4.4}$$

where C_A is the calibration constant that depends on the fiber arrangement only. When the droplet diameter drops below 0.5 mm, the error in the measurements exceeds 10%. When the droplet diameter reaches the size of the distance between the supporting fibers ($d \approx 0.3$ mm) the measurement has to be stopped in order to prevent the fibers to be destroyed by the laser beam. As it can already be seen in the Figure 4.2 that the disadvantages of this method lie in the distortion of the droplet shape and the consequent limitation to liquids with a high surface tension. A further inconvenience is the large initial droplet size ($\sim$ 1 mm in this case), which causes a higher distortion of the droplet.

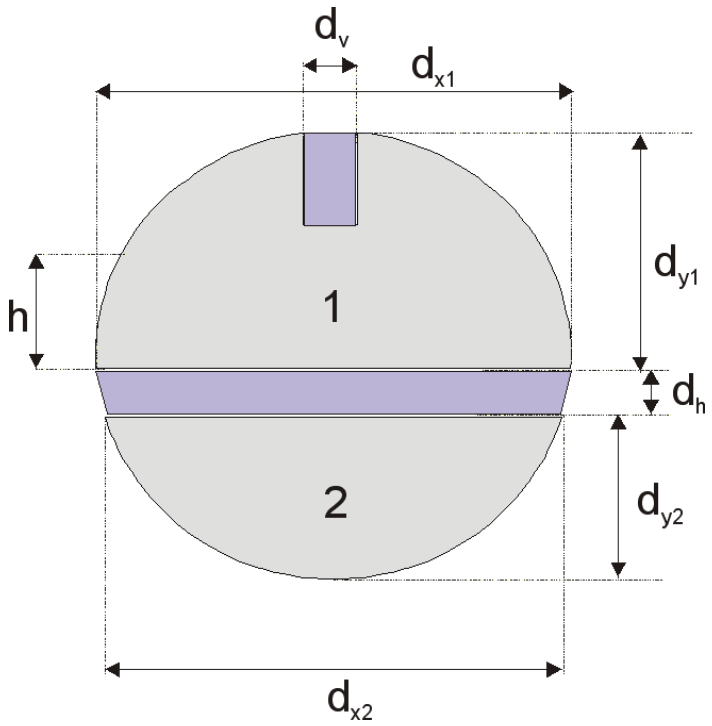

Figure 4.3: For calibration, the horizontal dimension of the droplet, d_{x1}, and the cross section were correlated to the diameter and cross section of a spherical droplet of the same volume [29].

4.1.2 Mathematical Model

The model is based on the Abramzon-Sirignano model [40] for convective droplet vaporization using a uniform temperature model as it was described in the Section 3.2.2. The model is based on the following assumptions: Considered is a single component droplet, isolated, isobaric, symmetric spherically, and suspended on two glass fibers. This is equivalent with the assumption of an infinite liquid heat conductivity. The temperature profile in the interior of the droplet is uniform but it increases with the time. These assumptions are satisfied in the experimental setup and they are taken into account in the numerical implementation. The description of the quasi-steady gas film can be summarized by the use of the Sherwood number Sh, the non-dimensional vaporization rate, the heat flux and the droplet motion. These quantities can be prescribed as functions of the transfer number B, the droplet Reynolds number Re. The vaporization rate and the other parameters will depend also on the ambient conditions outside the gas film, on the droplet surface conditions and on the laser characteristics. The lifetime of the droplet is assumed to be much longer than the time for the energy transport in the droplet. The model has been modified to treat the situation of hot droplets being exposed to a cold, convective air stream. Droplet interaction does not occur in the present arrangement. The modified expression for the droplet temperature accounts for

the laser-induced droplet heating at atmospheric pressure. Hence, the following liquid-phase equations are used to determine the droplet heating, vaporization rate, Sherwood number, and droplet motion.

Droplet Heating:

$$M_l C_{Pl} \frac{dT_l}{dt} = \dot{m} \left[\frac{C_{P,F}(T - T_l)}{B_H} - H_v \right] + W_{abs}. \tag{4.5}$$

Vaporization rate and droplet motion are already presented in equations (3.36) and (3.53).

The last term in the energy equation (4.5) is needed for the simulation of the absorbed energy flux W_{abs} of the pulsed laser beam. With the intensity of the incident light of the laser beam, I_0, and the spherical water droplet radius, R, the absorbed energy flux is given by [108]:

$$W_{abs} = Q_{abs} I_0 \pi R^2, \tag{4.6}$$

where Q_{abs} denotes the efficiency factor which can be computed via Mie scattering theory. The way of describing the light scattered from small spherical particles mainly depends on the ratio of the particle size and the wavelength of the incident light. The size parameter, defined by

$$\alpha = \frac{2\pi N R}{\lambda} \tag{4.7}$$

provides the distinctive criteria. Here, R is the radius and N is the refractive index of the particle. For $\alpha >> 1$ the scattering process is described by geometrical optics [109]. For $\alpha << 1$ the scattering process is described by the Rayleigh formalism, the scattered intensity mainly depends on the wavelength $I \approx \lambda^{-4}$ [110]. However, for our application the size parameter is in the regime $\alpha \approx 1$. For this condition the interaction of light and particle is described by Mie theory, named after the German physicist Gustav Mie (1869-1957). A program from [109] is used for computation of Q_{abs} which is based on the following equations:

$$Q_{abs} = Q_{ext} - Q_{sca}, \tag{4.8}$$

$$Q_{ext} = \frac{C_{ext}}{\pi R^2} \text{ and } Q_{sca} = \frac{C_{sca}}{\pi R^2}, \tag{4.9}$$

$$C_{sca} = \frac{2\pi}{k^2} \sum (2n+1)(\mid a_n \mid^2 + \mid b_n \mid^2), \tag{4.10}$$

$$C_{ext} = \frac{2\pi}{k^2} \sum (2n+1)\text{Real}\{a_n + b_n\}. \tag{4.11}$$

Here, Q_{ext} and Q_{sca} denote the efficiency factors for extinction and scattering, respectively, C_{ext} and C_{sca} are extinction cross section and scattering cross section, respectively, n is the real refractive index, m is the relative refractive index of particle and medium, and Real denotes the real part of the scattering coefficients. The scattering coefficients, a_n and b_n, from Mie theory are given by [109]:

$$a_n = \frac{m\psi_n(m\alpha)\psi_n^{'}(\alpha) - \psi_n(\alpha)\psi_n^{'}(m\alpha)}{m\psi_n(m\alpha)\xi_n^{'}(\alpha) - \xi_n(\alpha)\psi_n^{'}(m\alpha)} \tag{4.12}$$

$$b_n = \frac{\psi_n(m\alpha)\psi_n^{'}(\alpha) - m\psi_n(\alpha)\psi_n^{'}(m\alpha)}{m\psi_n(m\alpha)\xi_n^{'}(\alpha) - m\xi_n(\alpha)\psi_n^{'}(m\alpha)} \tag{4.13}$$

The functions ψ_n and ξ_n are the Riccati-Bessel functions [109]. The absorption cross section of a weakly absorbing sphere, like that of a small particle compared with the wavelength, λ, is proportional to its volume. This proportionality does not hold for infinitely large particle radius. The energy is absorbed primarily in the outer layer of a highly absorbing sphere (i.e. $2a\alpha >> 1$). With increasing of the radius, the absorption cross section becomes proportional to area instead of volume. Q_{ext} and Q_{sca} must not be negative, and Q_{ext} must be greater than Q_{sca} except for nonabsorbing sphere, in which instance they are equal. For the present conditions, Q_{abs} is computed to be close to unity ($Q_{abs} = 0.98$). Almost all of the light that enters in a sufficiently large sphere is absorbed, none of the non-reflected light will be transmitted [109]. The physical properties of the vaporizing droplet were adopted to water [111, 112].

4.2 Laminar Spray Flames in the Counterflow Configuration

4.2.1 Description of the Counterflow Configuration

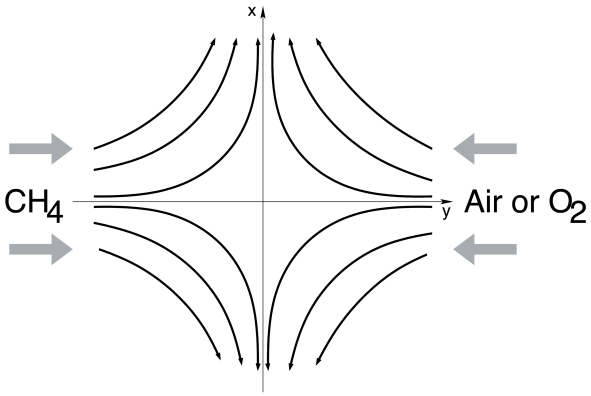

Figure 4.4: Schematic laminar spray flame in the counterflow configuration for CH_4/air(O_2).

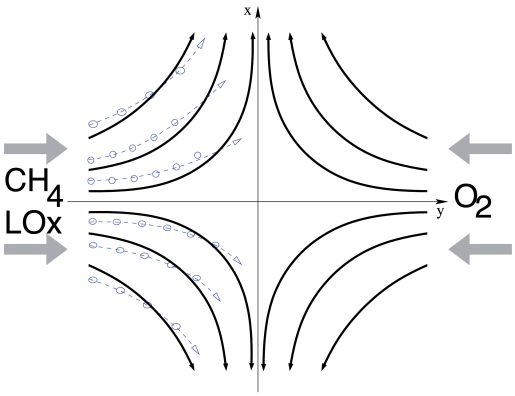

Figure 4.5: Schematic laminar spray flame in the counterflow configuration for CH_4/LOx

Figures 4.4 and 4.5 illustrate the system configuration. The lines show the gas phase streamlines. The x-axis represents the stagnation plane while y-axis represents the symmetry plane. As we know, air, fuel vapor, hot products, droplets can be fed from each side of the stagnation plane. In the present work, methane is fed against air or oxygen (gas) (see Figure 4.4) and liquid oxygen in the gaseous carrier methane is injected from left hand side of the stagnation plane whereas oxygen (gas) from the right hand side.

4.2.2 Mathematical Model

In this section governing equations for the counterflow configuration are presented and discussed. The mathematical model is based on Eulerian/Lagrangian formulation of non-dimensional equations [113, 114], where a similarity transformation transferring the two-dimensional equations into a one-dimensional system is applied. The governing equations for viscous flow with variable transport properties are given in [114].

4.2.2.1 Gas Phase

The conservation equations of the gas phase from Chapter 3.1.1, for the two dimensional counterflow configuration are formulated [114]. In the following, the conservation equations for mass, momentum and energy as well as the boundary conditions are formulated.

Continuity Equation
The steady state continuity equation, (3.5) becomes:

$$\frac{\partial(\rho u)}{\partial x} + \frac{\partial(\rho v)}{\partial y} = q_m. \tag{4.14}$$

This equation describes the mass conservation in a planar counterflow configuration. The parameter α, is equal to zero for planar configuration and equal to unity for axisymetric configuration. By adding the parameter α, the continuity equation turns into:

$$\frac{\partial([\alpha+1]\rho u)}{\partial x} + \frac{\partial(\rho v)}{\partial y} = q_m. \tag{4.15}$$

The boundary conditions of the continuity equation are the initial velocity at the spray side of the counterflow configuration and is given by:

$$\begin{aligned} u(y=-\infty) &= u_{-\infty}, \\ v(y=-\infty) &= v_{-\infty}. \end{aligned} \tag{4.16}$$

Species Mass Conservation Equation
The conservation of the mass species for the stationary case is given by [113, 115]:

$$\rho u\frac{\partial Y_i}{\partial x} + \rho v\frac{\partial Y_i}{\partial y} = \frac{\partial}{\partial y}\left(\rho V_{i,y}\right) + W_i\dot{\omega}_i + (\delta_i - Y_i)q_m. \tag{4.17}$$

In eq. (4.17), the term $V_{i,y}$ denotes the diffusion velocity in y direction and it is given by following equation:

$$V_{i,y} = -\frac{D_i}{\overline{W}}\frac{\partial(Y_i\overline{W})}{\partial y} - \frac{D_i^T}{\rho T}\frac{\partial T}{\partial y}. \tag{4.18}$$

The mass fractions at the boundary are given by:

$$\begin{aligned} Y_i(y=-\infty) &= Y_{i,-\infty}, \\ Y_i(y=+\infty) &= Y_{i,+\infty}. \end{aligned} \tag{4.19}$$

Momentum Conservation Equation

By using the continuity equation (3.5) in momentum conservation equation (3.13) and reducing the resultant equation to two dimensional cartesian space, the following form of the equation in x and y direction is obtained.

$$\begin{aligned} \rho\frac{\partial u}{\partial t} + \rho u\frac{\partial u}{\partial x} + \rho v\frac{\partial u}{\partial y} = &-\frac{\partial p}{\partial x} + \frac{\partial}{\partial x}\left[\mu\left(2\frac{\partial u}{\partial x} - \frac{2}{3}\left(\frac{\partial u}{\partial x} + \frac{\partial v}{\partial y}\right)\right)\right] \\ &+\frac{\partial}{\partial y}\left[\mu\left(\frac{\partial u}{\partial y} + \frac{\partial v}{\partial x}\right)\right] + \rho g_x + q_{p,x} - uq_m, \end{aligned} \tag{4.20}$$

$$\rho\frac{\partial v}{\partial t}+\rho u\frac{\partial v}{\partial x}+\rho v\frac{\partial v}{\partial y}=-\frac{\partial p}{\partial y}+\frac{\partial}{\partial y}\left[\mu\left(2\frac{\partial v}{\partial y}-\frac{2}{3}\left(\frac{\partial u}{\partial x}+\frac{\partial v}{\partial y}\right)\right)\right] +\frac{\partial}{\partial x}\left[\mu\left(\frac{\partial u}{\partial y}+\frac{\partial v}{\partial x}\right)\right]+\rho g_y+q_{p,y}-vq_m. \tag{4.21}$$

Assuming a steady state system and eliminating the boundary layer [115], the momentum equation can be rewritten as:

$$\rho u\frac{\partial u}{\partial x}+\rho v\frac{\partial u}{\partial y}=-\frac{\partial p}{\partial x}+\frac{\partial}{\partial y}\left(\mu\frac{\partial u}{\partial y}\right)+q_{p,x}-uq_m, \tag{4.22}$$

$$0=-\frac{\partial p}{\partial y}. \tag{4.23}$$

Therefore, the pressure in a boundary layer is steady crosswise to main stream direction and is virtually impressed to the boundary layer by the outside current. Hence, the pressure has to be considered as a known function which depends only on x. The pressure gradient in radial direction is determined by Euler's equation:

$$-\frac{\partial p}{\partial x}=\left(\rho u\frac{du}{dx}\right)\Big|_{-\infty}. \tag{4.24}$$

Now the equations (4.22) and (4.24) can be combined in the following form :

$$\rho u\frac{\partial u}{\partial x}+\rho v\frac{\partial u}{\partial y}=\left(\rho u\frac{du}{dx}\right)\Big|_{-\infty}+\frac{\partial}{\partial y}\left(\mu\frac{\partial u}{\partial y}\right)+q_{p,x}-uq_m. \tag{4.25}$$

Both boundary conditions which are necessary for the solution of this differential equation are:

$$\begin{aligned} u(y=-\infty)&=u_{-\infty},\\ u(y=+\infty)&=u_{+\infty}. \end{aligned} \tag{4.26}$$

Energy Conservation Equation
The energy conservation equation for the specific enthalpy (3.17) is used to obtain the desired temperature form, which is valid for ideal gases where $dh=C_pdT$ (3.17). By applying the boundary theory and considering small Mach numbers (low velocity), we get the desired form of energy conservation equation:

$$\rho uC_P\frac{\partial T}{\partial x}+\rho vC_P\frac{\partial T}{\partial y}=\frac{\partial}{\partial y}\left(\lambda\frac{\partial T}{\partial y}\right)-\rho\sum_{i=1}^{k}V_{i,y}C_{p,i}\frac{\partial T}{\partial y}-\sum_{i=1}^{k}W_i\dot{\omega}_ih_i+q_T, \tag{4.27}$$

where q_T denotes the source terms of the phase exchange.

The boundary conditions for the energy equation are:

$$\begin{aligned} T(y = -\infty) &= T_{-\infty}, \\ T(y = +\infty) &= T_{+\infty}. \end{aligned} \tag{4.28}$$

4.2.2.2 Source Terms of the Phase Exchange

Source Term in the Mass Conservation Equation

The source term of the phase exchange q_m in the mass conservation equation and species mass conservation equation is given by the following equation:

$$q_m = n\dot{m}. \tag{4.29}$$

Here, n denotes the number of droplets in the gas volume, so called droplet number density and $\dot{m}$ is single droplet vaporization mass flux (see Chapter 3.2).

Source Term in the Momentum Equation

The source term of the phase exchange in the vectorial form of the momentum conservation equation is given by:

$$\vec{q}_p = n\dot{m}\vec{v}_l - nm_l\frac{d\vec{v}_l}{dt}. \tag{4.30}$$

The component of the main flux direction of $\vec{q}_p$, used in Eq. (4.25), is given by:

$$\vec{q}_{p,x} = n\dot{m}\vec{u}_l - nm_l\frac{d\vec{u}_l}{dt}. \tag{4.31}$$

This equation represents the vaporization or condensation of mass flow of momentum between liquid and gas phase. Here, $\dot{m}$ is the mass flow of the vaporizing component, $\vec{v}_l$ is the velocity vector with the components u_l and v_l, and m_l is the mass of a droplet. The index l denotes sizes of the liquid phase. The index d marks the polydispersity of the sprays, in our case it is considered to be one for mono-disperse spray.

Source Term in the Energy Conservation Equation

In the energy conservation equation, the source term of the phase exchange is delivered by:

$$q_T = -n[\dot{q} + \dot{m}(\bar{c}_{p,f}(T - T_s) + L_{v,O_2}(T_s))]. \tag{4.32}$$

In this equation, $\dot{q}$ is the heat flux of inside of the droplet, $L_{v,O_2}(T_s)$ is the vaporization enthalpy of the liquid oxygen at the surface temperature T_s and $\bar{C}_{p,f}$ is the specific heat capacity at constant pressure of the gas mixture in a fictive droplet environment film.

4.2.2.3 Liquid Phase

The source terms of the phase exchange from Chapter 4.2.2.2 are functions of the droplet number density. They are derived from their dependence on the axial position of a droplet in the flow field. If the droplets are not generated or destroyed, it can be written for a droplet velocity field $\vec{v}_l$ and droplet number density n, the following equation [82, 113]:

$$\mathrm{div}(n\vec{v}_l) = 0. \tag{4.33}$$

This is the conservation equation for the number of droplets, for two-dimnsional case, which is equivalent with the following equation:

$$u_l\frac{\partial n}{\partial x} + v_l\frac{\partial n}{\partial y} + n\frac{\partial u_l}{\partial x} + n\frac{\partial v_l}{\partial y} = 0, \tag{4.34}$$

and, by definition,

$$\frac{dv_l}{dt} = \frac{\partial v_l}{\partial t}u_l\frac{\partial v_l}{\partial x} + v_l\frac{\partial v_l}{\partial y} \tag{4.35}$$

and

$$\frac{dn}{dt} = \frac{\partial n}{\partial t}u_l\frac{\partial n}{\partial x} + v_l\frac{\partial n}{\partial y}. \tag{4.36}$$

But it is a steady state case, it means that partial time dependent term is equal to zero. Also, the term $\partial v_l/\partial x$ from equation (4.35) is equal to zero for similarity. In order to calculate the term $\partial u_l/\partial x$, it is convenient to introduce the variable s [82, 113]:

$$s = \frac{x_l}{u_{l,0}}. \tag{4.37}$$

Here, the subscript 0 represents the variable at time t=0. Since $x_l = u_{l,0}s$, $u_l = dx_l/dt$, it follows the partial derivative $\partial u_l/\partial x$:

$$\frac{\partial u_l}{\partial x} = \frac{1}{s}\frac{ds}{dt} + x_l\frac{\partial}{\partial x}\left(\frac{1}{s}\frac{ds}{dt}\right). \tag{4.38}$$

If s_0 is set to be constant, then s will not depend on x and the equation (4.38) is reduced to:

$$\frac{\partial u_l}{\partial x} = \frac{1}{s}\frac{ds}{dt}. \tag{4.39}$$

Note that $s_0 = x_{l,0}/u_{l,0} = 1$ corresponds to matching gas and droplet velocity components along x at the starting location for the droplets. The equation (4.34), will be reformulated with the help of equations (4.35), (4.36), (4.39) as follows:

$$\frac{1}{n}\frac{dn}{dt} + \frac{1}{s}\frac{ds}{dt} + \frac{1}{v_l}\frac{dv_l}{dt} = 0. \tag{4.40}$$

From equation (4.40) follows:

$$\frac{d}{dt}(nsv_l) = nsv_l\frac{1}{n}\frac{dn}{dt} + \frac{1}{s}\frac{ds}{dt} + \frac{1}{v_l}\frac{dv_l}{dt} = 0. \tag{4.41}$$

The integration of the equation (4.41) leads to the form of droplet number density given by [82, 113]:

$$n = n_0\frac{s_0 v_{l,0}}{dt}(sv_l). \tag{4.42}$$

This equation is not dependent on x because $s \neq f(x)$ and $v_l \neq f(x)$.

4.2.3 Similarity Transformation

The Dimension of the Equations System

In the following chapters, all the equations for the modeling of laminar spray flame in counterflow configuration will be presented. To get a closer overview of solving the system of equations, all the equations will be summarized in the following. The Table 4.1 contains the equations describing the gas phase, Table 4.2 includes all the equations which describe the liquid phase and the Table 4.3 incorporate the source terms due to phase exchange during the vaporization. Also, the boundary conditions for solving the differential equations are given.

Dimensional physical quantities are indicated by a '$\hat{}$' sign. In the next subchapter, the reference quantities with superscript '$*$' will be introduced. Using these dimensional and reference quantities, all the dimensional equations of the model will become dimensionless [113]. The dimensionless quantities will be expressed in the following without any index. For a dimensionless physical quantity ϕ is applied:

$$\phi = \frac{\hat{\phi}}{\phi^*}. \tag{4.43}$$

The dimensionless equations will be transformed in the next step. Especially, the two dimensional conservation equations of the gas phase will become one dimensional using similarity analysis.

Introducing the Reference Quantities

Our case is a counterflow, for which the outer flow is the potential flow of two impinging streams described by:

$$\hat{y} = -\infty: \qquad \hat{u}(\hat{x}) = \hat{a}_-\hat{x}, \qquad \hat{v}(\hat{y}) = -\hat{a}_-\hat{y} \tag{4.44}$$

$$\hat{y} = +\infty: \qquad \hat{u}(\hat{x}) = \hat{a}_+\hat{x}, \qquad \hat{v}(\hat{y}) = -\hat{a}_+\hat{y} \tag{4.45}$$

Continuity Equation
$\frac{\partial([\alpha+1]\hat{\rho}\hat{u})}{\partial\hat{x}} + \frac{\partial(\hat{\rho}\hat{v})}{\partial\hat{y}} = \hat{q}_m$ BC: $\hat{v}(\hat{y}=-\infty) = \hat{v}_{-\infty}$
Species Mass Conservation Equation
$\hat{\rho}\hat{u}\frac{\partial Y_i}{\partial\hat{x}} + \hat{\rho}\hat{v}\frac{\partial Y_i}{\partial\hat{y}} = -\frac{\partial(\hat{\rho}\hat{V}_{i,y})}{\partial\hat{y}} + \hat{W}_i\hat{\dot{\omega}}_i + (\delta_{i,s} - Y_i)\hat{q}_m$ BC: $\hat{Y}_i(\hat{y}=-\infty) = \hat{Y}_{i,-\infty}$ and $\hat{Y}_i(\hat{y}=+\infty) = \hat{Y}_{i,+\infty}$
Momentum Conservation Equation
$\hat{\rho}\hat{u}\frac{\partial\hat{u}}{\partial\hat{x}} + \hat{\rho}\hat{v}\frac{\partial\hat{u}}{\partial\hat{y}} = \left(\hat{\rho}\hat{u}\frac{d\hat{u}}{d\hat{x}}\right)\Big\vert_{-\infty} + \frac{\partial}{\partial\hat{y}}\left(\hat{\mu}\frac{\partial\hat{u}}{\partial\hat{y}}\right) + \hat{q}_{p,x} - \hat{u}\hat{q}_m$ BC: $\hat{u}(\hat{y}=-\infty) = \hat{u}_{-\infty}$ and $\hat{u}(\hat{y}=+\infty) = \hat{u}_{+\infty}$
Energy Conservation Equation
$\hat{\rho}\hat{u}\hat{C}_P\frac{\partial\hat{T}}{\partial\hat{x}} + \rho\hat{v}\hat{C}_P\frac{\partial\hat{T}}{\partial\hat{y}} = \frac{\partial}{\partial\hat{y}}\left(\lambda\frac{\partial\hat{T}}{\partial\hat{y}}\right) - \rho\sum_{i=1}^{k}\hat{V}_{i,y}\hat{C}_{p,i}\mathrm{grad}\hat{T} - \sum_{i=1}^{k}\hat{W}_i\hat{\dot{\omega}}_i\hat{h}_i + \hat{q}_T$ BC: $\hat{T}(\hat{y}=-\infty) = \hat{T}_{-\infty}$ and $\hat{T}(\hat{y}=+\infty) = \hat{T}_{+\infty}$
Diffusion Velocities in $x-$ and $y-$Direction
$\hat{V}_{i,x} = -\frac{\hat{D}_i}{\hat{\overline{W}}}\frac{\partial(\hat{Y}_i\hat{\overline{W}})}{\partial\hat{x}} - \frac{\hat{D}_i^T}{\hat{\rho}\hat{T}}\frac{\partial\hat{T}}{\partial\hat{x}}$ $\hat{V}_{i,y} = -\frac{\hat{D}_i}{\hat{\overline{W}}}\frac{\partial(\hat{Y}_i\hat{\overline{W}})}{\partial\hat{y}} - \frac{\hat{D}_i^T}{\hat{\rho}\hat{T}}\frac{\partial\hat{T}}{\partial\hat{y}}$
Ideal Gas Law
$\hat{\rho} = \frac{\hat{p}\hat{\overline{W}}}{\hat{R}\hat{T}}$

Table 4.1: Dimensional conservation equations of the gas phase [104, 115]

Droplet Vaporization
$\frac{d\hat{R}}{d\hat{t}} = -\frac{\hat{\rho}_{g,f}\hat{D}_{g,f}}{2\hat{\rho}_l\hat{R}} \cdot \widetilde{\mathrm{Sh}} \cdot \ln(1+B_M)$ BC: $\hat{R}(\hat{t}=0) = \hat{R}_0$
Droplet Heating
$\frac{\partial\hat{T}_l}{\partial\hat{t}} = \frac{\hat{\alpha}_l}{\hat{r}^2}\frac{\partial}{\partial\hat{r}}\left(\hat{r}^2\frac{\partial\hat{T}_l}{\partial\hat{r}}\right)$ BC: $\left.\frac{\partial\hat{T}_l}{\partial\hat{r}}\right\vert_{\hat{r}=0} = 0$ $\left.\frac{\partial\hat{T}_l}{\partial\hat{r}}\right\vert_{\hat{r}=\hat{R}} = \frac{\hat{\dot{q}}}{4\pi\hat{R}^2\hat{\lambda}_{l,s}}$
Droplet Motion in $x-$ and $y-$ Direction
$\frac{4}{3}\pi\hat{R}^3\hat{\rho}_l\frac{d\hat{u}_l}{d\hat{t}} = \pi\hat{R}^2\frac{1}{2}\rho(\hat{u}-\hat{u}_l) \mid \hat{u}-\hat{u}_l \mid C_D + \frac{4}{3}\pi\hat{R}^3\hat{\rho}_l\hat{g}_x$ $\frac{4}{3}\pi\hat{R}^3\hat{\rho}_l\frac{d\hat{v}_l}{d\hat{t}} = \pi\hat{R}^2\frac{1}{2}\rho(\hat{v}-\hat{v}_l) \mid \hat{v}-\hat{v}_l \mid C_D + \frac{4}{3}\pi\hat{R}^3\hat{\rho}_l\hat{g}_y$ BC: $\hat{x}_l(\hat{t}=0) = \hat{x}_{l,0}$ $\hat{y}_l(\hat{t}=0) = \hat{y}_{l,0}$ $\hat{u}_l(\hat{t}=0) = \hat{u}_{l,0}$ $\hat{v}_l(\hat{t}=0) = \hat{v}_{l,0}$
Droplet Number Density
$\hat{n} = \hat{n}_0\frac{\hat{s}_0\hat{v}_{l,0}}{\hat{s}\hat{v}_l}$

Table 4.2: Dimensional equations of the liquid phase [104, 115]

Total Mass
$\hat{q}_m = \hat{n}\hat{\dot{m}}$
Momentum
$\hat{q}_{p,x} = -\hat{n}\left[\hat{\dot{m}}(\hat{u} - \hat{u}_l) + \hat{m}_l \frac{d\hat{u}_l}{d\hat{t}}\right]$
Energy
$\hat{q}_T = -\hat{n}[\hat{\dot{q}} + \hat{\dot{m}}(\hat{c}_{p,f}(\hat{T} - \hat{T}_s) + \hat{L}_{v,O_2}(\hat{T}_s))]$

Table 4.3: Dimensional source term equations due to vaporization in the equation from Table 4.1

Where $\hat{a}_-$ and $\hat{a}_+$ are the strain rates at left ($\hat{y} = -\infty$) and right ($\hat{y} = +\infty$) boundaries. The strain rates are equivalent with the velocity gradient and their unit is $[1/s]$. In an x, y plane, the above equations can be seen as stream lines(see Figures 4.4, 4.5).

If the reference frame is fixed to the stagnation plane, overall momentum balance requires for ∞ boundary conditions, that: $\hat{\rho}_- \hat{a}_-^2 = \hat{\rho}_+ \hat{a}_+^2$. When from both sides of the counterflow configuration, the gases are injected with the same temperature and composition and no chemical reactions are taking place, the total density is constant. From the overall momentum equation, follows then the strain rate $\hat{a} = \hat{a}_- = \hat{a}_+$.

In Figure 4.6, the axial velocity component $\hat{v}$ is plotted against the axial space coordinate $\hat{y}$ for $\hat{y} < 0$. The index "$-\infty$" indicates values on the left boundary of the counterflow configuration. In order to obtain a characteristic time constant for the flow, the equation $d\hat{t} = d\hat{y}/\hat{v}(\hat{y})$ has to be integrated from $\hat{t}_0 = 0$ to $\hat{t}$:

$$\hat{t} = \frac{1}{\hat{a}} \ln \frac{\hat{v}(\hat{y}_0)}{\hat{v}(\hat{y}(\hat{t}))} \tag{4.46}$$

Hereby $\hat{v}(\hat{t}) = -\hat{a}\hat{y}(\hat{t}) + \hat{v}_{-\infty}$. The time $\hat{t}$ obtained in (4.46) is the time needed to slow down the flow from $\hat{v}(\hat{y}_0)$ to $\hat{v}(\hat{y}(\hat{t}))$. The fraction $1/\hat{a}$ is the desired characteristic time, which is needed as a reference time when non-dimensionalizing the gas phase equation. Since the strain rate for reactive flows depends on the location, the value $1/\hat{a}_{-\infty}$ on the left boundary is taken as reference time.

Continillo and Sirignano [113, 115] introduced as reference time $t^* = 1/\hat{a}_{-\infty}$ as well as the following reference quantities for the gas phase equation:

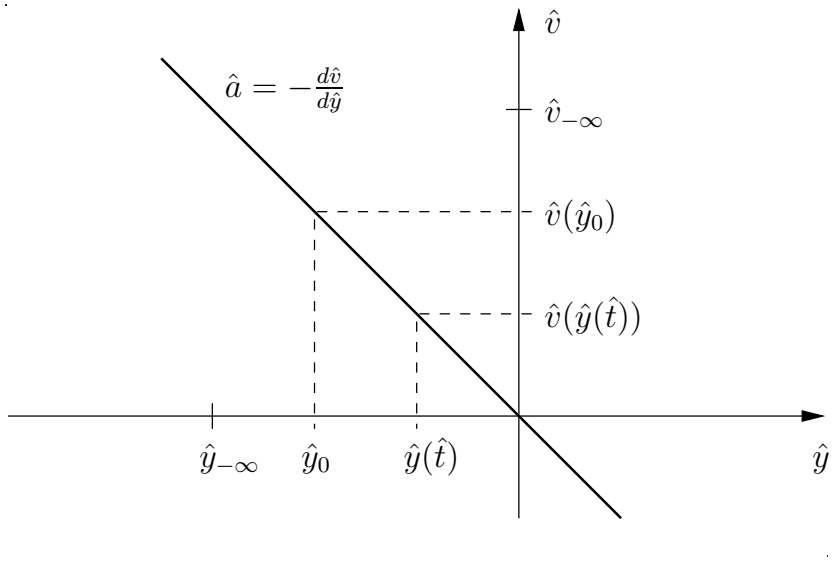

Figure 4.6: Schematic of the axial velocity component $\hat{v}$ plotted against the axial space coordinate $\hat{y}$.

$$
\begin{array}{lll}
l^* = \sqrt{\hat{v}_{-\infty}/\hat{a}_{-\infty}} & \rho^* = \hat{\rho}_{-\infty} & C_P^* = \hat{C}_{P-\infty} \\
T^* = \hat{T}_{-\infty} & W^* = \hat{W}_{-\infty}. &
\end{array}
$$

Through non-dimensionalization of the conservation equation by using the above reference quantities, following is obtained:

$$
\begin{array}{lll}
u^* = l^*/t^* & p^* = \rho^* u^{*2} & (W\dot{\omega})^* = \rho^* u^*/l^* \\
q_m^* = \rho^* u^*/l^* & q_{p,x}^* = \rho^* u^{*2}/l^* & q_T^* = \rho^* u^* C_P^* T^*/l^* \\
\mu^* = \rho^* u^* l^* & \lambda^* = \rho^* u^* l^* C_P^* & h^* = C_P^* T^* \\
V^* = u^* & D^* = l^{*2}/t^* & D^{T*} = \rho^* l^{*2}/t^*.
\end{array}
$$

Moreover, the following reference quantities for the liquid phase and the source terms are needed [113–115]:

$$
\begin{array}{llll}
l_l^* = \hat{R}_0 & t_l^* = \frac{l_l^{*2}}{\hat{\alpha}_l} & T_l^* = T^* & \alpha_l^* = l^{*2}/t^* \\
\lambda_l^* = \alpha_l^* \rho^* C_P^* & \dot{m}^* = \rho^* u^* l^{*2} & \dot{q}^* = \dot{m}^* C_P^* T^* & M^* = \rho^* l^{*3} \\
M_l^* = 4/3\pi l_l^{*3} \hat{\rho}_l & \rho_{g,f}^* = \rho^* & D_{g,f}^* = l^{*2}/t^* & n^* = 1/l^{*3} \\
u_l^* = l_l^*/t^* & L_v^* = C_P^* T^* & \dot{m}_l^* = M_l^*/t_l^*. &
\end{array}
$$

Finally, the corresponding dimensionless system of equations can be easily obtained from the above considerations by simple algebraic manipulation.

Transformation of the Equations

A similarity transformation is applied to the gas phase equations in order to reduce the two-dimensional gas phase equations to one-dimensional equations. Hereby, it is assumed that the flow field is similar, i.e. the conservation quantities are independent of that space coordinates which are orthogonal to the axial flow direction. Consequently, the partial derivatives $\partial\phi/\partial x$ disappear in the species, momentum, and energy conservation equations.

The reduction of the gas phase equation from a two to an one dimensional equation is achieved by introducing the stream function f [113, 114]:

$$f = \int_0^\eta \frac{u}{x} d\eta \tag{4.47}$$

The similarity variable η in equation (4.47) is defined as a density weighted axial space coordinate [113, 114] :

$$\eta = \int_0^y \rho dy. \tag{4.48}$$

The transformation of the dimensionless continuity equation yields a simple expression for the axial velocity:

$$v = -\frac{1}{\rho}([\alpha + 1]f + f_v) \tag{4.49}$$

with

$$f_v = -\int_0^\eta \frac{1}{\rho} q_m d\eta. \tag{4.50}$$

After transforming the species, momentum and energy conservation equation into non-dimensional equations, by using the boundary conditions from Table 4.1, and by applying the similarity transformation, one obtains the equations shown in Table 4.4, where the transformed continuity equation (4.49) has been substituted into all three conservation equations.

In the next step, the liquid phase equations are transformed. The following constants are needed [113, 114]:

$$\xi_s = \frac{\hat{R}}{\hat{v} R_0}, \quad d\tau = \frac{d\hat{t}}{\xi_s t_l^*}, \quad \xi = \frac{\hat{r}}{\hat{R}} \quad \text{as well as} \quad d\eta_l = \rho dy_l. \tag{4.51}$$

ξ_s is the dimensionless droplet radius, τ a dimensionless time constant, ξ the dimensionless radial space coordinate with its origin in the droplet center, and η is the transformed,

density weighted, axial position of the droplet in the counterflow configuration. The transformed equations of the liquid phase are shown in Table 4.5. Due to the similarity assumption, all the coefficients in the droplet momentum equation for the axial flow direction are independent of $\hat{x}$, except the droplet radius $\hat{R}$. If also the time derivative of the droplet radius is assumed to be independent of $\hat{x}$ in the flow field, then this implies that all droplets have the same $\hat{y}$ trajectory. The condition $\hat{R} \neq f(\hat{x})$ is satisfied, if the boundary conditions of the $\hat{y}$ momentum equation in Table 4.2 are independent of $\hat{x}$. Hence, they have been chosen according to Table 4.5.

After transforming the dimensional source terms in Table 4.3 into dimensionless source terms by using the introduced reference quantities, a similarity transformation is applied utilizing the equations (4.47), (4.48) and (4.51).

For the dimensionless vaporization rate $\dot{m}$, one obtains after transforming (3.45) [113, 114]:

$$\dot{m} = -3\frac{M_l^*}{M^*}\frac{t^*}{t_l^*}\xi_s\frac{d\xi_s}{d\tau}. \tag{4.52}$$

Using the relation $\hat{u}_1 = d\hat{x}_1/d\hat{t}$, the following equation for the dimensionless axial droplet velocity can be obtained:

$$u_l = -3\frac{t^*}{t_l^*}\frac{1}{\xi_s}\frac{x_l}{s}\frac{ds}{d\tau}. \tag{4.53}$$

The dimensionless accelaration of a single droplet in axial direction is given by:

$$\frac{du_l}{dt} = \frac{t^*}{t_l^*}\frac{1}{\xi_s}\frac{x_l}{s}\left[\frac{d^2s}{d\tau^2} - \frac{1}{\xi_s}\frac{d\xi_s}{d\tau}\frac{ds}{d\tau}\right]. \tag{4.54}$$

After substituting equations (4.52, 4.53, 4.54) into the equations in Table 4.3, one obtains the expressions for the transformed, dimensionalless source terms for the phase exchange as shown in Table 4.6.

Continuity Equation
$v = -\frac{1}{\rho}([\alpha+1]f + f_v) \qquad \text{with} \qquad f_v = -\int_0^\eta \frac{1}{\rho} q_m d\eta$ BC: $f(\eta = -\infty) = f_{-\infty}$
Species Mass Conservation Equation
$-\frac{d}{d\eta}(\rho V_{i\eta}) + ([\alpha+1]f + f_v)\frac{dY_i}{d\eta} = -\frac{W_i \dot{\omega}_i}{\rho} - (\delta_{i,s} - Y_i)\frac{q_m}{\rho}$ BC: $Y_i(\eta = -\infty) = Y_{i,-\infty}$ and $Y_i(\eta = +\infty) = Y_{i,+\infty}$
Momentum Conservation Equation
$\frac{d}{d\eta}\left(\rho\mu\frac{df'}{d\eta}\right) + ([\alpha+1]f + f_v)f'' = (f')^2 - \frac{1}{\rho} - \frac{q_{p,x} - u q_m}{\rho x}$ BC: $f'(\eta = -\infty) = 1$ and $f'(\eta = +\infty) = \sqrt{\frac{\rho_{-\infty}}{\rho_{+\infty}}}$
Energy Conservation Equation
$\frac{d}{d\eta}\left(\lambda\rho\frac{dT}{d\eta}\right) + C_P([\alpha+1]f + f_v)\frac{dT}{d\eta} = \rho\sum_{i=1}^k V_{i,\eta} C_{p,i}\frac{dT}{d\eta} + \frac{1}{\rho}\sum_{i=1}^k W_i \dot{\omega}_i h_i - \frac{q_T}{\rho}$ BC: $T(\eta = -\infty) = 1$ and $T(\eta = +\infty) = T_{+\infty}$
Diffusion Velocities in $x-$ and $y-$Direction
$V_{i,\eta} = -\frac{\rho D_i}{\overline{W}}\frac{d(Y_i\overline{W})}{d\eta} - \frac{D_i^T}{T}\frac{dT}{d\eta}$
Ideal Gas Law
$\rho = \frac{\overline{W}}{T}$

Table 4.4: Dimensionless conservation equations of the gas phase [114]

Droplet Vaporization
$\frac{d\xi_s}{d\tau} = -\frac{1}{9} a \rho_{g,f} D_{g,f} \widetilde{\mathrm{Sh}} \ln(1 + B_M)$ BC: $\xi_s(\tau = 0) = 1$
Droplet Heating
$\frac{\partial T_l}{\partial \tau} = \left(\frac{2}{\xi_s \xi} + \frac{\xi}{\xi_s} \frac{d\xi_s}{d\tau} \right) \frac{\partial T_l}{\partial \xi} + \frac{1}{\xi_s} \frac{\partial^2 T_l}{\partial \xi^2}$ BC: $\left. \frac{\partial T_l}{\partial \xi} \right\vert_{\xi=0} = 0$ $\left. \frac{\partial T_l}{\partial \xi} \right\vert_{\xi=\xi_s} = \frac{1}{4\pi \lambda_{l,s} b \xi_s} \dot{q}$
Droplet Motion in $x-$ and $y-$ Direction
$\frac{d^2 x_l}{d\tau^2} - \frac{1}{\xi_s} \left(\frac{d\xi_s}{d\tau} - a\mu \right) \frac{dx_l}{d\tau} = ab\mu \frac{df}{d\eta} x_l + b^2 \xi_s^2 g_x$ $\frac{d^2 \eta_l}{d\tau^2} + \rho \frac{d\rho^{-1}}{d\tau} \frac{d\eta_l}{d\tau} - \frac{1}{\xi_s} \left(\frac{d\xi_s}{d\tau} - a\mu \right) \frac{d\eta_l}{d\tau} = -ab\mu([\alpha + 1]f + f_v) + \rho b^2 \xi_s^2 g_\eta$ BC: $x_l(\tau = 0) = x_{l,0}$ $\eta_l(\tau = 0) = \eta_{l,0}$ $x_l^{'}(\tau = 0) = u_{l,0}$ $\eta_l^{'}(\eta = 0) = \eta_{l,0}^{'}$
Droplet Number Density
$n = n_0 \frac{s_0 \eta_{l,0}^{'} \rho}{s \eta_l^{'} \rho_0}$
Constants
$a = 6\pi \frac{t_1^*}{t^*} \frac{M^*}{M_l^*} \frac{l_l^*}{l^*}$ $b = \frac{t_l^*}{t*}$

Table 4.5: Dimensionless equations of the liquid phase, see Gutheil [114]

Total Mass
$\frac{q_m}{\rho} = -3\frac{M_l^*}{M^*}\frac{t^*}{t_l^*}\frac{n}{\rho}\xi_s\frac{d\xi_s}{d\tau}$
Momentum
$-\frac{q_{p,x}-uq_m}{\rho x} = \frac{M_l^*}{M^*}\left(\frac{t^*}{t_l^*}\right)^2\frac{n}{\rho s}\left[2\frac{d\xi_s}{d\tau}\frac{ds}{d\tau} + \xi_s\frac{d^2s}{d\tau^2} - 3\frac{t_l^*}{t^*}\xi_s f' s\frac{d\xi_s}{d\tau}\right]$
Energy
$-\frac{q_T}{\rho} = \frac{M_l^*}{M^*}\frac{t^*}{t_l^*}\frac{n}{\rho}\frac{\hat{C}_{P,F}}{C_P}\dot{m}\left(T - T_{l,s}\frac{T_l^*}{T^*}\right)\frac{1+B_T}{B_T}$

Table 4.6: Dimensionless source term equations for the phase exchange [114]

4.2.4 Numerical Algorithm

In this section, a numerical scheme is explained [116] to solve the equations discussed above.

4.2.4.1 Discretization of the Model

In the following, the mathematical model described by a system of partial differential equations (PDEs) is discretized in order to obtain an algebraic system of equations for the conserved quantities at given grid points.

This is done, first by defining a grid over the computation domain and second by approximating the partial derivatives at each grid point in an appropriate way. As a result, an algebraic equation at each grid point is obtained which contains the conserved quantities at a given grid point and its neighboring grid points as unknown variables.

All PDEs in the mathematical model are of second order or less. The general form is given by:

$$\frac{\partial\phi}{\partial t} = A\frac{\partial^2\phi}{\partial\eta^2} + B\frac{\partial\phi}{\partial\eta} + C\phi + D. \tag{4.55}$$

Goal of the discretization is the computation of the stationary solution of the PDE system. The spatial derivatives of first and second order in equation (4.55) are described by a parabola $\phi = a\eta^2 + b\eta + c$. The coefficients a, b, c are uniquely determined by the

values of the parabola at three neighboring points [117]. In particular, the goal is to solve

$$\begin{aligned}\phi_{i+1} &= a_i\eta_{i+1}^2 + b_i\eta_{i+1} + c_i\phi_i = a_i\eta_i^2 + b_i\eta_i + c_i \\ \phi_{i-1} &= a_i\eta_{i-1}^2 + b_i\eta_{i-1} + c_i.\end{aligned} \tag{4.56}$$

in order to obtain the coefficients a_i and b_i, which are needed to compute the derivatives in the spatial domain η:

$$\left.\frac{\partial\phi}{\partial\eta}\right|_{\eta_i} = 2a_i\eta_i + b_i \tag{4.57}$$

$$\left.\frac{\partial^2\phi}{\partial\eta^2}\right|_{\eta_i} = 2a_i \tag{4.58}$$

The solution of the system (4.56) is given by

$$a_i = \frac{\frac{1}{\Delta\eta_i}\phi_{1-1} - \left(\frac{1}{\Delta\eta_i} + \frac{1}{\Delta\eta_{i+1}}\right)\phi_i + \frac{1}{\Delta\eta_{i+1}}\phi_{i+1}}{\Delta\eta_i + \Delta\eta_{i+1}} \tag{4.59}$$

$$b_i = \frac{\phi_i - \phi_{i-1}}{\Delta\eta_i} - a_i(\eta_{i-1} + \eta_i). \tag{4.60}$$

where $\Delta\eta_{+1} = \eta_{+1} - \eta$ is the grid spacing s. By substituting the coefficients a_i and b_i in equation (4.57), one obtains the following approximation for the first derivative

$$\left.\frac{\partial\phi}{\partial\eta}\right|_{\eta_i} = G_1\frac{\phi_i - \phi_{i-1}}{\Delta\eta_i} + G_2\frac{\phi_{i+1} - \phi_i}{\Delta\eta_{i+1}} \tag{4.61}$$

with the weight factors

$$G_1 = \frac{\Delta_{i+1}}{\Delta\eta_i} + \Delta\eta_{i+1} \tag{4.62}$$

$$G_2 = \frac{\Delta_i}{\Delta\eta_i} + \Delta\eta_{i+1} \tag{4.63}$$

By using an equidistant grid, the weight factors are both 0.5. In that case, equation (4.61) is called a central difference, that means the approximation of the derivative is given by linear function where the slope of the function is the first derivative at η (see Figure 4.7).

Figure 4.7: Schematic of the approximation of first derivative.

As will become clear later, an equidistant grid is not appropriate in our case because of the large gradients in the profile of the conservation quantities. Hence, the approximation defined by (4.61), which allows to use variable grid size, is used in the counterflow simulations to ensure numerical stability:

$$\left.\frac{\partial\phi}{\partial\eta}\right|_{\eta_i} = \frac{1}{2}\frac{\phi_i - \phi_{i-1}}{\Delta\eta_i} + \frac{1}{2}\frac{\phi_{i+1} - \phi_i}{\Delta\eta_{i+1}} \tag{4.64}$$

$$= -\frac{1}{2}\frac{1}{\Delta\eta_i}\phi_{i-1} + \left(\frac{1}{\Delta\eta_i} + \frac{1}{\Delta\eta_{i+1}}\right)\phi_i + \frac{1}{2}\frac{1}{\Delta\eta_{i+1}}\phi_{i+1} \tag{4.65}$$

$$= K_{1,i}\phi_{i-1} + K_{2,i}\phi_i + K_{3,i}\phi_{i+1}. \tag{4.66}$$

The application of the central difference for convective terms might cause numerical problems. It is often unstable and causes overshoots in the profiles of the considered variable [118]. Hence, dependent on the sign of the factor B_i^t in equation (4.55), the forward respectively the backward difference is used for discretization (see figure 4.7).

For $B_i^t > 0 \Rightarrow$ Forward difference:

$$\left.\frac{\partial\phi}{\partial\eta}\right|_{\eta_i} = \frac{\phi_{i+1} - \phi_i}{\Delta\eta_{i+1}} = -\frac{1}{\Delta\eta_{i+1}}\phi_i + \frac{1}{\Delta\eta_{i+1}}\phi_{i+1} = K_{2,i}\phi_i + K_{3,i}\phi_{i+1}. \tag{4.67}$$

For $B_i^t < 0 \Rightarrow$ Backward difference:

$$\left.\frac{\partial\phi}{\partial\eta}\right|_{\eta_i} = \frac{\phi_i - \phi_{i-1}}{\Delta\eta_i} = -\frac{1}{\Delta\eta_i}\phi_{i-1} + \frac{1}{\Delta\eta_i}\phi_i = K_{1,i}\phi_{i-1} + K_{2,i}\phi_i \tag{4.68}$$

The second derivative is given by substituting the coefficient a_i (equation (4.59)) in equation(4.58):

$$\begin{aligned}\left.\frac{\partial^2\phi}{\partial\eta^2}\right|_{\eta_i} = \frac{2}{\Delta\eta_i(\Delta\eta_i + \Delta\eta_{i+1})}\phi_{i-1} - \frac{2}{\Delta\eta_i + \Delta\eta_{i+1}}\phi_i + \frac{2}{\Delta\eta_{i+1}(\Delta\eta_i + \Delta\eta_{i+1})}\phi_{i+1} \\ = K_{4,i}\phi_{i-1} + K_{5,i}\phi_i + K_{6,i}\phi_{i+1}.\end{aligned} \tag{4.69}$$

Finally, in equation (4.55), the time derivative of the conserved quantity ϕ is approximated by

$$\left.\frac{\partial\phi}{\partial t}\right|_{t+\Delta t} = \frac{\phi_i^{t+\Delta t} - \phi_i^t}{\Delta t}. \tag{4.70}$$

After introducing all approximations for the derivatives in the PDE, the approximations can be substituted in equation (4.55). As a result, the following system of equations is obtained:

$$\alpha_i^t\phi_{i-1}^{t+\Delta t} + \beta_i^t\phi_i^{t+\Delta t} + \gamma_i^t\phi_{i+1}^{t+\Delta t} = \delta_i^t \tag{4.71}$$

with

$$\begin{aligned}\alpha_i^t &= A_i^t K_{4,i} + B_i^t K_{1,i} \\ \beta_i^t &= A_i^t K_{5,i} + B_i^t K_{2,i} + C_i^t - \frac{1}{\Delta t} \\ \gamma_i^t &= A_i^t K_{6,i} + B_i^t K_{3,i} \\ \delta_i^t &= -\left(\frac{\phi_i^t}{\Delta t} + D_i^t\right).\end{aligned} \tag{4.72}$$

In matrix form, equation (4.72) can be written as

$$\begin{pmatrix} \beta_2^t & \gamma_2^t & 0 & & & & & \\ & \alpha_3^t & \beta_3^t & \gamma_3^t & & & & \\ & & . & . & . & & & \\ & & & . & . & . & & \\ & & & & . & . & . & \\ & & & & & \alpha_{m-2}^t & \beta_{m-2}^t & \gamma_{m-2}^t \\ & & & & & 0 & \alpha_{m-1}^t & \beta_{m-1}^t \end{pmatrix} \begin{pmatrix} \phi_2^{t+\Delta t} \\ \phi_3^{t+\Delta t} \\ . \\ . \\ . \\ \phi_{m-2}^{t+\Delta t} \\ \phi_{m-1}^{t+\Delta t} \end{pmatrix} = \begin{pmatrix} \delta_2^t - \alpha_2^t\phi_1^{t+\Delta t} \\ \delta_3^t \\ . \\ . \\ . \\ \delta_{m-2}^t \\ \delta_{m-1}^t - \gamma_{m-1}^t\phi_m^{t+\Delta t} \end{pmatrix}. \tag{4.73}$$

As can be seen, a tridiagonal linear system of equations must be solved to obtain the solution vector $(\phi_2^{t+\Delta t}, \ldots, \phi_{m-1}^{t+\Delta t})^T$. Hereby, the coefficients A, B, C, D and a, b, c, d are determined at time t and the spatial derivatives of the conserved quantities at time $t + \Delta t$.

Solving the system of equations is only possible, if the boundary conditions are given, i.e. the values for $\phi_1^{t+\Delta t}$ and $\phi_m^{t+\Delta t}$ must be known. The boundary values have to be either defined by absolute values (for example the boundary conditions of the species-, momentum-, and energy conservation equations) or in terms of gradients (for example the boundary conditions of the energy equation for droplet heating).

In order solve the system of equations in (4.72), the socalled Thomas algorithm [119] is used. Hereby, the tridiagonal matrix is decomposed into a lower and upper triangular matrix and the solution is obtained by forward and backward substitution.

4.2.4.2 Linearization of the Source Terms

4.2.4.3 Numerical Method for the Mathematical Model

A flow chart for the numerical solution of the overall system of equations is shown in Figure 4.8. At the beginning, inital values and parameters are initialized. The initial values are obtained either from estimates (approximations) or from previous iterations. After that, if necessary, a new grid will be generated. The grid is refined at places where gradients are large. In the following two steps, the equations for the liquid phase are solved, using the method of Lagrange, and the source terms for the phase exchange are computed. After the source terms have been computed, the gas phase equations are iteratively solved. One iterations consists of several steps: the computation of the gas density, the computation of the chemical data, as well as the sequential solution of the Eulerian conservation equations with the help of the Thomas algorithm. Experience shows that about 100 gas phase iterations are reasonable before checking convergence. In case convergence has not been achieved, a new grid is generated and the solution of the equations for the liquid phase has to be recomputed. At the end of the iterations, when the solution vector does not change significantly anymore, no new grid is generated.

The computation is successfully completed if the stream function f satisfies

$$\frac{\sum_{i=2}^{M-1} (f_i^{t+\Delta t} - f_i^t)}{f_1^{t+\Delta t}} < 10^{-5} \tag{4.74}$$

and the residues $R_{i,j}$ of all gas phase equations satisfy

$$\frac{\sum_{j=1}^{J} \left(\sum_{i=2}^{M-1} [(R_{i,j})^2 \Delta\eta_i] \right)}{J \sum_{i=2}^{M-1} \Delta\eta_i} < 10^{-8}. \tag{4.75}$$

Hereby, J denotes the number of equations, in this case 37 (when the continuity equations are used in the momentum, energy, and in the 35 balance equations for the

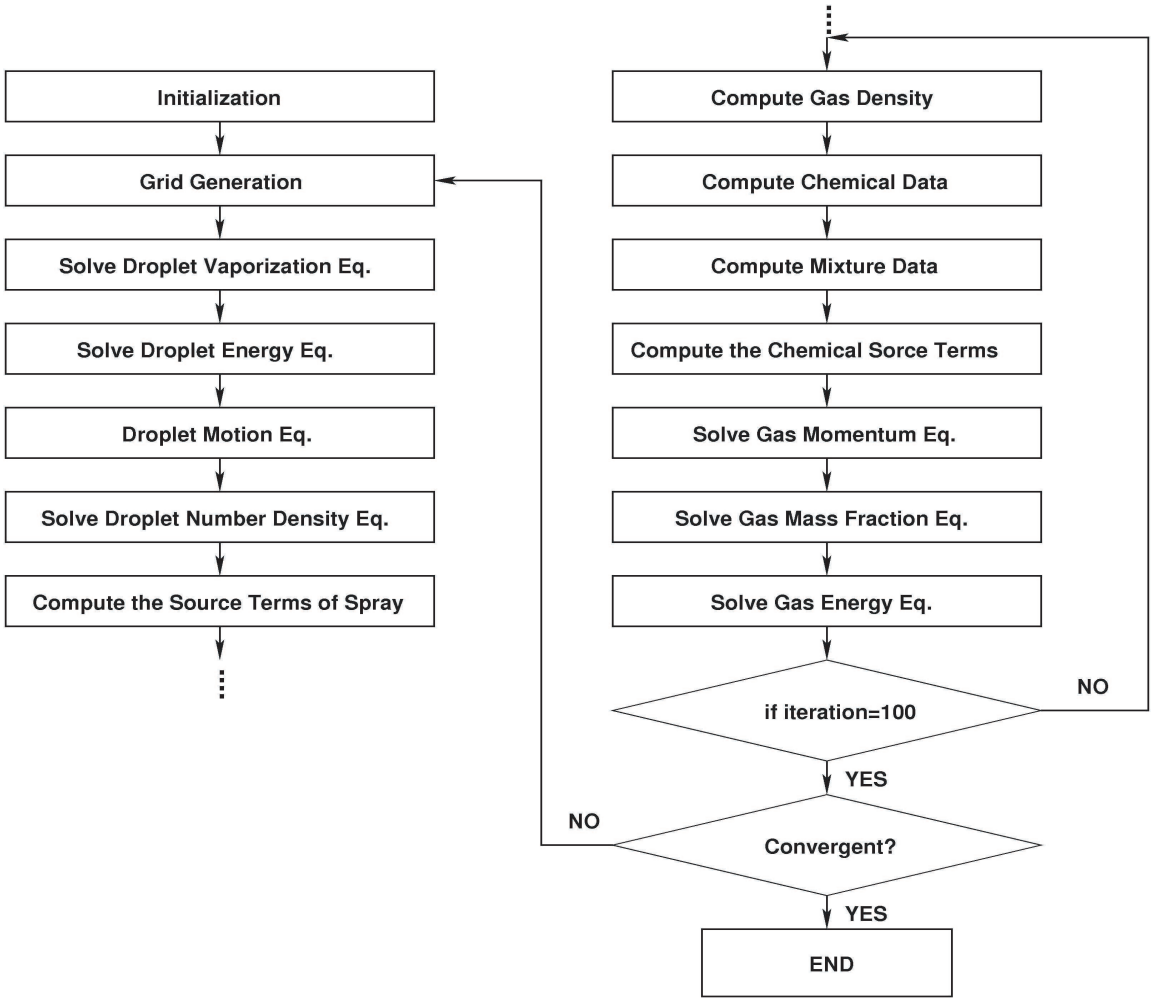

Figure 4.8: Schematic numerical flowchart of solution of the system of equations.

mass fractions of the chemical species) and M denotes the number of grid points. The residuum of equation j at the grid point i is defined by:

$$R_{i,j} = -A^t_{i,j}\left(\frac{\partial^2\phi}{\partial\eta^2}\right)^{t+\Delta t}_{i,j} - B^t_{i,j}\left(\frac{\partial\phi}{\partial\eta}\right)^{t+\Delta t}_{i,j} - C^t_{i,j}(\phi)^{t+\Delta t}_{i,j} - D^t_{i,j}. \tag{4.76}$$

5 Results and Discussion

5.1 Single Droplet Vaporization

The mathematical model was implemented and simulated in Fortran based on the uniform temperature field model 4.1.2. Some modifications in the initial vaporization model were necessary to be done in order to apply it to the setup used here, in particular, to take heating by a pulsed laser beam into account. It should be noticed since a pulsed laser beam is used so only a certain fraction of the laser energy is absorbed by the droplet. This, of course, needs to be addressed in equation (4.5). For this purpose, major aspects of the initial simulation parameters are summarized in the following.

A uniform temperature field inside the droplet was assumed during the vaporization process. The physical properties of the vaporizing droplet were adapted to water. The initial radius of water droplet is about 1.3 mm. The initial droplet temperature is room temperature, i.e., 293 K and the ambient gas temperature is also 293 K. Four different pulse lengths were used, namely 2 ms, 5 ms, 8 ms and 15 ms. Pressure is considered to be 1 bar.

Figure 5.1 shows the droplet diameter versus time obtained from the simulations (lines) and the experiment (symbols) for four different laser pulse durations of 2 ms, 5 ms, 8 ms, and 15 ms. The discrepancies between measurement and simulation are attributed to distortions of the droplet by suspending fibers leading to a deviation from the spherical shape. It can be further seen that the life times of droplets strongly depend upon the laser pulse duration time.

Figure 5.2 shows the droplet temperature versus time obtained from the simulations (lines) and the experiment (symbols), for different laser pulse durations of 2 ms, 5 ms, 8 ms, and 15 ms. It can be seen, especially for 2 ms laser pulse duration, the same behavior as in diagram 5.3 which shows the decrease of the relative droplet surface d^2/d_0^2 as a function of time. According to the d_2 law a linear decrease is expected. The evaporation takes place in two phases. As long as the temperature of the droplet is below the equilibrium temperature [28], energy is consumed for increasing the droplet temperature and the evaporation rate is reduced. When the droplet reaches its equilibrium temperature (in this example after approx. 37 s) all the heating energy is used to evaporate the liquid and the evaporation rate increases.

The droplet temperatures versus time obtained from the simulations, for different laser pulse durations of 2 ms, 5 ms, 8 ms, and 15 ms are presented in Figure 5.4. It can

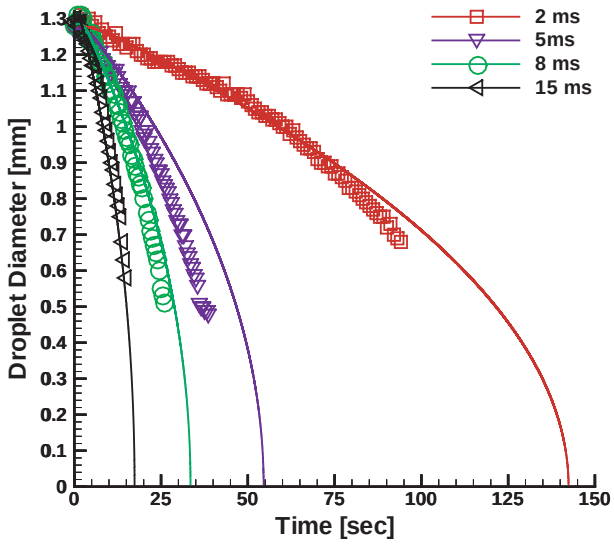

Figure 5.1: Simulated (lines) and measured (symbols) time dependence of droplet diameter for different laser pulse duration times.

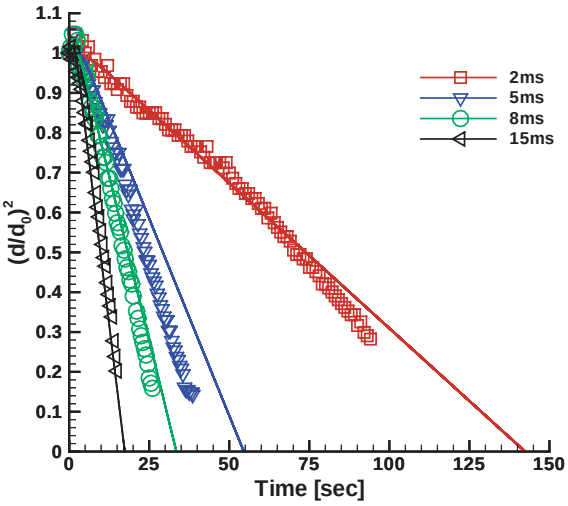

Figure 5.2: Simulated (lines) and measured (symbols) time dependence of d^2/d_0^2 for different laser pulse duration times.

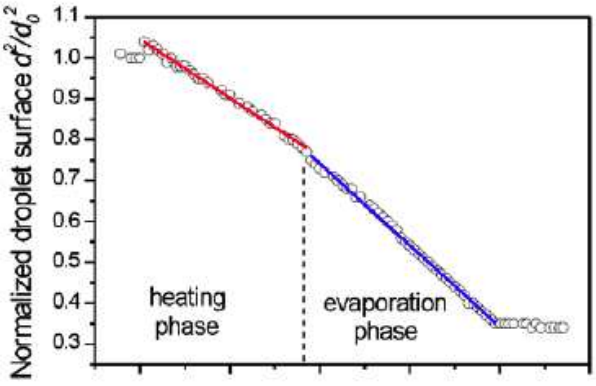

Figure 5.3: Temporal evolution of the droplet surface for d^2/d_0^2 [28]

be seen that for longer laser pulses, the droplet temperature is higher and closer to the boiling temperature of the liquid. Also, the total heating time is longer for shorter laser pulses (i.e. smaller duty cycles). Unfortunately, the liquid temperature inside the

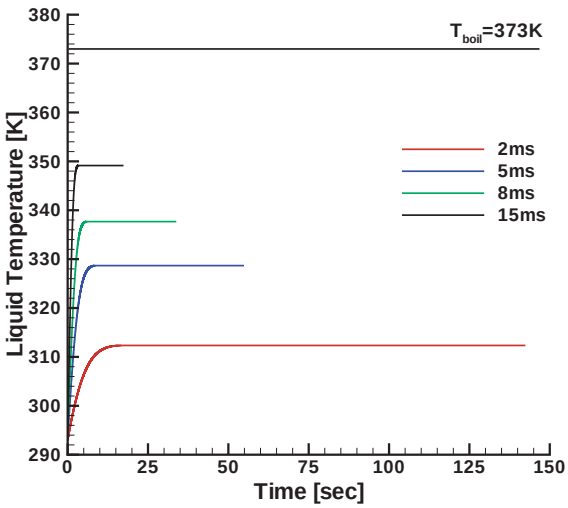

Figure 5.4: Computed droplet temperature versus time for different laser pulse duration times.

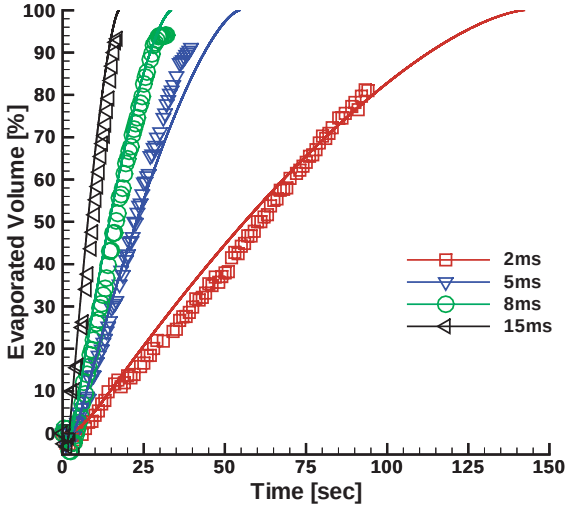

Figure 5.5: Computed and experimental droplet evaporated volume versus time for different laser pulse duration times.

droplet could not be measured, so that a validation of the calculated liquid-phase temperatures was not possible. In Figures 5.5, 5.6 and 5.7, the simulated and experimental results of the droplet evaporated volume versus time for the different pulse duration times are presented. The percentage of evaporated volume is computed according to equation (5.1) as follows:

$$V_{evap} = \left(1 - \left(\frac{R}{R_0}\right)^3\right) \cdot 100, \tag{5.1}$$

where R denotes the instantaneous radius of the droplet during the evaporation process, and R_0 is the initial droplet radius.

The enlarged view of the evaporated droplet volume versus time at the beginning of the evaporation process can be seen in Figures 5.6 and 5.7. It can be seen that the numerical simulations and experimental results of evaporated volume are in good agreement. The experimental error is about $2-3\%$, and some error bars are introduced into the figures. It is observed that at the beginning of the evaporated process, there is an expansion of the droplet. In order to distinguish between droplet size increase due to condensation or due to droplet expansion because of temperature-dependent density variation, the percentage evaporated droplet mass versus time is displayed in Figure 5.8. The percentage evaporated droplet mass is computed according to the equation (5.2):

$$M_{evap} = \left(1 - \frac{M}{M_0}\right) \cdot 100, \tag{5.2}$$

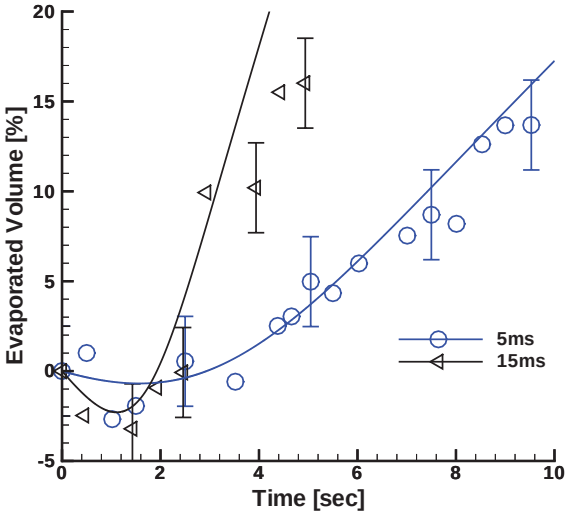

Figure 5.6: Computed and experimental droplet evaporated volume versus time for different laser pulse duration times, at the beginning of the evaporation.

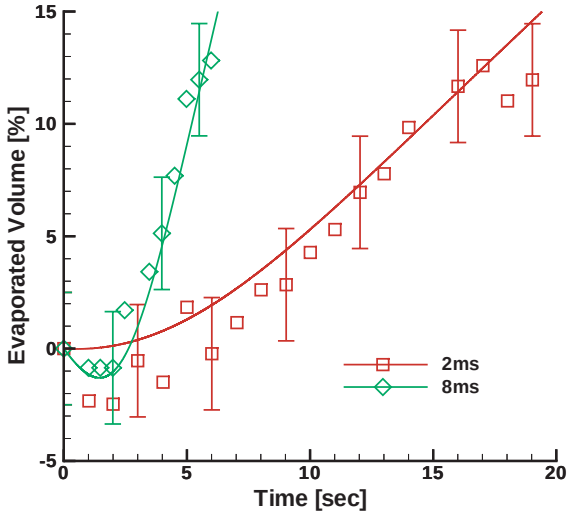

Figure 5.7: Computed and experimental droplet evaporated volume versus time for different laser pulse duration times, at the beginning of evaporation.

where M_l denotes the liquid mass and M_0 denotes the initial liquid mass. The evaporated liquid mass always maintains a positive value, and it is concluded that the initial droplet volume growth is attributable to droplet expansion due to droplet heating, and there is no condensation. Due to the increase of equilibrium temperature with increasing heating pulse duration, thermal expansion is considerably larger for long pulse duration times, and it is hardly visible for the smallest pulse duration time. The values of up to 2.5% of droplet expansion obtained in the experiment at 2 ms agrees with the simulation within the experimental error. A comparison of Figs. 5.4, 5.6 and 5.7 shows that the increase of droplet volume due to droplet heating does not extend the entire droplet heating time. For the longest pulse duration time, the droplet expansion is about 33% of the total droplet heating time, and it decreases for the other cases: 25% for the 8ms situation, 18% for 5ms, and 3% for the shortest laser pulse duration. Figure 5.9 shows that the droplet expansion is a non-linear function of the pulse duration time and it increases with the liquid temperature. The negative peak value of the evaporated volume is also displayed in here, also an almost linear behavior is observed. In summary, the present model for droplet vaporization with laser heating of the droplet in a cold surrounding is suitable to predict the experimental results very well. Therefore, the model is suitable to be used in a broad range of spray combustion systems where dilute sprays predominate the processes.

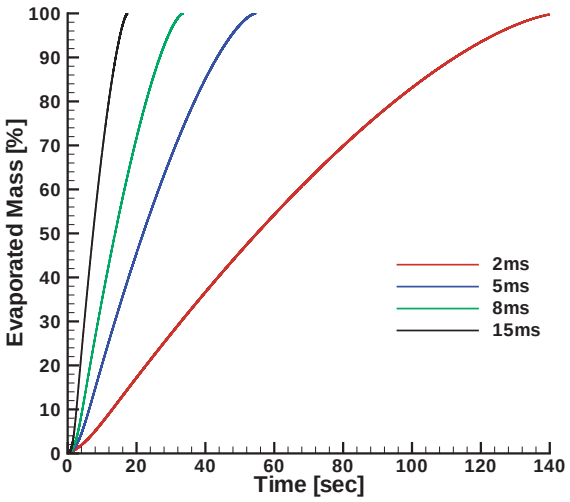

Figure 5.8: Computed droplet evaporated mass versus time for different laser pulse duration times.

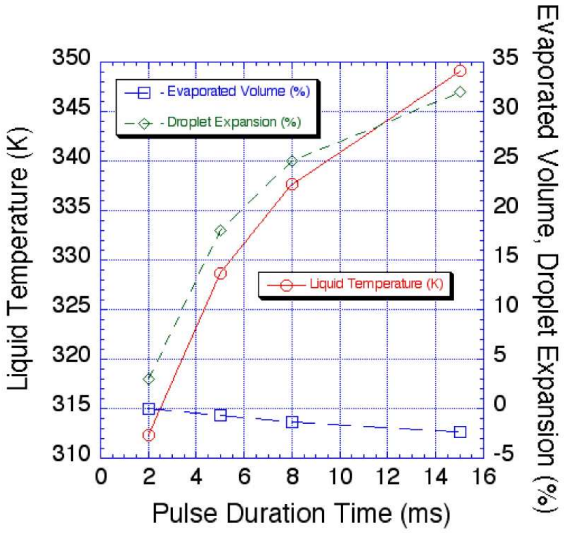

Figure 5.9: Liquid-phase temperature, evaporated volume, and droplet expansion relative to droplet heating time versus pulse duration time.

5.2 Laminar Combustion in the Counterflow Configuration

An axisymmetric counterflow configuration is considered, where either gaseous or liquid fuel versus oxidizer, hot products, and inert gas may be fed from each side of the stagnation plane in any combination [80, 113, 114, 120, 121]. The mathematical model is based on Eulerian/Lagrangian formulation of non-dimensional equations, which are obtained using a similarity transformation by transforming the two-dimensional equations into a one-dimensional system as discussed in detail in subsections 4.2.2 and 4.2.3. The gas-phase model includes a detailed chemical reaction mechanism [1] for CH_4/air, CH_4/O_2 as well as CH_4/LOX, as it is described in subsection 3.3. It consists of 294 elementary reactions among 35 species. The gas phase transport coefficients are computed from NASA polynomials which cover the temperature range between 300 K and 5000 K (see subsection 3.4). Therefore, the set of physical properties must be extended by data from the JSME tables [80] for the temperature range between 80 and 300 K and for pressures up to 20 MPa.

The chemical reaction terms cause the system of conservation equations to be strongly non-linear and stiff. The system of equations is solved using a numerical scheme which is described in 4.2.4. For the solution of the gas phase equations, an adaptive grid is used. The verification of the mathematical model and mechanism is achieved through comparison of the present results for CH_4/air and $CH_4/N_2/O_2$ flames with results from the literature [60, 61].

5.2.1 Gas Diffusion Flames

5.2.1.1 Methane/Air Flames

In this subsection, numerical results for CH_4/air flames are presented and discussed. The pure fuel comes from one side of the counterflow configuration whereas the oxygen/nitrogen mixtures are directed against the fuel stream. In order to validate the mathematical model, the results of the CH_4/air flame are compared with results from the literature [60, 61, 63, 64]. In [60, 61], numerical results for CH_4/air diffusion flame were computed using a detailed starting kinetic mechanism, a reduced 5-step mechanism and a 4-step mechanism. The starting mechanism is a skeletal C_1 mechanism including 39 reactions among 17 species. The strain rates at the fuel side range from 300 s^{-1} to extinction. For the three different mechanisms in [60], namely the starting kinetic mechanism, 5-step and the 4-step mechanisms, the extinction strain rates are 518, 561, and 547 s^{-1} respectively, at standard conditions. The extinction temperature is approximately 1800 K. Du *et. al.* [63] investigated the extinction strain rate for CH_4-N_2-O_2 diffusion flames both numerically and experimentally. Simulations in [63] are based on a 58-step C_1 mechanism and an axisymetric configuration with standard boundary conditions. The numerically obtained extinction strain rate in [63] was 494 s^{-1} and the extinction temperature was 1770 K, while the experimental extinction strain rate was 375 s^{-1}. Other study on CH_4/air flames was done in [64], using an axisymetric counterflow configuration and the GRI 2.11 reaction mechanism including NOx reactions. Using the same boundary conditions as mentioned above, this study led to the extinction strain rate of about 300 s^{-1} and an extinction temperature of about 1700 K. For verification of the model and the chemical reaction scheme, a comparison of a CH_4/air flame at standard conditions and a fuel-side strain rate of 300 s^{-1} is computed. The

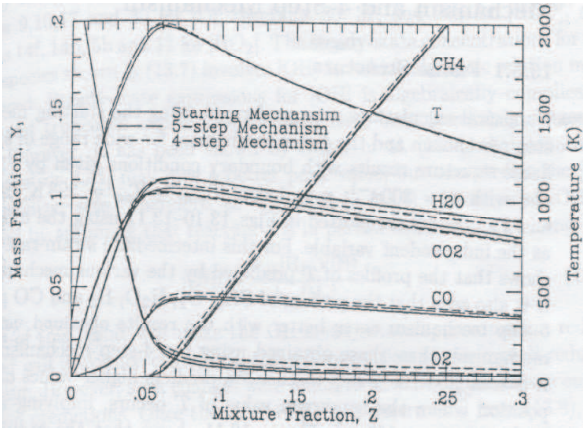

Figure 5.10: Profiles of temperature and major species mass fractions for a CH_4/air flame at standard conditions [60] at a fuel-side strain rate of 300 s^{-1}.

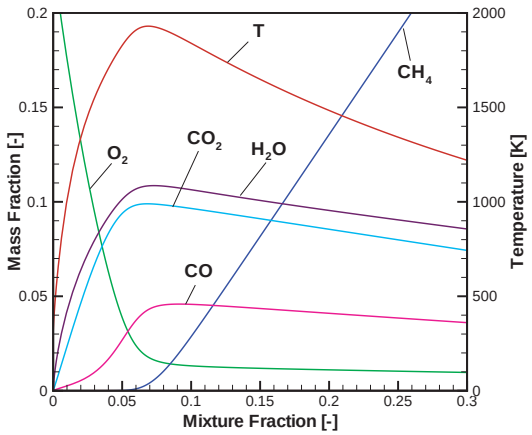

Figure 5.11: Profiles of temperature and mass fractions of major species for a CH_4/air flame at standard conditions for a fuel-side strain rate of 300 s^{-1}.

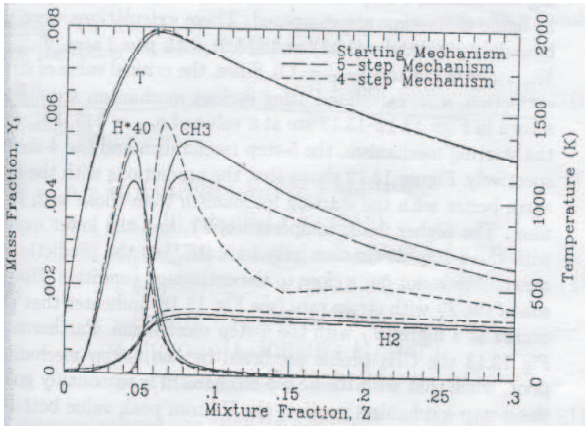

Figure 5.12: Profiles of temperature and minor species mass fractions for a CH_4/air flame at standard conditions [60] at a fuel-side strain rate of 300 s^{-1}.

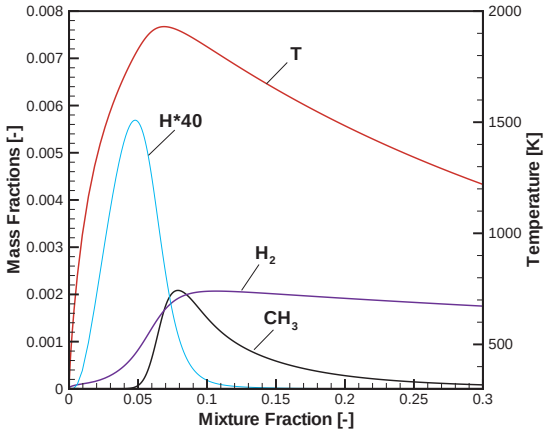

Figure 5.13: Profiles of temperature and mass fractions of minor species for a CH_4/air flame at standard conditions for a fuel-side strain rate of 300 s^{-1}.

comparison of the flame structure in the literature [60], and the present simulations (see Fig. 5.10, 5.11, 5.12, 5.13) shows an excellent agreement. The present simulations yield an extinction strain rate at the fuel side of 380 s^{-1} and the extinction temperature is 1874 K, what leads to a very good agreement especially between present extinction results and experimental extinction results from [60, 63]. The major difference in the models is the employed chemical reaction scheme. The present mechanism includes C_2 reactions [1], which are neglected in Ref. [60, 63, 70]. In stoichiometric CH_4/air flames, the recombination path consumes about 20-30% of the CH_3 radical [1] and therefore the present mechanism includes these reaction rates. Figures 5.11 to 5.13 demonstrate a very good agreement between the present results and the data from the literature. The small discrepancies between the present simulations and the results presented in [60] may be due to the different mechanisms. The C_2 branch typically causes lower extinction temperatures due to the fact that more chemical species are involved leading to a reduced maximum gas temperature because of their energy content.

5.2.1.2 Methane/Oxygen Flames

In this subsection, numerical results for CH_4/O_2 flames are presented and discussed. The pure fuel comes from one side of the counterflow configuration whereas the pure oxygen are injected against the fuel stream.This is achieved through successive replacement of nitrogen by oxygen in the air stream opposing the methane flow. A similar setup has been discussed in [70] for a molar mixture of 68% O_2 and 32% nitrogen. In [70], an extended GRI-Mech 2.11 chemical kinetic mechanism up to C_6 mechanism is used. The conditions used in [70] are standard conditions, and the strain rate on the fuel side of the configuration is 20 s^{-1}. Figure 5.14 shows the present results of the outer flame structure of this configuration using the Warnatz mechanism [1]. They are in very

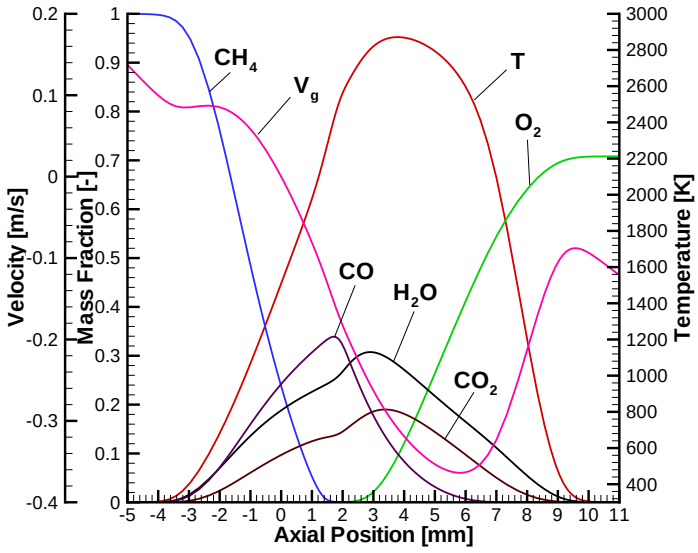

Figure 5.14: Profiles of temperature and mass fractions of CH_4, O_2, H_2O, CO_2 and CO of a $CH_4/O_2/N_2$ flame at a fuel-side strain rate of 20 s^{-1}.

good agreement with the results presented in [70]. For instance, in [70] the peak flame temperature is about 2800 K, peak values of H_2O and H_2 mole fractions are about 0.38 and 0.2 while in the present simulation results the peak flame temperature is 2871 K and the corresponding peak values of H_2O and H_2 are 0.38 and 0.21. Thus, the present model and the chemical mechanism are suitable to predict and coincide with results in the literature. Removal of nitrogen from the air stream was completed so that pure CH_4/O_2 flames are obtained. Figure 5.15 shows the maximum temperature and the mass fractions of thespecies CH_3, CO, O, OH, C_2H_2, C_2H_6, H and CH_2O as a function of the oxygen mass fraction at a strain rate of 100 s^{-1}. The values of oxygen mass fraction range from 0.233 diluted in nitrogen (CH_4/air) to pure O_2. With an increase of oxygen content in the oxidizing gas stream, the maximum flame temperature increases substantially from 1874 K to 2965 K. The maximum mass fraction of the major species plotted in Figure 5.15 increases non-linearly as nitrogen is removed from the system. At the same time, formaldehyde is decreased with nitrogen removal.

The pollutants and soot formation in laminar flames are of particular interest. The detailed chemical reaction mechanism used here is also suitable to predict formation of species such as CO, C_2H_2 as well as CH_2O. Maximum mass fractions of carbon monoxide and acetylene increase by a factor of about 10 as nitrogen is removed (CO increases from 0.043 to 0.46 and C_2H_2 from 0.0078 to 0.075, respectively). The maximum mass fraction of other species such as CH_2O is decreasing as nitrogen is removed, however, the reduction is much smaller.

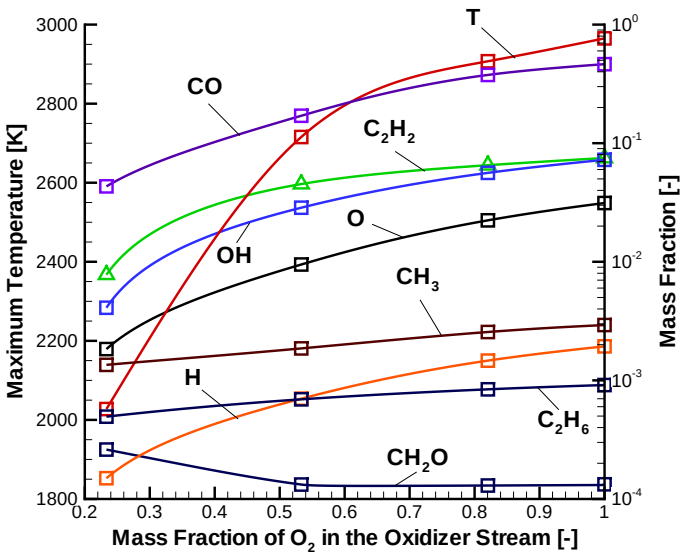

Figure 5.15: Maximum flame temperature and mass fraction of various species with increase of oxygen content in the oxidizing stream at a strain rate of 100 s^{-1}.

In Figs. 5.16 and 5.17, a comparison of the outer flame structure of the CH_4/air (black) and the CH_4/O_2 (red) flames at the strain rates near extinction and standard conditions are shown. The in-figures show an enlarged view of CH_4/O_2 flame for the same conditions. With replacement of nitrogen through oxygen, the flame thickness decreases dramatically by about a factor of seven. This is due to the fact that the damping of chemical reactions by nitrogen is removed with replacement of nitrogen through oxygen leading to enhanced chemical reactions. This enhancement is accompanied by a pronounced increase of flame temperature as shown in the figures. The increase of gas temperature leads to higher values of mass fractions for the major species in the chemical reaction system. In both systems, it can be observed that the flame resides on the oxidizer side of the configuration which is typical for gas flames of this type. For the CH_4/O_2 flame, however, the flame is shifted towards the stagnation plane.

The extinction strain rate for CH_4/air flame is 380 s^{-1}, and the corresponding value for the CH_4/O_2 flame is 46,750 s^{-1} while the extinction temperature of the CH_4/air is 1874 K. The extinction strain rate of CH_4/O_2 at 0.9 MPa is found to be 338,500 s^{-1} with an extinction temperature of 2662K versus 2490 K for the CH_4/O_2 flame at 0.1 MPa. For 2.0 MPa the corresponding values are 667,500 s^{-1} and 2801 K. As extinction is approached, the temperature drop with increased strain is striking, and special attention needs to be paid to evaluate extinction data carefully. Scalar dissipation at stoichiometry decreases with increased strain rate over several orders of magnitude.

The profiles of the main reaction products H_2O, CO_2 and CO as well as the fuel and

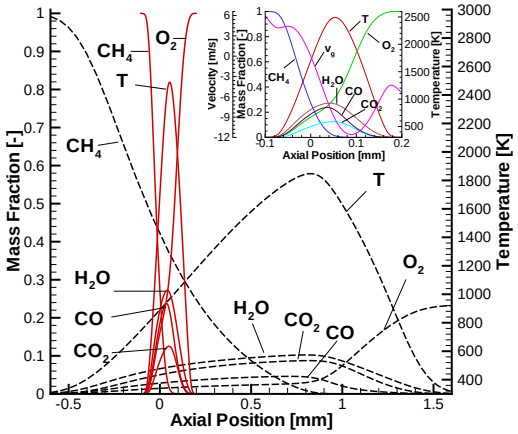

Figure 5.16: Profiles of temperature and mass fractions of CH_4, O_2, H_2O, CO_2 and CO of a CH_4/air (black) and a CH_4/O_2 (red) flame at extinction. Zoomed figure for CH_4/O_2.

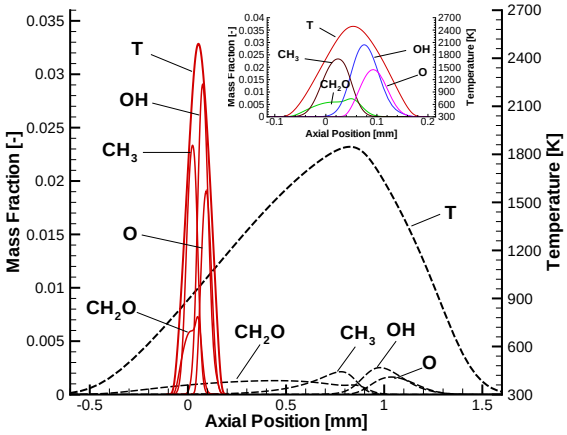

Figure 5.17: Profiles of temperature and mass fractions of CH_3, CH_2O, OH and O for the CH_4/air (black) and the CH_4/O_2 (red) flame at extinction. Zoomed figure of CH_4/O_2.

oxygen are also plotted in Figure 5.16. It can be easily seen that in case the of the CH_4/O_2 flame, all the major species attain higher maximum values of all mass fractions compared to the CH_4/air flame as a consequence of the elevated flame temperature. In the CH_4/O_2 flame, the maximum mass fraction of H_2O is 0.27, that of CO_2 is 0.125, and the maximum mass fraction of CO is 0.237. The corresponding values for the CH_4/air flame are 0.1, 0.087, and 0.045, respectively. Figure 5.17 displays the profiles of the species CH_3, CH_2O, O as well as OH. Oxygen containing species attain their maximum on the oxidizer side of the configuration whereas carbon containing species reach their maximum on the fuel side which is typical for this type of flames. In the case of CH_4/O_2 flame, the maxima of the mass fraction of all the minor species are higher than that in the case of CH_4/air flame. This is due to the fact that the extinction strain rate for CH_4/air flame is much lower than that in the case of CH_4/O_2 flame. High strain rate reduces residence time and thus promotes formation of intermediate species as well as certain pollutants.

Figures 5.18 and 5.19 show the profiles of temperatures, major and minor species respectively, at a strain rate of 100 s^{-1} and pressure of 0.1 and 2 MPa. It can be seen that the temperature is increasing and the flame thickness is becoming narrower with increase of pressure. By increasing the pressure, the molecules are compressed, which reduces the distance between molecules and hence increases the frequency of collisions between them. Compression of the gaseous mixture of air (O_2) and fuel increases the temperature high enough to produce combustion. Thus, increased pressure, results in raising the temperature. This leads to very fast combustion.

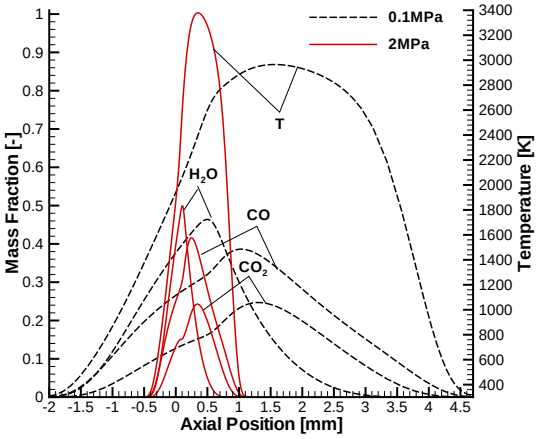

Figure 5.18: Profiles of temperature and of mass fractions of H_2O, CO_2 and CO using CH_4/O_2 laminar flame, at strain rate of 100 s^{-1} and pressures of 0.1MPa and 2MPa.

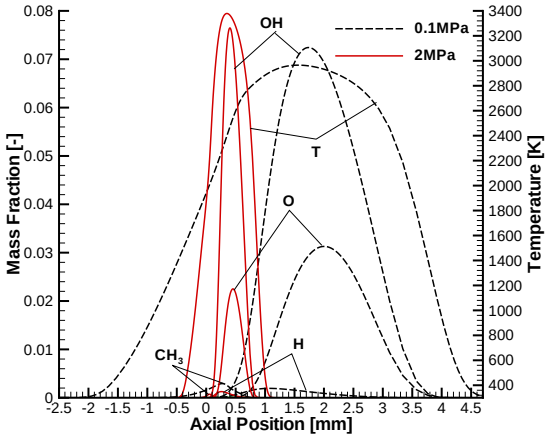

Figure 5.19: Profiles of temperature and of mass fractions of CH_3, CH_2O, OH and O using CH_4/O_2 laminar flame, at strain rate of 100 s^{-1} and pressures of 0.1MPa and 2MPa.

It is because once the reaction has started, heat is produced, which makes it go even faster. The profiles of mass fraction of C_2H_2 for the CH_4/O_2 flame at 2 and 0.9 MPa for different strain rates are shown in Figs. 5.20 and 5.21 respectively. With increased strain rate, the mass fraction of C_2H_2 decreases while that of CH_2O increases, and the narrower profiles are the consequence of the decreased flame thickness resulting from pressure increase. The profile of CH_2O shows a non-monotonic behavior near the maximum flame temperature being a consequence of the stability of this species.

In Fig. 5.22, results of the parametric study that was done to obtain a flamelet library are presented. In flamelet computations, the scalar dissipation rate plays an important role since it is relevant in determination of the regime of extinguished and burning flamelets. The scalar dissipation rate varies with space (and mixture fraction), and typically the flamelet computations include the value of scalar dissipation rate at stoichiometric conditions [105, 122]. Therefore, the figure shows both maximum flame temperature, T, and scalar dissipation rate at stoichiometric conditions. Besides the flames discussed so far, CH_4/O_2 flames at elevated pressures are investigated which are relevant for liquid rocket propulsion applications. In particular, the flames at pressures 0.1, 0.9, and 2 MPa are investigated. For all cases, extinction conditions are determined. It is well known that increased pressure leads to increased flame stability and thus to increased extinction strain rates and temperatures.

Figure 5.23 presents the profiles of mass fraction of C_2H_2 and CH_2O for CH_4/air at 0.1 MPa and CH_4/O_2 at 0.1, 0.9, and 2 MPa, at a fixed value of strain rate, 100 s^{-1}. It can be seen that for CH_4/air at 0.1 MPa, the mass fraction profile of C_2H_2 and CH_2O are broader and the peak is shifted to the oxidizer side in comparison with the CH_4/O_2

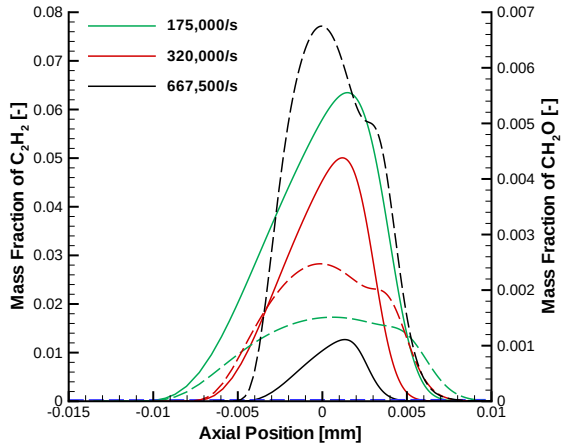

Figure 5.20: Profiles of C_2H_2 (solid line) and CH_2O (dashed line) mass fractions in the CH_4/O_2 flame at 2 MPa and different strain rates.

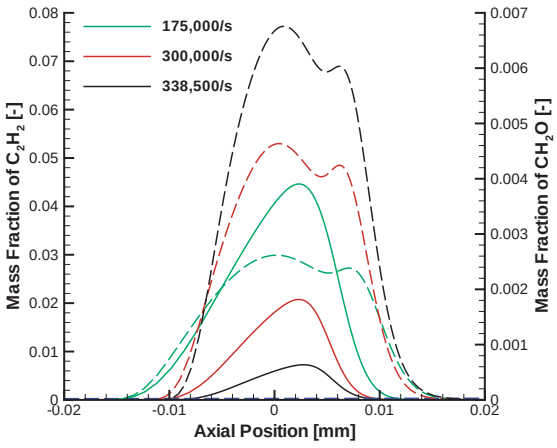

Figure 5.21: Profiles of C_2H_2 (solid line) and CH_2O (dashed line) mass fractions in the CH_4/O_2 flame at 0.9 MPa and different strain rates.

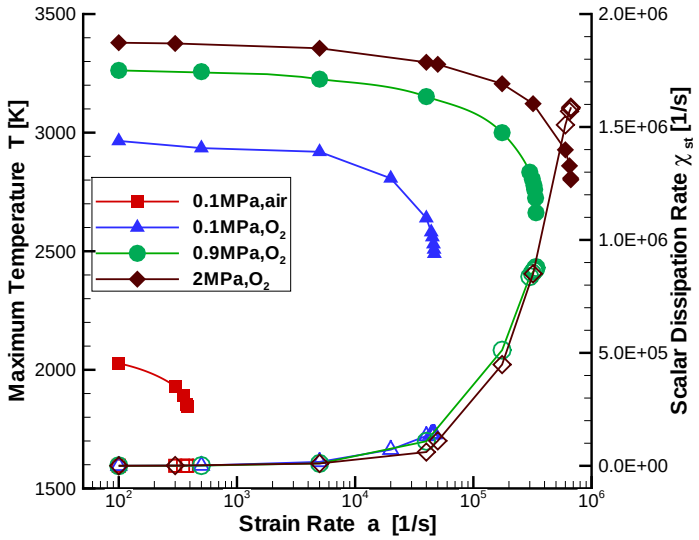

Figure 5.22: Profiles of maximum temperature (filled symbols) and scalar dissipation rate (empty symbols) at strain rates up to extinction.

flame. Pressure increase causes a narrowing of flame thickness and thus a narrower profile of acetylene. For pressures up to 2 MPa for the CH_4/O_2 flame, the maximum

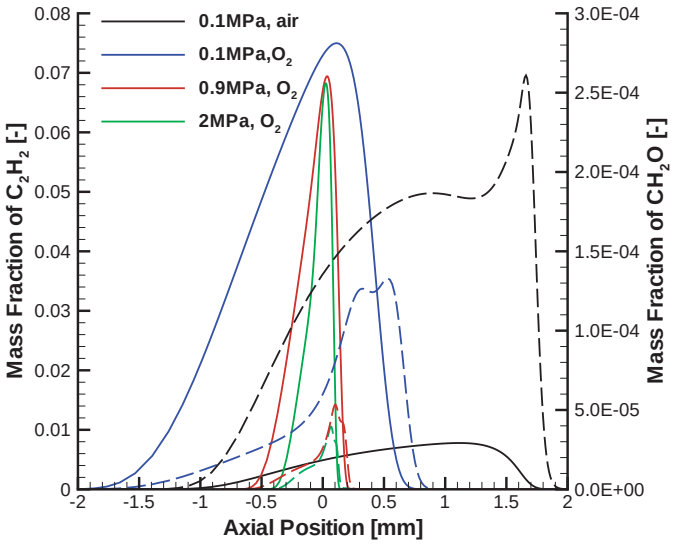

Figure 5.23: Profiles of C_2H_2 and CH_2O mass fraction at different configurations and strain rates of $100s^{-1}$.

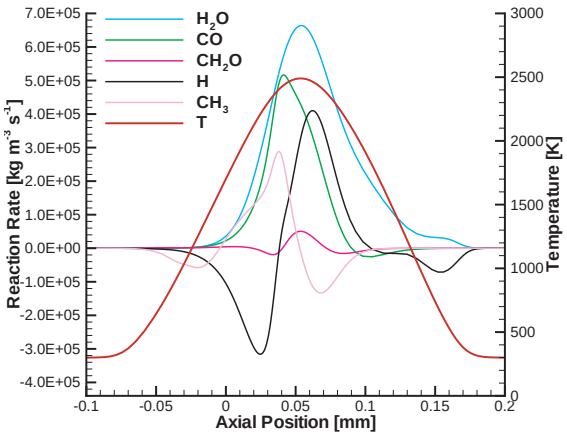

Figure 5.24: Profiles of temperature and reaction rates of H_2O, CH_2O, H, CH_3 and CO using CH_4/O_2 laminar spray flame, at extinction strain rate and pressure of 0.1 MPa.

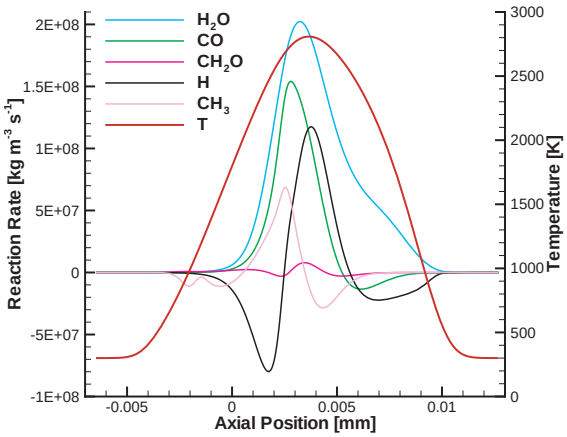

Figure 5.25: Profiles of temperature and reaction rates of H_2O, CH_2O, H, CH_3 and CO using CH_4/O_2 laminar spray flame, at extinction strain rate and pressure of 2 MPa.

mass fraction of C_2H_2 and CH_2O decreases. Here, both nitrogen removal and pressure increase cause lower profiles of formaldehyde.

In Figures 5.24 and 5.25, the profiles of temperature and reaction rates of H_2O, CH_2O,

H, CH_3 and CO using CH_4/O_2 laminar flame, at extinction strain rate and pressures of 0.1 and 2MPa are shown. As it can be seen in the figures 5.24 and 5.25, increasing pressure 20 times, from 0.1 MPa to 2 MPa, reaction rates are increased by 3 orders of magnitude but this does not effect the shape of reaction rates of species. Moreover, it causes temperature to increase by 16.67 % and flame thickness to decrease by more than 15 times.

5.2.2 Spray Flames

5.2.2.1 Methane/LOX Flames

In the present subsection, numerical results for CH_4/LOX spray flames are presented and discussed. A stream of monodisperse LOX droplets with carrier gas methane is directed from one side of the counterflow configuration whereas the pure oxygen is injected against the fuel stream. The initial droplet velocity equals the methane velocity, $v_{g0} = v_{l0} = 0.49$ m/s, and together with the strain rate on this side of the configuration, the velocity of the oxygen is determined from the computation. All present results are for atmospheric pressure and initial LOX temperature of 85K and methane temperature of 300K. The results show variation of initial droplet radius for fixed strain rate.

Figures 5.26, 5.27 and 5.28 show the comparison of the outer flame structure of CH_4/LOX spray flames for three different initial droplet radius of 15, 25, 35 µm, respectively, at a strain rate of 100 s^{-1} at the fuel side of the configuration.

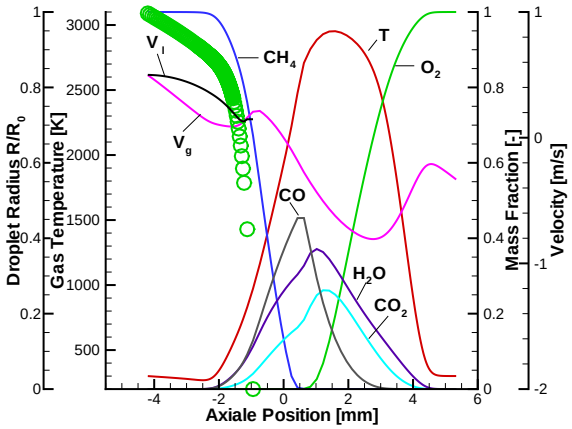

Figure 5.26: Profiles of gas temperature and H_2O, CO_2 and CO mass fractions in the LOX/CH_4 spray flame, at strain rate 100 s^{-1}, and pressure of 0.1 MPa, initial droplet radius 15 µm.

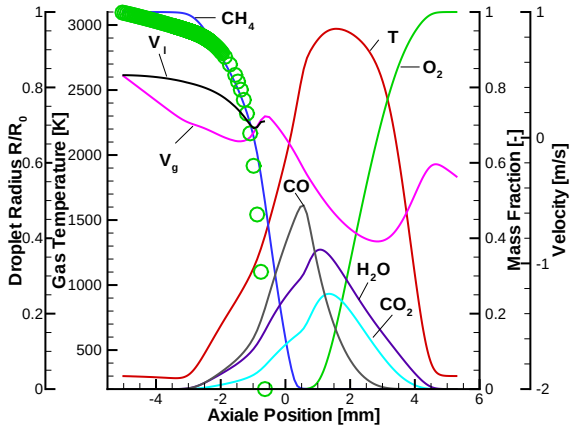

Figure 5.27: Profiles of gas temperature and H_2O, CO_2 and CO mass fractions in the LOX/CH_4 spray flame, at strain rate 100 s^{-1}, and pressure of 0.1 MPa, initial droplet radius 25µm.

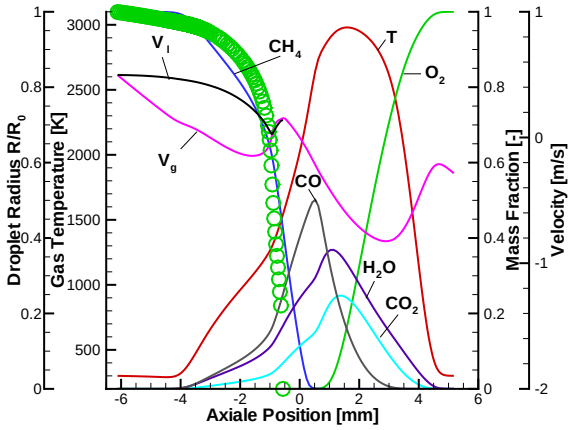

Figure 5.28: Profiles of gas temperature and H_2O, CO_2 and CO mass fractions in the LOX/CH_4 spray flame, at strain rate 100 s^{-1}, and pressure of 0.1 MPa, initial droplet radius 35 µm.

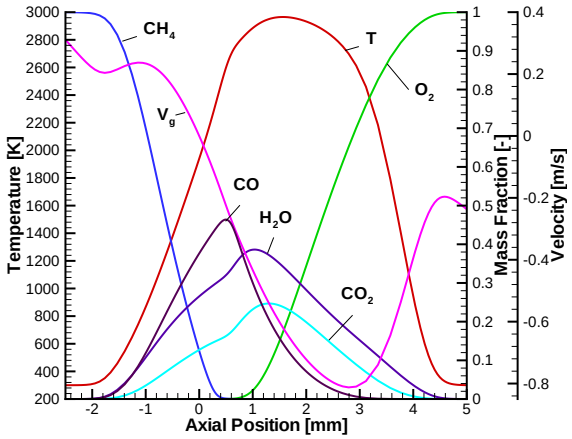

Figure 5.29: Profiles of gas temperature and H_2O, CO_2 and CO mass fractions in the CH_4/O_2 laminar flame, at strain rate 100 s^{-1}, and pressure of 0.1 MPa.

The droplets vaporize completely before they reach the stagnation plane at axial position zero. However, they move closer to the stagnation plane as initial droplet radius is increased. The present computations do not show droplets crossing the stagnation plane and no droplet reversal is seen due to the small strain rate, which is typical for spray flames in the counterflow configuration [114, 120, 121]. The flame resides on the oxidizer side of the configuration, and the spray flame broadens with increased initial droplet size. Larger droplet size also increases drag which can be seen from the velocity profiles of the gas and the droplets. As droplets vaporize, drag is reduced and small droplets eventually follow the gas velocity. As initial droplet size is increased, the gas temperature is pronouncedly affected by evaporation causing an increased dip in the left wing of the temperature profile. The maximum flame temperature increases by 30 K as initial droplet radius is increased from 15 to 35 µm. Considering the gas-phase species, it is observed that profiles of both major and minor species are quite close for different initial droplet sizes.

Principal flame characteristics such as CO formation prior to CO_2 formation are maintained. Carbon monoxide is produced and then consumed at high temperatures in the rate-limiting reaction $CO + OH \rightleftharpoons CO_2 + H$.

A comparison of the LOX/CH_4 spray flame and the CH_4/O_2 flame, see Fig. 5.29, shows that in both configurations, the main reaction zone resides on the gas side of the counterflow configuration and the principal flame structure is almost similar. At the same time, the presence of the spray strongly influences the gas temperature in regions where the spray is present. Moreover, the presence of the spray causes considerable

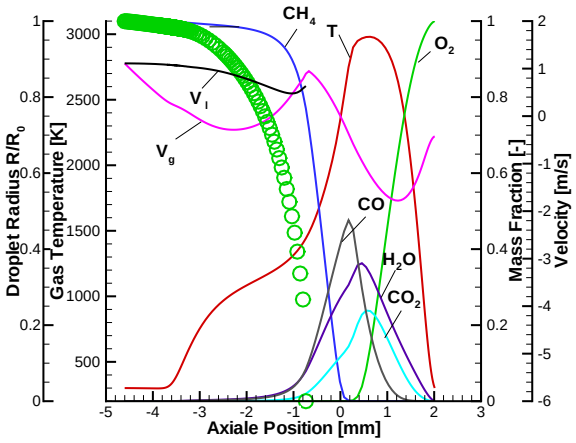

Figure 5.30: Gas temperature and major species mass fractions of CH_4/LOX flame, strain rate 500 s^{-1}, $p = 0.1$ MPa, $r_{l0} = 25$ µm.

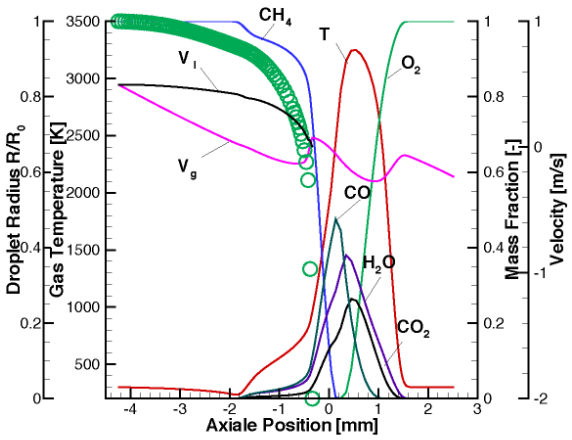

Figure 5.31: Profiles of gas temperature and major species mass fractions of CH_4/LOX spray flame, at pressure 0.9 MPa, initial droplet radius 25 µm.

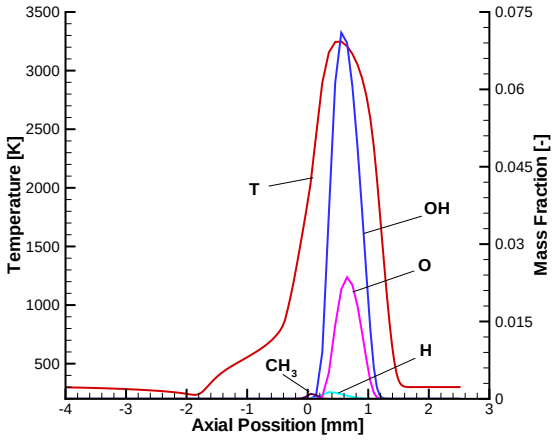

Figure 5.32: Profiles of gas temperature and minor species mass fractions of CH_4/LOX spray flame, at pressure 0.9 MPa, initial droplet radius 25 µm.

broadening of the reaction zone.

An increase of strain rate from 100 to 500 s^{-1} at fixed initial droplet size of 25 µm, the flame becomes thinner and the effect of droplet vaporization on the temperature profile is evident. A comparison of Fig. 5.30 and Fig. 5.27 shows that the flame becomes thinner with increased strain rate, and the cooling effect due to droplet vaporization is

dominant.

Figures 5.31 and 5.32 show the structure of major and minor species of the CH_4/LOX spray flame at a pressure of 0.9 MPa. The pressure increase at cryogenic conditions is shown in Figure 5.31, where the flame structure is considerably narrow and the combustion is enhanced when compared with the results at atmospheric pressure.

It is interesting to note that in methane/LOX flames, so far, only single flames are found whereas in both H_2/LOX [80] flames and during combustion of fuel sprays in air [113, 114, 120, 121], double flames where identified for small strain rates below about 500 s^{-1}. However, in [121], two different flame structures were identified with one and two reaction zones, for spray flames at low strain.

6 Summary and Conclusions

In the present work, laminar models for CH_4/air, CH_4/O_2 and CH_4/LOX -spray flames as well as single droplet vaporization by laser heating are investigated numerically. Initially, an overview of the basic equations of gas and liquid phase and the models for transport processes are presented. The detailed kinetics were described separately. Then the simulation results are discussed. The main findings are summarized in the following.

It is known that droplet vaporization is the basic process in spray combustion. In the first part of present work, a mathematical model for water droplet vaporization with laser heating of the droplet in a cold surrounding was developed and validated through comparison with the experimental results. A uniform temperature field inside the droplet was assumed during the vaporization process of the droplet by laser heating. The physical properties of the vaporizing droplet were adapted to water. Four different laser pulse widths were used, namely 2 ms, 5 ms, 8 ms, and 15 ms, and the simulation results [29] predict the experimental results very well [28]. Therefore, the model is suitable to be used in a broad range of spray combustion systems where dilute sprays predominate the processes.

Initially, the mathematical model for counterflow configuration was used and validated for other fuels such as methanol/air, ethanol/air and H_2/LOX (see [80, 114, 120, 121]). Therefore, in the second part of present work, the mathematical model has been tested with different chemical kinetic mechanism and successfully validated through comparison of calculated temperature and concentration profiles of a CH_4/air gas diffusion flame in counterflow configuration with data of [60]. The C_2 kinetic mechanism was used involving 35 species and 294 reactions whilst in literature [60] the starting C_1 mechanism of 39 reactions involving 17 species, a 5-step mechanism and a 4-step mechanism was used.

After validation of the models for CH_4/air-gas diffusion flames, simulations of CH_4/O_2 flames at pressures of 0.1 MPa, 0.9 MPa and 2 MPa were performed. The conditions used in the simulations of CH_4/O_2 flames are: the temperature at both boundaries is 298 K, the mass fractions of fuel and oxygen is 1. So, with increasing the oxygen quantity and removing the nitrogen, the high temperature region is becoming broader compared to the CH_4/air flame and the combustion is enhanced significantly. It can be also observed that the maximum temperature and stagnation plane of CH_4/O_2 flame is shifted toward the fuel side in comparison with CH_4/air flame. The extinction strain rate at 0.1 MPa for CH4/air flame is about 380 s^{-1} and for CH_4/O_2 flame is about 46,500 s^{-1} while the peak temperatures near extinction for CH_4/air and CH_4/O_2 are about 1800 K and 2507 K respectively. Thus, with increasing pressure, the flame becomes thinner and the peak

temperature becomes higher. The extinction strain rate for CH_4/O_2 flame at 0.9 MPa is about 3,385,00 s^{-1} and at 2 MPa is about 667,500 s^{-1} while the peak temperatures near extinction at 0.9 MPa and 2 MPa are about 2663 K and 2802 K respectively. Objectives were, first, determining the extinction conditions and second, to be used as a gas flame library in turbulent calculations.

The pollutants and soot formation in laminar flames are of particular interest. The detailed chemical reaction mechanism used here is favorably enabled to predict formation of species such as CO, C_2H_2 as well as CH_2O. Maximum mass fraction of carbon monoxide and acetylene increase by a factor of about 10 as nitrogen is removed. This increase of acetylene formation with oxygen content confirms the results of [70] who found soot formation to increase with oxygen content, since acetylene is considered an important soot precursor.

The next step, the laminar flame structure of CH_4/LOX in counterflow configuration depending on the parameters like equivalence ratio, strain rate and droplet size was systematically investigated for monodisperse spray at atmospheric pressure. Since the boiling temperature for oxygen is around 90 K depending on pressure, so in our computations, the initial LOX temperature is set at 85 K in order to catch the liquid phase of oxygen. The physical properties for methane and oxygen above 300 K are covered by the NASA data. Therefore, the set of physical properties must be extended by data from the JSME tables [103] for the temperature range between 80 and 300 K and for pressures up to 2 MPa. Moreover, increased initial droplet size broadens the spray flame considerably.

The present simulations at low strain rate do not reveal droplets crossing the stagnation plane or droplet oscillations which is typical for spray flames at elevated strain rates. Double flames which are found in both the H_2/LOX system and in fuel sprays burning in air could not be identified in the present study, which can be studied further in prospective research.

Overall, it can be concluded that the calculation of spray flames can not be made with models of pure gas flame, as the spray characteristics such as evaporation, heating of the liquid and spray dynamics influence the mathematical modeling significantly. Using detailed chemical reaction mechanisms is essential for the calculation of pollutant formation and extinction conditions in laminar flames.

Future studies will investigate if the occurrance of a single flame is a principal characteristics of methane/LOX flames or if different structures [121] may be found besides the low-strain structures with a single reaction zone shown in the present work.

Further computations will include methane/LOX flames at elevated strain where the spray has an increased effect on both the flame structure and extinction conditions due to droplets crossing the stagnation plane and droplet reversal and oscillation. Moreover, extinction conditions need to be identified for the establishment of a spray flamelet library. Additionally, structures at elevated pressures which characterize liquid rocket propulsion will be investigated for use in turbulent spray computations either through spray flamelet models or flamelet generated manifolds.

List of Symbols

Symbol	Meaning	Units
a	Strain rate	$1/\mathrm{s}$
A_j	Pre-exponential factor in chemical reaction j	m,mol,s
b_j	Temperature exponent in chemical reaction j	-
B_M	Spalding transfer number for mass	-
B_T	Spalding transfer number for heat	-
C_p	Specifc heat at constant pressure	$\frac{\mathrm{J}}{\mathrm{kg\,K}}$
$\overline{c_p}$	Specific heat at constant pressure of mixture	$\frac{\mathrm{J}}{\mathrm{kg\,K}}$
C_v	Specific heat at constant volume	$\frac{\mathrm{J}}{\mathrm{kg\,K}}$
C_D	Drag coefficient	-
D_i	Diffusion coefficient of species i	$\frac{\mathrm{m}^2}{\mathrm{s}_2}$
$D_{i,j}$	Binary diffusion coefficient of species i and j	$\frac{\mathrm{m}^2}{\mathrm{s}_2}$
D_i^T	Thermal diffusion coefficient of species i	$\frac{\mathrm{m}^2}{\mathrm{s}}$
D_a	Damkohler number	-
$\overline{\overline{E}}$	Unit matrix	-
E_j	Actvition energy of the elementary reaction j	$\frac{\mathrm{J}}{\mathrm{mol}}$
F_M	Correction factor for the film thickness of diffusive flux	-
F_T	Correction factor for the film thickness of thermal flux	-
f	Similarity variable	-
f_i	Fugacity of component i	Pa
f_p	Droplet size distribution	-
$\vec{g}$	Vector of gravitational accelaration	$\frac{\mathrm{m}}{\mathrm{s}^2}$
G	Gravity potential	$\frac{\mathrm{m}^2}{\mathrm{s}^2}$
h	Specific enthalpy	$\frac{\mathrm{J}}{\mathrm{kg}}$
$\vec{j_i}$	Mass flux by molecular diffusion of species i	$\frac{\mathrm{kg}}{\mathrm{m}^2\,\mathrm{s}}$
$\vec{j_i^T}$	Mass flux by thermal diffusion of species i	$\frac{\mathrm{kg}}{\mathrm{m}^2\,\mathrm{s}}$

Symbol	Meaning	Units
$\vec{j_e}$	Energy flux by diffusion and heat conduction	$\frac{\mathrm{J}}{\mathrm{m^2\,s}}$
$\vec{j_e^c}$	Energy flux by heat conduction	$\frac{\mathrm{J}}{\mathrm{m^2\,s}}$
$\vec{j_e^d}$	Energy flux by diffusion	$\frac{\mathrm{J}}{\mathrm{m^2\,s}}$
$\vec{j_e^D}$	Energy flux by concentration gradient	$\frac{\mathrm{J}}{\mathrm{m^2\,s}}$
k_j	Rate constant of reaction j	$\frac{\mathrm{m^3}}{\mathrm{mol\,s}}$
K	Number of chemical components	-
l_t	intergral length scale	m
L_v	Latent heat of vaporization	$\frac{\mathrm{J}}{\mathrm{kg}}$
Le	Lewis number	-
m	mass	kg
$\dot{m}$	Vaporization rate	$\frac{\mathrm{kg}}{\mathrm{s}}$
m_i	mass of species i	kg
m_l	mass of a droplet	kg
Ma	Mach number	-
N	Number of chemical reaction	-
N_p	Number of droplets	-
n	Droplet number density	$\mathrm{m^{-3}}$
Nu_0	Nusselt number without Stefan-Flow	-
$\widetilde{Nu}$	Modified Nusselt number	-
p	Pressure	Pa
p_c	Critical pressure	Pa
p_s	Vapor pressure	Pa
$\overline{\overline{p}}$	Pressure tensor	Pa
P_r	Prandtl number	-
q	Specific heat	$\frac{\mathrm{J}}{\mathrm{kg}}$
$\dot{q}$	Heat flux	$\frac{\mathrm{J}}{\mathrm{s}}$
q_m	Phase exchange term in continuity equation	$\frac{\mathrm{kg}}{\mathrm{m^3\,s}}$
q_{m_i}	Phase exchange term in species conservation equation	$\frac{\mathrm{kg}}{\mathrm{m^3\,s}}$
$\vec{q}_p$	Phase exchange term in momentum equation	$\frac{\mathrm{kg}}{\mathrm{m^3\,s^2}}$
$q_{p,x}$	x- component of Phase exchage term in momentum equation	$\frac{\mathrm{kg}}{\mathrm{m^2\,s^2}}$
$q_{p,y}$	y- component of Phase exchage term in momentum equation	$\frac{\mathrm{kg}}{\mathrm{m^2\,s^2}}$

Symbol	Meaning	Units
q_e	Source term of phase exchange for the specific total energy	$\frac{\mathrm{J}}{\mathrm{m}^3\,\mathrm{s}}$
q_T	Source term of phase exchange for the temperature	$\frac{\mathrm{J}}{\mathrm{m}^3\,\mathrm{s}}$
q_h	Source term of phase exchange for the enthalpy	$\frac{\mathrm{J}}{\mathrm{m}^3\,\mathrm{s}}$
r	Radial coordinate	m
R	Droplet radius	m
R_0	Droplet radius at $t = 0$	m
R	Gas constant	$\frac{\mathrm{J}}{\mathrm{mol\ K}}$
$\vec{r}$	Local vector	m
Re	Reynolds number	-
Sh_0	Sherwood number without Stefan-Flow	-
$\widetilde{Sh}$	Modified Sherwood number	-
Sc	Schmidt number	-
s	Transformed radial local coordinate of a droplet	-
T	Temperature	K
T_l	Temperature in a droplet	K
T_s	Surface temperature of a droplet	K
t	Time	s
t_c	chemical time scale	s
u	Velocity component	$\frac{\mathrm{m}}{\mathrm{s}}$
u_l	Radial component of drop velocity	$\frac{\mathrm{m}}{\mathrm{s}}$
u_in	Specific internal energy	$\frac{\mathrm{J}}{\mathrm{kg}}$
V	Volume	m^3
v	Velocity component	$\frac{\mathrm{m}}{\mathrm{s}}$
$\vec{V_i}$	Diffusional velocity of species i	$\frac{\mathrm{m}}{\mathrm{s}}$
$\vec{V_{i,y}}$	Diffusional velocity of species i in y - direction	$\frac{\mathrm{m}}{\mathrm{s}}$
$\overline{W}$	Molecular weight of gas mixture	$\frac{\mathrm{kg}}{\mathrm{mol}}$
W_i	Molecular weight of the species i	$\frac{\mathrm{kg}}{\mathrm{mol}}$
W_e	Weber number	-
x	Radial local coordinate	m
x_l	Radial local coordinate of a droplet	-
X_i	Mole fraction of species ı	-
Y_i	Mass fraction of species i	-

Symbol	Meaning	Units
y	Axial space coordinate	m
y_l	Axial space coordinate of a droplet	-
Z	Compressibilty factor	-

Greek symbols

Symbol	Meaning	Units
α	Planar/axisymetric counterflow configuration	-
α_l	Thermal diffusivity	-
$\delta_{i,s}$	Kronecker delta	-
δ_M	Film thickness due to diffusion exchange with Stefan flow	m
δ_T	Film thickness due to thermal exchange with Stefan flow	m
δ_{M0}	Film thickness due to diffusion exchange without Stefan flow	m
δ_{T0}	Film thickness due to thermal exchange without Stefan flow	m
η	Similarity independent variable	-
η_l	Dimensionless axial position of a droplet	-
λ	Heat conductivity	$\frac{\mathrm{J}}{\mathrm{m\,s\,K}}$
$\bar{\lambda}$	Heat conductivity of a mixture	$\frac{\mathrm{J}}{\mathrm{m\,s\,K}}$
μ	Dynamic viscosity	$\frac{\mathrm{kg}}{\mathrm{m\,s}}$
$\nu'_{i,j}$	Stoichiometric coefficient, educt	-
$\nu''_{i,j}$	Stoichiometric coefficient, products	-
ν	Kinematic viscosity	$\frac{\mathrm{m}^2}{\mathrm{s}}$
ξ	Dimensionless radial coordinate	-
ξ_s	Dimensionless droplet radius	-
τ	Dimensionless time	-
Φ	Extensive variable	-
χ	Scalar dissipation rate	$\frac{1}{\mathrm{s}}$
$\dot{\omega}_i$	Source term due to chemical reactions	$\frac{\mathrm{mol}}{\mathrm{s}}$
ω_{CV}	Control volume	-

Bibliography

[1] J. Warnatz, U. Maas, R.W. Dibble. *Combustion, Physical and Chemical fundamentals, Modeling and Simulation, Experiments, Pollutant Formation.* Springer-Verlag, Berlin Heidelberg, New York, 2nd Edition, (1999).

[2] D.H. Brouwer, S. Semple, J. Marquart, J.W. Cherrie. A Dermal Model for Spray Painters. *Ann. Occup. Hyg.* **45**, 15–23 (2001).

[3] F. Lebeau. Modelling the Dynamic Distribution of Spray Deposits. *Biosystems Eng.* **89**, 255–265 (2004).

[4] D. Nuyttens, K. Baetens, M. De Schampheleire, B. Sonck. PDPA Laser Based Characterisation of Agricultural Sprays. *Agric. Eng. Int.: the CIGR Ejournal* **8**, 03–024 (2006).

[5] W.A. Taylor, A. R. Womac, P. C. H. Miller, B. P. Taylor. An Attempt to Relate Drop Size to Drift Risk. *Proceedings of the International Conference on Pesticide Application for Drift Management*, 210–233 (2004).

[6] O. Permin, L. N. Jrgensen, P. Persson. Deposition Characteristics and Biological Effectiveness of Fungicides Applied to Winter Wheat and the Hazards of Drift when Using Different Types of Hydraulic Nozzles. *Crop Protection* **11**, 541–546 (1992).

[7] R. N. Klein, A.K. Johnson. Nozzle Tip Selection and its Effect on Drift and Efficacy. *Aspects of Applied Biology, International Advances in Pesticide Application* **66**, 217–224 (2002).

[8] P.C.H. Miller, M. C. Butler Ellis. Effects of Formulation on Spray Nozzle Performance for Applications from Ground-Based Boom Sprayers. *Crop Protection* **19**, 609–615 (2000).

[9] D. Pochi, D. Vannucci. *Prediction of Pesticide Distribution on the Ground Based on Sprayer Boom Movements. Agric. Eng. Int.: the CIGRE Journal* **4**, (2002).

[10] L. Fan, R.D. Reitz. Spray and Combustion Modeling in Gasoline Direct-Injection Engines. *Atomization Spray* **10(3–5)**, 318 (2000).

[11] R. Rotondi, G. Bella. Gasoline Direct Injection Spray Simulation. *Int. J. Therm. Sci.* **45(2)**, 168–179 (2006).

[12] D.M. Probst, J.B. Ghandhi. An Experimental Study of Spray Mixing in a Direct Injection Engine. *Int. J. Engine Res.* **4(1)**, 27–45 (2003).

[13] P.B. Paul, M. Sichel, J.A. Nicholls. Analysis of Spray Combustion in a Research Gas Turbine Combustor. *Combust. Sci. Tech.* **17(1–2)**, 21–31 (1978).

[14] A.H. Lefebvre, D.R. Ballal. *Gas Turbine Combustion.* Lawrence Erlbaum, New York, 3rd edition Edition, (2010).

[15] M. Zaller, R.J. Locke, R.C. Anderson. Comparison of Techniques for Non-intrusive Fuel Drop Size Measurements in a Subscale Gas Turbine Combustor. *J. Vizualization* **2(3–4)**, 301–308 (1999).

[16] V. Schmidt, J. Sender, M. Oschwald. Simultaneous Observation of Liquid Phase Distribution and Flame Front Evolution during the Ignition Transient of a LOx/GH_2 Combustor. *J. Vizualization* **4(4)**, 365–372 (2001).

[17] H. Ellerbrock, S. Ziegenhagen. Liquid Rocket Engine Test Facility Engineering Challenges. *Acta Astronaut.* **59(12)**, 1123–1134 (2006).

[18] W.O.H. Mayer. Cryogenic Rocket Engine Research within the National Technology Program TEKAN at the German Aerospace Center. *Aerosp. Sci. Tech.* **5(4)**, 273–282 (2006).

[19] J. Warnatz, U. Maas, R.W. Dibble. *Combustion, Physical and Chemical Fundamentals, Modeling and Simulation, Experiments, Pollutant Formation.* Springer-Verlag, Berlin Heidelberg, New York, 4th Edition, (2006).

[20] S. Zurbach, J.L. Thomas, P. Vuillermoz, L. Vingert, M. Habiballah. Recent Advances on LOX/CH_4 Combustion for Liquid Rocket Engine Injector. *AIAA* **38**, (2002).

[21] S. Zurbach, J.L. Thomas, C. Verplancke, L. Vingert, M. Habiballah. LO2/Methane Studies for Fuel Rich Preburner. *AIAA* **39**, (2003).

[22] S. Zurbach, J.L. Thomas, C. Verplancke, L. Vingert, M. Habiballah. LOX/Methane studies for fuel rich preburner. *AIAA* **2003–5063**, (2003).

[23] F. Cuoco, B. Yang, C. Bruno, O.J. Haidn, M. Oschwald. Experimental Investigation on LOx/CH_4 Ignition. *AIAA* **40**, (2004).

[24] C Pauly. *Laser Ignition of Gaseous CH_4/O_2 Coaxial Jet.* Phd thesis, DLR, Lampoldshausen, (2006).

[25] F. Cuoco, B. Yang, M. Oschwald. Experimental Investigation of LOx/H_2 and LOx/CH_4 Coaxial Sprays and Flames. *ISTS* **24**, (2004).

[26] G. Coppola, B. Coriton, A. Gomez. Highly Turbulent Counterflow Flames: A laboratory Scale Benchmark for Practical Systems. *Combust. Flame* **156(9)**, 1834–1843 (2009).

[27] H. Bongers, J.A. Van Oijen, L.M.T. Somers, L.P.H. De Goey. The Flamelet Generated Manifold Method Applied to Steady Planar Partially Premixed Counteflow Flames. *Combust. Sci. Tech.* **177(12)**, 2373–2393 (2005).

[28] I. Düwel, J. Schorr, J. Wolfrum, C. Schulz. Laser Induced Fluorescence of Tracers Dissolved in Evaporating Droplets. *Appl. Phys. B*, (2003).

[29] D. Urzica, I. Düwel, C. Schulz, E. Gutheil. Laser Induced Evaporation of Single Droplets - An Experimental and Computational Investigation. *ILASS Europe (20th Anual Conference on Liquid Atomization and Spray Systems)*, (2005).

[30] *CTR Carinthian Tech Research AG, Europastrae 4/1A-9524, Villach/St. Magdalen, Austria.* http://www.ctr.at/carinthian_tech_research_deutsch, (2005).

[31] J. Graf. *Investigation on Laser-induced Ignition of an Otto Direct Injection Engine of the 2nd Generation.* Master thesis, University of Technology, Vienna, (2002).

[32] M. Lackner, F. Winter, J. Graf, B. Geringer, M. Weinrotter, H. Kopecek, E. Winter, J. Klausner, G. Herdin. Laser Ignition in Internal Combustion Engines-A contribution to a Sustainalble enviroment. *IFRF, 14th Members Conference, International Flame Research Fundation, Nordwijkerhont, Netherlands*, 2004 (2004).

[33] A. Müsing, U. Riedel, J. Warnatz, W. Herden, H. Ridderbusch. *Laser-Induced Breakdown in Air and Behind Droplets: a Detailed Monte-Carlo Simulation.* Proc. Combust. Inst. **31**, 3007–3014 (2006).

[34] R. L. Armstrong. Aerosol Heating and Vaporization by Pulsed Light Beams. *Appl. Opt.* **23**, 148–155 (1984).

[35] R.L. Armstrong, P.J. Orourke, A. Zardecki. Vaporization of Irradiated Droplets. *Phys. Fluids* **29**, 3573–3577 (1986).

[36] R. L. Armstrong, A. Zardecki. Diffusive and Convective Vaporization of Irradiated Droplets. *Appl. Phys.* **62**, 4571–4578 (1987).

[37] A. N. Kucherov. Sublimation and Vaporization of an Ice Aerosol Particle in the Form of Thin Cylinder by Laser Radiation. *Int. J. Heat Mass Transfer* **43**, 2793–2806 (2000).

[38] H. Zhang. Evaporation of a Suspended Droplet in Forced Convective High-pressure Environments. *Combust. Sci. Tech.* **175**, 2237–2268 (2003).

[39] J.R. Yang, S.C. Wong. An Experimental and Theoretical Study of the Effects of Heat Conduction through the Support Fiber on the Evaporation of a Droplet in a Weakly Convective Flow. *Int. J. Heat Mass Transf.* **45**, 4589–4598 (2002).

[40] W. A. Sirignano. *Fluid Dynamics and Tansport of Droplets and Sprays*. Cambrigde University Press, (1999).

[41] H.W. Ge, D. Urzica, M. Vogelgesang, E. Gutheil. *Modeling and Simulation of Turbulent Nonreacting and Reacting Spray Flows*. Springer, (2006).

[42] I. Düwel. *Beobachtung der laserinduzierten Einzeltropfenvardampfung mit Hilfe der laserinduzierten Fluoreszenz*. Diplom thesis, Universität Heidelberg, (2003).

[43] J.D. Clark. *Ignition! An Informal History of Liquid Rocket Propellants*. Rutgers University Press, (1972).

[44] H. Burkhardt, M. Sippel, J. Klevanski, A. Herbertz. Comparative Study of Kerosene and Methane Propellants for Reusable Liquid Booster stages. *AIAA-2002-5235*, (2002).

[45] P.A. Masters, E.S. Armstrong, H.G. Price. High Pressure Calorimeter Chamber Tests for Liquid Oxygen/Kerosene (LOx/RP-1) Rocket Combustion. *Technical Report NASA, Cleveland, USA*, (1998).

[46] J. Yu, C. Lee. Prediction of Non-equilibrium Kinetics of Fuel-Rich Kerosene/LOX Combustion in Gas Generator. *J. Mech. Sci. Technol.* **21(8)**, 1271–1283 (2007).

[47] *Non-toxic OMS/RCS for Space Shuttle*. http:// spaceflight.nasa.gov/ shuttle/upgrades/ ntoms.html, (2002).

[48] D. Haeseler, G. Langel, T. Froehlich. Use of Non-toxic Propellants for Launcher Propulsion Systems. *EAC-99-71*, (1999).

[49] *Encyclopedia Astronautica*. http://www.astronautix.com, (2002).

[50] I.A. Klepikov, B.I. Katorgin, V.K. Chvanov. The New Generation of Rocket Engines, Operating by Ecologically Safe Propellant Liquid Oxygen and Liquefied Natural Gas (Methane). *48th IAF Congress* **48**, (1997).

[51] F.M. Kirby. LOX/CH_4 for Reusable High Performance Booster Engines. *JANNAF Propulsion Meeting*, 253–260 (1984).

[52] D. Haeseler, C. Maeding, V. Roubinski, S. Khrissanfov. LOX-Hydrocarbon Rocket Engines and Thrust Chamber Technologies for Future Launch Vehicle Applications. *53rd International Astronautical Congress* **53**, (2002).

[53] L. Pons, N. Darabiha, S. Candel, G. Ribert, V. Yang. Mass Transfer and Combustion in Transcritical Non-premixed Counterflows. *Combust. Theor. Model.* **13**, 57–81 (2009).

[54] S. Candel, M. Juniper, G. Singla, P. Scouflaire, C. Rolon. Structure and Dynamics of Cryogenic Flames at Supercritical Pressure. *Combust. Sci. Tech.* **178**, 161–192 (2006).

[55] G. Singla, P. Scouflaire, C. Rolon, S. Candel. Transcritical Oxygen/Transcritical or Supercritical Methane Combustion. *Proc. Combust. Inst.* **30**, 2921–2928 (2005).

[56] G. Singla, P. Scouflaire, C. Rolon, S. Candel. Flame Stabilization in High Pressure LOX/GH_2 and GCH_4 Combustion. *Proc. Combust. Inst.* **31**, 2215–2222 (2007).

[57] B. Yang, F. Cuoco, M. Oschwald. Atomitation and Flames in LOx/H_2 and LOx/CH_4 - Spray Combustion. *J. Propulsion Power* **23(4)**, 763–771 (2007).

[58] J. Lux, O. Haidn. Flame Stabilization in High-pressure Liquid Oxygen/Methane Rocket Engine Combustion. *J. Propulsion Power* **25**, 15–23 (2009).

[59] J. Lux, O. Haidn. Effect of Recess in High-pressure Liquid Oxygen/Methane Coaxial Injection and Combustion. *J. Propulsion Power* **25**, 24–32 (2009).

[60] H.K. Chelliah, K. Seshadri, C.K. Law. *Reduced Kinetic Mechanisms for Counterflow Methane Diffusion Flames. In: Reduced Kinetic Mechanisms for Applications in Combustion Systems.* Springer Verlag, 15 Edition, (1993).

[61] M. Bollig, A Linan, A.L. Sanchez, F.A. Williams. A Simplified Approach to the Numerical Description of CH_4/Air Diffusion Flames. *Proc. Combust. Inst.* **27**, 595–603 (1998).

[62] L. Pons, N. Darabiha, S. Candel. Pressure Effects on Nonpremixed Strained Flames. *Combust. Flame* **152**, 218–229 (2008).

[63] J. Du, L. Axelbaum. The Effects of Flame Structure on Extinction of CH4/Air Diffusion Flame. *Proc. Combust. Inst.* **26**, 1137–1142 (1996).

[64] C.H. Sohn, I.M. Jeong, S.H. Chung. Numerical Study of the Effects of Pressure and Air-Dilution on NO Formation in Laminar Counterflow Diffusion Flames of Methane in High Temperature Air. *Combust. Flame* **130**, 83–92 (2002).

[65] C. Gibaud, J.A. Snyder, V. Sick, R.P. Lindstedt. Laser Induced Fluorescence Measurements and Modeling of Absolute CH Concentrations in Strained Laminar CH_4/Air Diffusion Flames. *Proc. Combust. Inst.* **30**, 455–463 (2006).

[66] K.T. Walsh, M.B. Long, M.A. Tanoff, M.D. Smooke. *Experimental and Computational Study of CH, CH^* and OH^* in an Axisymetric Laminar Diffusion Flame. Proc. Combust. Inst.* **27**, 615–623 (1998).

[67] Z. Cheng, J.A. Wehrmeyer, R.W. Pitz. Experimental and Numerical Studies of Opposed Jet Oxygen-Enhanced Methane Diffusion Flames. *Combust. Sci. Tech.* **178**, 2145–2163 (2006).

[68] Z. Cheng, J.A. Wehrmeyer, R.W. Pitz. Oxygen-Enhanced High Temperature Laminare Flames. *AIAA* **42**, Reno, Nevada (2004).

[69] S.V. Naik, N.M. Laurendeau, J.A. Cooke, M.D. Smooke. A Soot Map for Methane-Oxygen Counterflow Diffusion Flames. *Combust. Sci. Tech.* **175**, 1165–1167 (2003).

[70] A. Beltrame, P. Porshnev, W. Merchan-Merchan, A. Saveliev, A. Fridman, L.A. Kennedy, O. Petrova, S. Zhdanok, F. Amouri, O. Charon. Soot and NO Formation in Methane-Oxygen Enriched Diffusion Flames. *Combust. Flame* **124**, 295–310 (2001).

[71] K.K. Kuo. *Principles of Combustion.* John Wiley & Sons, Inc., (2005).

[72] F.A. Wiliams. *Combustion of Liquid Fuel Sprays.* Butterworth Co (Publishers) Ltd., (1990).

[73] J.O. Hirschfelder, C.F. Curtiss. Theory of Propagation of Flames, Part I: General Equations. *Proc. Combust. Inst* **3**, 121–127 (1949).

[74] R.B. Bird, W.E. Stewart, E.N. Lightfoot. *Transport Phenomena.* John Wiley & Sons, New York, (1960).

[75] J. O. Hirschfelder, C. F. Curtiss, R. B. Bird. *Molecular Theory of Gases and Liquids.* John Wiley & Sons Inc., New York, (1964).

[76] G. Abramzon, W.A. Sirignano. Approximate Theory of a Single Droplet Vaporization in a Convective Field: Effects of Variables Properties, Stefan Flow, and Transient Liquid Heating. Proceedings of the 2nd ASME-JSME Thermal Engineering Joint Conference, Honululu, Hawai **1**, 11–18 (1987).

[77] G. Abramzon, W.A. Sirignano. Droplet Vaporization Model for Spray Combustion Calculations. *AIAA 26th Aerospace Science Meeting, Reno, Nevada*, AIAA–88–0636 (1988).

[78] H Schlichting, Gestern.K. *Granzschicht Theory.* Springer, Berlin, Heidelberg, 9th Edition, (1997).

[79] R. Clift, J.R. Grace, M.E. Weber. *Bubbles, Drops and Particles.* Academic Press, New York, (1978).

[80] D. Schlotz, E. Gutheil. Modeling of Laminar Mono- and Bidisperse Liquid Oxygen/Hydrogen Spray Flames in the Counterflow Configuration. *Combust. Sci. Tech.* **158**, 195–210 (2000).

[81] K.C. Hsieh, J.S. Shuen, V. Yang. Droplet Vaporization in High-pressure Environments I: Near Critical Conditions. *Combust. Sci. Tech.* **76**, 111–132 (1991).

[82] G. Abramzon, W.A. Sirignano. Droplet Vaporization Model for Spray Combustion Calculations. *Int. J. Heat Mass Transf.* **9**, 1605–1618 (1989).

[83] G.L. Hubbard, V.E. Deny, A.F Mills. Droplet Evaporation: Effects of Transients and Variable Properties. *Int. J. Heat Mass Transfer* **18**, 1003–1008 (1975).

[84] R. Schmehl, G. Klose, R. Koch, S. Wittig. *Droplet Evaporation and Transport.* Brite euram report, Low Emission Combustor Technology Program - Phase III, Aeronautics Contract BRPR-CT95-0122, (1998).

[85] B. Sreznevsky. *Zh. R. F. Kho.* **14**, 420–483 (1982).

[86] G.M. Faeth. Evaporation and Combustion of Sprays. *Prog. Energy Combust. Sci.* **9**, 1–76 (1983).

[87] W.A. Sirignano. Fuel Droplet Vaporization and Spray Combustion. *Proc. Energy Combust. Sci.* **9**, 291–322 (1983).

[88] W.A. Sirignano. Fluid Dynamics of Sprays. *J. Fluids Eng.* **115**, 345–378 (1992).

[89] C.K. Law. Recent Advances in Droplet Vaporization and Combustion. *Prog. Energy Combust. Sci.* **8**, 171–201 (1982).

[90] J. Stengele, M. Willmann, S. Wittig. Experimental and Theoretical Study of Droplet Vaporization in a High Pressure Environment. *ASME* **97-GT-151**, (1997).

[91] A. Putnam. *ARS J.* **31**, 1467 (1961).

[92] D.A. McQuarrie, J.D. Simon. *Physical Chemistry: A Molecular Approach.* University Science Books, Sausalito, California.

[93] F.A. Lindemann. *Discussion on The Radiation Theory of Chemical Action.* Trans. Faraday Soc. **17**, 598.

[94] P.W. Atkins. *Physical Chemistry.* Oxford University Press, New York, 7th Edition, (2002).

[95] P.J. Robinson, K.A. Holbrook. *Unimolecular Reactions.* Wiley-Interscience, New York, (1972).

[96] D.M. Golden. *Gas Phase Homogeneous Kinetics. In: Low-Temperature Chemistry of the Atmosphere.* Moortgat GK ed., Springer-Verlag, Berlin/Heidelberg, (1994).

[97] D.L. Baulch, C.J. Cobos, R.A. Cox, C. Esser, P. Frank, Th. Just, J.A. Kerr, M.J. Pilling, J. Troe, R.W. Walker, J. Warnatz. *Evaluated Kinetic Data for Combustion Modelling.* J. Phys. Chem. Ref. Data **21**(3), 411 (1992).

[98] J. Troe, G. Ushakov. Rotational Effects in Broadening Factors of Fall-off Curves of Unimolecular Dissociation Reactions. *Faraday Discuss.* **119**, 145–157 (2001).

[99] J. Troe. *Predictive Possibilities of Unimolecular Rate Theory.* J. Phys. Chem. **83**, 114 (1979).

[100] J. Troe. *Theory of Thermal Unimolecular Reactions in the Fall-off Range. I.Strong Collision Rate Constants.* Ber. Bunsenges. Phys. Chem. **87**, 161 (1983).

[101] R.G. Gilbert, K. Luther, J. Troe. *Theory of Thermal Unimolecular Reactions in the Fall-off Range. II. Weak Collision Rate Constants.* Ber. Bunsenges. Phys. Chem. **87**, 169 (1983).

[102] R.J. Kee, J. Warnatz, J.A. Miller. *A FORTRAN Computer Code Package for the Evaluation of Gas-Phase Viscosities, Conductivities, and Diffusion Coefficients.* Sandia Report SAND83-8209, Sandia National Laboratories Report Technical Report, (1988).

[103] Japan Society of Mechanical Engineers (JSME). *Data Book: Thermophysical Properties of Fluids.* (1983).

[104] Schlotz D. *Modellierung laminarer und turbulenter Flüssig-Sauerstoff/ Wasserstoff-Sprayflammen unter kryogenen Hochdruckbedingungen.* Phd thesis, Universität Stuttgart, (2001).

[105] C. Hollmann, E. Gutheil. *Modeling of Turbulent Spray Diffusion Flames Including Detailed Chemistry.* Proc. Combust. Inst. 26 **1**, 1731–1738 (1996).

[106] C. Hollmann, E. Gutheil. *Flamelet-Modeling of Turbulent Spray Diffusion Flames Based on a Laminar Spray Flame Library.* Combust. Sci. and Tech. **1**, 135–175 (1998).

[107] P.M. Struk, M. Ackerman, V. Nyagam, D.L. Dietrich. On Calculating Burning Rates during Fiber Supported Droplet Combustion. *Microgravity Sci. Tech.* **11**, 144–151 (1998).

[108] H. C. Van de Hulst. *Light Scattering by Small Particles*. Wiley, (1999).

[109] C. Bohren, D. Huffman. *Absorption and Scattering of Light by Small Particles*. Wiley, (1983).

[110] P.W. Atkins. *Physicalische Chemie*. VCH-Verlag, Oxford, UK, 1st Edition, (1990).

[111] R. C. Reid, J. M. Prausnitz, B. E. Poling. *The Properties of Gases and Liquids*. McGraw-Hill, (1987).

[112] M. Lisal, W. Smith, I. Nezbeda. Accurate Vapour-Liquid Equilibrium Calculations for Complex Systems Using the Reaction Gibbs Ensemble Monte Carlo Simulation Method. *Fluid Phase Equilibria* **181**, 127–146 (2001).

[113] G. Continillo, W.A. Sirignano. Counterflow Spray Combustion Modeling. *Combust. Flame* **81**, 325–340 (1989).

[114] E. Gutheil, W.A. Sirignano. Counterflow Spray Combustion Modeling Including Detailed Transport and Detailed Chemistry. *Combust. Flame* **113**, 92–105 (1998).

[115] G. Continillo, W.A. Sirignano. Counterflow Spray Combustion Modeling. *AIAA 27th Aerospace Science Meeting, Reno, Nevada*, AIAA–89–0051 (1989).

[116] S. V. Patankar. *Numerical Heat Transfer and Fluid Flow*. Hemisphere Publishing Corporation, USA, (1980).

[117] U. Maas. *Mathematische Modellirung instationärer verbrennungsprozesse unter Verwendung detaillierter Reaktionesmechanismen*. Dissertation, Universität Heidelberg, (1988).

[118] F. John. *Partial Differential Equations*. Springer-Verlag, Heidelberg, 4th Edition, (1982).

[119] W.H. Press, B.P. Flannery, S.A. Teukolsky, W.T. Vetterling. *Numerical Recipes, The Art of Scientific Computing*. Cambridge University Press, Cambridge, 1st Edition, (1989).

[120] E. Gutheil. Structure and Extinction of Laminar Ethanol/Air Spray Flames. *Combust. Theor. Model.* **5(2)**, 131–145 (2001).

[121] E. Gutheil. Multiple Solutions for Structures of Laminar Counterflow Spray Flames. *Progress in Computational Fluid Dynamics* **5(7)**, 414–419 (2005).

[122] N. Peters. *Laminar Flamelet Model of Turbulent Combustion in: Numerical Simulation of Combustion Phenomena*. Springer, k. bray, ed Edition, (2006).

Acknowledgements

I feel myself fortunate enough to have the support of my supervisors, colleagues, family and friends, who helped me in completing this thesis. Their suggestions and feedback was really useful and valuable. I am indebted to pay my gratitude to Prof. Eva Gutheil, who helped and guided me throughout this work. She corrected my papers, presentations and this thesis with great patience. She also helped me in availing the financial support from DFG. Without her invaluable support and guidance, the writing of this thesis might have not been possible.

I am grateful to Prof. Uwe Riedel for his precious suggestions and corrections in the present thesis, which helped me in achieving this milestone. I extend my thanks to Late Prof. Jürgen Warnatz, who provided me with chemical mechanisms that contributed towards completing this work successfully. He has always been kind and helpful.

I acknowledge the support of all of my colleagues during my stay in this group. I thank to Hai-Wen Ge, Marco de Rosa, Yarlanki Sriniwas, Peter Groppenbächer, Rana Muhammad Humza, Srikanth Reddy G, Xinguang Cui and Cao Le for their valuable support and encouragement. I especially thank Rana Muhammad Humza and Srikanth Reddy G for reading and correcting the thesis. I also acknowledge the help of Peter Groppenbächer for correcting the German language in Kurzfassung.

My parents have helped me at each step of my life, especially in academic career. I do not have words to account for their favors, help and guidance. They have always been source of my motivation and strength, particularly in this work. I supplicate my heartiest gratitude to them.

Erklärung

Ich erkläre hiermit, dass ich diese Arbeit selbständig verfasst und keine anderen als die angegebenen Quellen und Hilfsmittel benutzt habe.

Heidelberg, 11. Mai 2010